

https://dspace.org/

Detecting reversals in Earth’s magnetic field using continuous core samples: a new measurement system

Warrener, Nicholas Myles

2025-09
University of the Witwatersrand, Johannesburg
https://hdl.handle.net/10539/49902
Warrener, Nicholas Myles. (2025). Detecting reversals in Earth’s magnetic field using continuous core samples: a new measurement system. [Master's dissertation, University of the Witwatersrand, Johannesburg]. WIReDSpace. https://hdl.handle.net/10539/49902

Downloaded from a DSpace repository. https://dspace.org/



University of the Witwatersrand, Johannesburg

Master of Science in Engineering

Detecting reversals in Earth's magnetic field using continuous core samples: a new measurement system

Nicholas Myles Warrener

School of Electrical Engineering and Information Engineering

A dissertation submitted to the Faculty of Engineering and the Built Environment, University of the Witwatersrand, Johannesburg in fulfilment of the requirements for the degree of Master of Science in Engineering.

30th September 2025

Abstract

To detect reversals in the geomagnetic field of the Earth, the direction of the permanent magnetic field recorded by rocks during formation must be measured. Previous studies have shown that the 2054 Ga Bushveld Igneous Complex (BIC), located in South Africa, recorded at least seven reversals in the geomagnetic field of the Earth during emplacement and cooling. The exact boundaries delineating a change in polarity are poorly constrained. The Bushveld Drilling Project (BVDP) is retrieving 2.5 km of continuous drill core samples for various investigations, and this provides the opportunity to constrain the reversal boundaries. Existing commercial measurement systems cannot cope with the complete analysis of all the drill cores: small subsamples must be selected for detailed study. Without an instrument to characterise the magnetic field recorded by all the drill cores, subsampling is ineffective as samples are chosen randomly. The work presents an investigation on the design and evaluation of a prototype measurement system to detect geomagnetic reversals recorded in continuous drill cores rapidly. Tests with synthetic drill cores and short sections of weakly magnetised drill cores from the Main Zone of the BIC show that the proposed system can resolve changes in the direction of the magnetic fields - on the order of a few nT. The minimum thickness of a layer of rock containing a reversed polarity that the measurement system can resolve is measured to be 30 mm. Provided that drilling overprints do not significantly alter the direction of the remanent magnetisation, the findings show that, in principle, the measurement system can detect changes in the direction of the magnetic field in drill cores from the BIC.

Declaration

I declare that this dissertation is my own unaided work. It is being submitted for the degree of Master of Science in Engineering to the University of the Witwatersrand, Johannesburg. It has not been submitted before for any degree or examination to any other university.



.....

Nicholas Myles Warrener

...30th... day of ...September 2025...

Acknowledgments

I extend my heartfelt gratitude to my supervisors, Professor Susan Webb and Professor Ken Nixon, for their exceptional guidance, dedication, and enthusiasm over the past two years. Their support made this journey rewarding and unforgettable. I am also deeply thankful to Professor Trond Torsvik for generously providing the magnetic shield for our research and to Professor William Morris for his invaluable expertise in downhole magnetics. Special thanks go to Mr. Ray Van Rensburg from Geotron for loaning two fluxgate magnetometers and an acquisition system.

I am grateful to the School of Geosciences for their warm welcome and sense of community, and to the School of Electrical and Information Engineering for providing essential equipment, including the much-appreciated coffee machine. My appreciation extends to the academic staff for their insightful ideas and the administrative team for their support. I sincerely thank Mr. Gorden Konieczek from Sensorik & Systemtechnologie GmbH, the Elmer FEM development team, particularly Dr. Peter Råback and Mika Malinen, and community members "kevinarden" and "Rich_B" for their invaluable assistance.

This work was supported by the Focus on Africa Space Science and Technology for Future Development (FAST4Future) project, funded by the European Commission under grant agreement number 101082487 - ERASMUS-EDU-2022-CBHE. I am grateful for the productive discussions with Mykola Ivchenko (KTH Royal Institute of Technology) and Dario Modenini (University of Bologna), which enriched this research, through my participation in FAST4Future. Additionally, I thank the University for the financial support provided through the Postgraduate Merit Award.

Finally, I am profoundly grateful to my parents, family, and friends for their unwavering encouragement and support, without which this work would not have been possible.

Contents

1 Introduction **1**

1.1 Problem Statement and Motivation 3

1.2 Aim and Scope of Investigation 3

1.3 Overview 4

2 Background and Motivation **6**

2.1 Rock Magnetism 6

2.2 Magnetic Measurements 7

2.3 Magnetic Shields 10

2.4 Rock Magnetism Measurement Systems 11

2.4.1 Sensors 12

2.4.2 Systems for Small Samples 15

2.4.3 Systems for Long Drill Cores 17

2.5 Motivation 21

3 Investigative Framework **23**

3.1 Investigative Question 23

3.2 Research Strategy 24

3.2.1 Requirement Analysis and Component Selection 25
3.2.2 Magnetic Shield Simulation and Validation 25
3.2.3 Measurement of Real and Synthetic Drill Cores 25

4 Measurement System Design 26

4.1 Requirements 28
4.1.1 Detect Changes in the Direction of Magnetic Fields 28
4.1.2 Tolerance Toward Stray Magnetic Fields 32
4.1.3 Robust and Portable 34
4.1.4 Rapid Operation 34
4.2 Proposed Design 34

5 Magnetic Shield Finite Element Analysis 36

5.1 Modelling and Meshing 37
5.2 Finite Element Analysis 41

6 Experimental Methods 47

6.1 Measurement System Setup 47
6.2 Synthetic Drill Cores 51
6.3 Residual Field 53
6.4 Response to a Magnetic Dipole 56
6.5 Synthetic Reversals 60
6.6 Weakly Magnetised Drill Cores from the BIC 64
6.7 Strongly Magnetised Drill Core from the BIC 71

7 Tracing the Past: Evaluating a Magnetic Reversal Measurement System 75

7.1 Finite Element Analysis Validation 76

7.2 Measurement System Component Placement 82

7.3 Response to a Magnetic Dipole 84

7.4 Detecting Geomagnetic Field Reversals 88

7.5 Bushveld Igneous Complex Drill Cores 95

7.6 Oriented Drill Core 98

7.7 Alternative Applications 101

7.8 Limitations 102

7.9 Recommendations 104

8 Conclusion 109

References 111

Further Reading 118

A Magnetic Shield Specifications 119

A.1 Mechanical Specifications 119

A.2 ASTM A753 Alloy 4 Properties 122

B Magnetic Shield Finite Element Analysis Setup 124

B.1 Processing B-H Data for FEA Use 124

B.2 Geometry and Mesh 126

B.3 Simulation Input File 128

C Compute Resources **134**

C.1 System Specifications 134

C.2 Resource Usage 135

D Fundamentals and Terminology **137**

D.1 Magnetic Fields 137

D.1.1 Flux Density, Field Intensity, and Magnetisation 137

D.2 Physical Properties 138

D.2.1 Magnetic Permeability and Susceptibility 138

D.3 Terminology 139

List of Figures

1.1 A simplified geologic map of the Bushveld Igneous Complex (BIC) in South Africa. The red cross on the Eastern Lobe indicates the location of the Bushveld Drilling Project (BVDP) borehole. Map of the BIC modified and used with permission, from Webb et al. (2004). The blank map of South Africa, by Wikimedia user "Clapsus", is used under license (CC BY-SA 3.0) 2

2.1 A diagram depicting a magnetic dipole moment **m** positioned along the z-axis and an arbitrary measurement point Q. The diagram is adapted from Griffiths (2023) and represents the geocentric axial dipole of the average magnetic field of the Earth [14]. 9

2.2 Instruments used for the measure of magnetism in rock samples. An *italicised* name indicated a prototype instrument that was not commercially available. Diagram compiled from the works of Heye and Meyer (1972) and Noel, Pickering and Molyneux (1989), Butler (1992), Weeks et al. (1993), Goree (2007), Foss, Leslie and Stuart (2015), and Ripka (2021). 12

2.3 A simplified diagram of a single-component Vacquier-type fluxgate magnetometer. The high-permeability cores and excitation winding have been separated from the sense winding for visibility. In a real device, the sense winding is wrapped around both the high-permeability cores and the excitation winding. Source: Adapted from Figure 3.4b in Ripka (2021). 13

2.4 A diagram of a measurement system designed for the measurement of the radial component of magnetisation present in a drill core. The directions of the radial and axial components of magnetisation are illustrated by the bold horizontal arrow and vertical dashed arrow, respectively. Source: Adapted from Figure 1 in Heye and Meyer (1972). 18

2.5 A diagram of a measurement system designed for the measurement of axial remanent magnetisation of long sediment cores. The directions of the radial and axial components of magnetisation are illustrated by the vertical dashed arrow and bold horizontal arrow, respectively. Source: Adapted from Figure 1b in Noel, Pickering and Molyneux (1989). 19

2.6 A measurement system for the determination of remanent and induced magnetisation along drill cores proposed by Foss, Leslie and Stuart (2015). 20

4.1 Professors Susan Webb and Lewis Ashwal, surrounded by 900 m of Bellevue drill core, performed magnetic susceptibility measurements in the National Core Library hosted at the Council for Geoscience, Donkerhoek, Pretoria. Reproduced with permission from Ashwal, Webb and Knoper (2005). 27

4.2 A diagram illustrating the intended application for an instrument used to rapidly identify sections of drill core that would be set aside for palaeomagnetic study. 28

4.3 A diagram of the proposed measurement system with a second fluxgate magnetometer introduced to facilitate operation as a magnetic gradiometer. 34

5.1 Different views of the magnetic shield proposed for use in the investigation. 38

5.2 A simplified, not to scale, diagram depicting a cross-section of the geometry used to represent a two-layer cylindrical magnetic shield. The annotations indicate areas in the model where the mesh size was controlled with transfinite curves. 39

5.3 Different views of the mesh representing the two-layer magnetic shield used in the FEA. For visibility, only the 2D mesh elements are shown. The innermost cylinder in (b) is the region referred to as the "internal transition region". 40

5.4 Main and minor axis slices of the magnitude of the magnetic flux density, coloured in 50 bins, inside a two layer cylindrical magnetic shield exposed to an ambient geomagnetic field (I:−64.0°, D:−12.4°, F:22 792.9 nT). The mesh used by the FEA contained 95 M elements. 44

5.5 A line plot of the magnitude of the magnetic flux density along the main axis of a magnetic shield while varying the element count of the input mesh used in the FEA. The 0 m position corresponded to the midpoint of the main axis of the shield. The shield spanned from −0.447 m to 0.447 m in the plot. 45

5.6 A plot of a small section of Figure 5.5, centred around the midpoint of the main axis of the magnetic shield. 46

6.1 The components of the measurement system used in the investigation and a simplified diagram of the measurement system. 49

6.2 The setup used to degauss the magnetic shield. The magnetic shield is on the left side of the image, while the multimeter is in the centre and the variable autotransformer is on the right. 51

6.3 A diagram illustrating the process used to create synthetic drill cores from a cassette tape. 52

6.4 Magnetic flux density as a function of position along the main axis of a two-layer magnetic shield. The 0 m position corresponds to the midpoint of the main axis of the shield. The area marked "Shielded region" corresponds to measurements taken inside the magnetic shield. 54

6.5 A small section of Figure 6.4, centred around the midpoint of the main axis of the magnetic shield used in the investigation. The grey rectangle in the inset graph indicates where the enlarged section was taken from Figure 6.4. 55

6.6 X component of the response of a fluxgate magnetometer to a magnetic dipole. The line of best fit, for positions between 540–1200 mm, was an eight-term Fourier model ($R^2 = 0.9984$, RMSE = 0.0886). The effective sampling rate was 8 Hz. The 'shielded region' annotation indicates the extent of the area enclosed by the magnetic shield. 57

6.7 Y component of the response of a fluxgate magnetometer to a magnetic dipole. The line of best fit was an eight-term Fourier model ($R^2 = 0.7203$, RMSE = 0.0727). The effective sampling rate was 8 Hz. The 'shielded region' annotation indicates the extent of the area enclosed by the magnetic shield. 58

6.8 Z component of the response of a fluxgate magnetometer to a magnetic dipole. The line of best fit was a six-term Gaussian model ($R^2 = 0.9818$, RMSE = 0.1708). The effective sampling rate was 8 Hz. The 'shielded region' annotation indicates the extent of the area enclosed by the magnetic shield. 59

6.9 A diagram of three synthetic drill cores used to evaluate the ability of the proposed measurement system to resolve changes in the direction of a magnetic field. Samples A and C had magnetisations oriented in the same direction, while sample B had a magnetisation in the opposite direction. 60

6.10 Three sets of fluxgate magnetometer outputs were collected using three synthetic drill cores passed under the sensor, with the length of the centre standard varied each run. The effective sampling rate was 10 Hz. The legend in Figure 6.10c applies to Figures 6.10a and 6.10b. 62

6.11 Three sets of fluxgate magnetometer outputs were collected using two synthetic drill cores, separated by a gap, passed under the sensor, with the length of the gap varied each run. The effective sampling rate was 10 Hz. The legend in Figure 6.11a applies to Figures 6.11b and 6.11c. 63

6.12 Images of the Main Zone drill cores, from the BIC, with weak remanent magnetisation. Drill cores with identifiers 4/3, 4/4, and 4/5 are presented in the top, centre, and bottom of the image, respectively. All cores had a diameter of 40 mm and cores 4/3, 4/4, and 4/5 had lengths of 290 mm, 380 mm, and 390 mm, respectively. 65

6.13 Magnetic susceptibility measurements, as a function of position along drill core 4/3, 4/4, and 4/5, recorded with the GDD MPP instrument. 67

6.14 A plot of the three components of the magnetic flux density recorded for drill core with ID 4/3, from the Main Zone of the BIC, that contained little magnetic minerals, passed through the measurement system used in the investigation. The effective sampling rate was 20 Hz. 68

6.15 A plot of the three components of the magnetic flux density for the drill core with ID 4/3, from the Main Zone of the BIC, that contained little magnetic minerals, passed through the measurement system used in the investigation. The effective sampling rate was 10 Hz. 69

6.16 A plot of the three components of the magnetic flux density for the drill core with ID 4/4, from the Main Zone of the BIC, that contained little magnetic minerals, passed through the measurement system used in the investigation. The effective sampling rate was 10 Hz. 70

6.17 A plot of the three components of the magnetic flux density for the drill core with ID 4/5, from the Main Zone of the BIC, that contained little magnetic minerals, passed through the measurement system used in the investigation. The effective sampling rate was 10 Hz. 71

6.18 An image of the strongly magnetised drill core from the Critical Zone in the Eastern Lobe of the BIC. The "A" side of the core is facing the camera. Ledwaba reported the sample had a length of 100 mm and a diameter of 30 mm [56]. 72

6.19 Magnetic susceptibility measurements as a function of position along the drill core recovered near the Atok mine, recorded by the GDD MPP instrument. The letters in the legend correspond to four different profiles taken along the length of the drill core. Each profile was a 90° rotation about the main axis from the other. 73

6.20 A plot of the three components of the magnetic flux density for a drill core, from the Critical Zone in the Eastern Lobe of the BIC. The effective sampling rate was 600 Hz. 74

7.1 A line plot comparing the FEA and experimental results for the magnetic flux density along the main axis of the magnetic shield used in the investigation. The centre of the shield, along the main axis, is found at the 0 m position and the space enclosed by the shield is indicated on the plot as the "shielded region". 78

7.2 A small section of Figure 7.1 focuses on the midpoint of the main axis of the magnetic shield, comparing the FEA and experimental results for the magnetic flux density. 79

7.3 Main and minor axis slices of the Frobenius norm of the gradient tensor of the magnetic flux density ($||\nabla \boldsymbol{B}||_F$), coloured in 85 bins, inside a two-layer cylindrical magnetic shield exposed to an ambient geomagnetic field. 81

7.4 A not-to-scale diagram of a synthetic drill core passed under a fluxgate magnetometer, with component orientations depicted. Idealised field lines around the drill core are displayed. 85

7.5 The three components of the response of a fluxgate magnetometer to a magnetic dipole as the dipole was moved closer to the fluxgate, directly under the fluxgate, at 0 m, and then away from the fluxgate. The lines of best fit, depicted here, are derived from the measurement points in Figures 6.6, 6.7, and 6.8. The positions of each set of results were adjusted so that at 0 m, all responses corresponded to the dipole being directly under the corresponding sense element inside the magnetometer. The space enclosed by the shield is indicated on the plot as the "shielded region". 87

7.6 A diagram illustrating how the geomagnetic field of the Earth is expressed in spherical coordinates. The diagram is adapted from Lowrie (2007). 88

7.7 Plots of the computed declination and inclination of the magnetic flux density where the width of the centre synthetic drill core was varied. The polarity of the magnetisation of the outer synthetic drill cores was the same, while the centre synthetic drill core had the opposite polarity. 91

7.8 Plots of the change in declination and inclination of the magnetic flux density, for three experiments, each with a different length space between two synthetic drill cores having magnetisations with the same polarities. 94

7.9 Plots of the change in declination and inclination of the magnetic flux density, for three drill cores taken from the Main Zone of the BIC. 96

7.10 A diagram depicting the two angles used to describe the trajectory, blue line, of a borehole in three-dimensional space and a third angle, θ_{roll}, that describes the direction that the drill core faces. The borehole is constrained to the grey plane, which is parallel to the vertical axis and not orthogonal to either horizontal axis. Borehole trajectory diagram adapted from Figure 3 in [59]. 99

7.11 A diagram that illustrated how the position of a drill core, white rectangle with two regions of measurement (A and B), would alter the distance, d_A and d_B between the regions of measurement and the fluxgate magnetometer (black dot). 100

7.12 A simplified diagram, excluding the magnetic shield for clarity, of an automated version of the proposed measurement system where the only user intervention required is the loading of drill core and initiation of the measurement procedure. 106

A.1.1 A dimensioned drawing of the side of the magnetic shield used in the investigation. 120

A.1.2 A dimensioned drawing of the front of the magnetic shield used in the investigation. 121

B.1.1 A semi-log plot of the original B-H points measured by Arpaia et al. for 1.4 mm thick ASTM A753 Alloy 4 and a line plot derived from fitting a cubic spline to the original data. 126

C.2.1 A bar graph of the number of elements in an input mesh, to an FEA, and the amount of CPU time taken for the FEA code to reach the convergence criterion. 135

C.2.2 A bar graph of the number of elements in an input mesh, to an FEA, and the maximum memory usage, per compute node, during execution of the FEA code. 136

List of Tables

4.1 A table of results presenting the approximate magnitude of the magnetic flux density measured by a magnetometer positioned at varying distances (r) and angles (θ) from an idealised magnetic dipole moment based on NRM measurements of rock samples taken from the Main Zone in the Eastern Lobe of the BIC, by Letts et al. NRM measurements compiled from Table 2 in Letts et al. (2009). . 29

4.2 A table of selected specifications for the two fluxgate sensors manufactured by Sensys GmbH, used in the investigation. Specifications adapted from [37] and noise measurements were compiled from certification reports of the individual sensors. 31

4.3 A table of selected specifications for the data acquisition system manufactured by Sensys GmbH, used in the investigation. Specifications adapted from [38]. 31

5.1 A table comparing the relative permeability of the different metals found in the magnetic shield used in the investigation. 38

5.2 A table listing the number of points on the transfinite curves, used in the generation of the input mesh for the FEA of the magnetic shield, for meshes with various element counts. Lines 50 to 59 in Listing B.2 correspond to the transfinite curves that were modified with the values given in this table. 41

6.1 A table of the minimum, maximum, and average values of the components of the ambient magnetic field, near the magnetic shield, when the residual field was measured. The X-component measured the vertical component, and the Y and Z components constituted the horizontal components of the geomagnetic field. The measurement duration was 1.48 h, and the effective sampling rate was 100 Hz. . . 56

7.1 A table comparing the length of three different regions inside a magnetic shield where the magnitude of the residual magnetic flux density, for all three components, was less than three different threshold values. The length of the region reported in the table is centred on the midpoint of the main axis of a two-layer cylindrical magnetic shield. 83

A.1 A table of B-H data for 1.4 mm thick ASTM A753 Alloy 4 derived from Sample 2 in Figure 3 from the paper by Arpaia et al., used to fit a cubic spline and interpolate points for magnetic shield simulations in the investigation. 123

List of Abbreviations

BIC Bushveld Igneous Complex. ix, xiii, xiv, xvi, xviii, 2, 3, 21, 25, 27, 29, 65, 68–72, 74–76, 95, 96, 98, 103, 109

BVDP Bushveld Drilling Project. ix, 2, 3, 27, 29

DAS Data Acquisition System. 31, 34, 48, 49, 106

DIRM Drilling-Induced Remanent Magnetisation. 7, 97, 103, 104, 109

FEA finite element analysis. xi, xv, xvii, xviii, 4, 5, 11, 24, 25, 36–38, 40–46, 53, 74–80, 82, 83, 107, 124, 128, 134–136

HPA high permeability alloy. 37–42, 50, 79, 80, 84

MD multi-domain. 7, 104, 105

NRM natural remanent magnetisation. 7, 8, 29, 64, 98

ODP Ocean Drilling Program. 17, 18, 103

PVC Polyvinyl Chloride. 34, 48

SD single domain. 7, 104, 105

SQUID Superconducting QUantum Interference Device. 12, 14–17, 30

SRM Superconducting Rock Magnetometer. 16–18, 21, 33

UDP User Datagram Protocol. 31, 49

List of Symbols

θ_{azimuth}, θ_{tilt}	Borehole trajectory angles	$^\circ$
κ_v	Bulk magnetic susceptibility	SI Units
D	Declination of a magnetic field	$^\circ$
$\boldsymbol{r}$	Displacement vector	m
$\boldsymbol{B}_{\mathbf{ambi}}$	Flux density of the ambient magnetic field	T
I	Inclination of a magnetic field	$^\circ$
$\boldsymbol{M}_{\mathbf{indu}}$	Induced magnetisation	A/m
$\boldsymbol{m}$	Magnetic dipole moment	$\mathrm{A\,m^2}$
$\boldsymbol{H}$	Magnetic field strength	A/m
$\boldsymbol{B}$	Magnetic flux density	T
$\boldsymbol{B}_{\mathbf{NRM}}$	Magnetic flux density associated with the NRM	T
μ_0	Magnetic permeability of free space	$\mathrm{N/A^2}$
$\boldsymbol{M}$	Magnetisation	A/m
$\boldsymbol{M}_{\mathbf{NRM}}$	Natural remanent magnetisation	A/m
θ_{roll}	Orientation of a drill core about the main axis	$^\circ$
$\hat{\boldsymbol{\theta}}$, $\hat{\boldsymbol{\phi}}$, $\hat{\boldsymbol{r}}$	Spherical coordinate system basis vectors	
V	Volume	$\mathrm{m^3}$

Chapter 1

Introduction

The geomagnetic field of the Earth shields the planet from charged particles emitted by the Sun and other cosmic sources. While the environmental implications of a weakened or absent geomagnetic field are passionately debated, an increase in the amount of charged particles reaching the surface of the planet would cause interference in electrical power infrastructure, satellites, and communication systems.

Palaeomagnetism and palaeointensity are branches of the geosciences concerned with determining the direction and intensity of the geomagnetic field recorded by certain minerals during or after formation, respectively [1]. Palaeomagnetic studies have shown that the geomagnetic field is not constant and varies randomly in intensity and direction over geologic timescales due to the chaotic system responsible for generating the magnetic field [1]. This physical process, known as the geodynamo, within the core of the Earth, cannot be observed directly due to the extreme depth at which it occurs. The evolution of this mechanism remains poorly understood for much of the history of the Earth [2].

Data on the direction of the geomagnetic field at specific points in time, particularly before, during, and after reversals in the direction of the field, enable comparisons of reversal processes across geological timescales. Such insights help refine and constrain numerical models of the geodynamo [2]. The only method to gather information about the geomagnetic field is through palaeomagnetic studies of rock

samples, sediments, and archaeological sources (pottery and hearths) [2, 3].

The largest layered mafic intrusion on Earth, known as the Bushveld Igneous Complex (BIC), Figure 1.1, is an economically significant region in South Africa as it hosts more than three-quarters of the known deposits of the platinum group metals in the world [4]. The 2054 Ga BIC is significant in terms of palaeomagnetic studies as Letts et al. (2009) have shown that the Eastern Lobe, amongst others, recorded seven reversals in the geomagnetic field during emplacement and subsequent cooling [5, 6]. Not all seven reversals may be unique as Cawthorn and Webb (2013) demonstrated that some of these reversals may have been repeated due to the way the BIC cooled during formation [6].

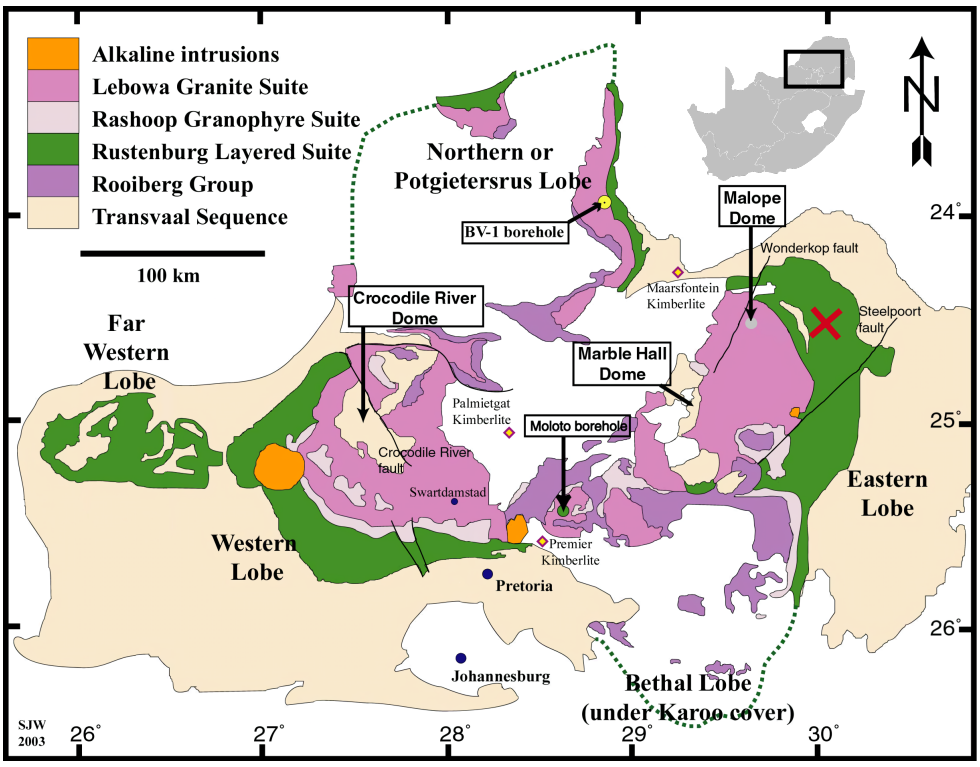


Figure 1.1: A simplified geologic map of the Bushveld Igneous Complex (BIC) in South Africa. The red cross on the Eastern Lobe indicates the location of the Bushveld Drilling Project (BVDP) borehole. Map of the BIC modified and used with permission, from Webb et al. (2004). The blank map of South Africa, by Wikimedia user "Clapsus", is used under license (CC BY-SA 3.0)

1.1 Problem Statement and Motivation

The Bushveld Drilling Project (BVDP) is drilling a 2.5 km deep borehole into the Eastern Lobe of the BIC and retrieving a continuous set of drill cores for detailed study [8]. The drill cores provide the opportunity to identify the region in the BIC stratigraphy where the geomagnetic field of the Earth *transitioned* from one polarity to another and to study the behaviour of the geomagnetic field *during* a reversal at two billion years.

Existing instruments used to determine the direction of the magnetisation in rock samples, precisely, make measurements on cylindrical (diameter of 25 mm and height 22–25 mm) or cuboidal (side length 20–25 mm) samples [1, 9]. A complete analysis of 2.5 km of drill core for the detection of changes in the direction of magnetisation would amount to the individual measurement of more than 110 000 cylindrical samples with existing instruments.

Palaeomagnetic studies are time-consuming processes. Identifying the precise location of a magmatic reversal in a stratigraphic magmatic palaeomagnetic study becomes impractical as soon as more than a few metres of drill core need to be analysed. Without a method for continuously measuring the permanent magnetic field along the drill cores, delineating the exact stratigraphic positions where the recorded magnetic field transitioned from one polarity to another remains a significant challenge for palaeomagnetic studies.

1.2 Aim and Scope of Investigation

To detect changes in the direction of the geomagnetic field recorded in continuous drill cores, it was necessary to evaluate the ability to measure weak permanent magnetic fields - significantly weaker than the ambient geomagnetic field. This capability is required to identify subtle variations in magnetisation that may indicate geomagnetic reversals.

Measurements were conducted on short sections of weakly magnetized drill cores from the BIC to assess whether this approach could reliably detect directional changes. These tests provided an initial evaluation of the sensitivity and effectiveness

of the method in recording weak palaeomagnetic signals.

To further explore the feasibility of this approach, the investigation focused on adapting the underlying physical principles of rock magnetism to long sections of drill core. A prototype measurement system was designed and tested using both real and synthetic drill core samples. While the results demonstrated the potential of this method, further refinements are necessary to enhance the robustness of the system for field applications.

1.3 Overview

The structure and summary of each chapter is as follows:

Chapter 2: A brief explanation of the fundamentals of rock magnetism and magnetic measurements is provided. A summary of the existing instruments and applications to palaeomagnetic studies is contextualised. This information is used to identify a new measurement system capable of rapidly detecting changes in the direction of the magnetic fields in drill cores.

Chapter 3: A concise description of the research question is presented, and the framework used to perform the investigation is outlined.

Chapter 4: The requirements for the proposed measurement system, aimed at addressing the investigative question, are provided. In analysing the requirements, the design of the proposed measurement system is presented.

Chapter 5: The method for developing a finite element analysis (FEA) of a two-layer cylindrical magnetic shield is described, and the results of the analysis are presented.

Chapter 6: The construction and standardisation of the experimental setup are discussed. Measurements are collected to evaluate the accuracy of the FEA and test various responses of the setup to synthetic and real drill cores.

Chapter 7: The results obtained in **Chapters 5** and **6** are reconciled and a discussion of the measurements made with the synthetic drill cores and real drill

cores follows. Recommendations for a robust version of the proposed measurement system are given.

Chapter 8: The findings of the dissertation are summarised.

Additional supporting material is provided in the appendices as follows:

Appendix A: The mechanical drawings and magnetic properties of the magnetic shield are given.

Appendix B: The preparation of the B-H data used in the FEA is provided. The complete input geometry and simulation configuration for a magnetostatic FEA of a magnetic shield exposed to an ambient magnetic field are presented.

Appendix C: The CPU time and maximum memory usage for various configurations of the magnetostatic FEA of the magnetic shield are presented.

Appendix D: The terminology used in the measure of magnetic fields and magnetic properties is summarised.

In the following chapter, a background on the acquisition of remanent magnetisation in rocks is provided, and a summary of existing measurement systems is given to facilitate the development of a motivation for the investigation.

Chapter 2

Background and Motivation

This chapter provides the necessary background to understand the context and operating principles of existing measurement systems used to assess the remanent magnetization in rock samples. Based on this review, a motivation for developing a new measurement system is presented.

2.1 Rock Magnetism

Many magnetic minerals, like magnetite, can retain magnetic fields once an external magnetic field is removed [10]. If the mineral is heated above the Curie point, the permanent magnetisation is lost [10]. Conversely, a new permanent magnetisation is acquired when the mineral cools below this temperature *if* it is exposed to an ambient magnetic field [11].

Rocks are composed of a mixture of different minerals, and when igneous rocks form from cooling magmas or lavas containing iron, magnetic minerals such as magnetite, maghemite and hematite may form and acquire the direction of the ambient magnetic field as they cool [10]. When these magnetic minerals exceed a critical size, they lose the ability to become uniformly magnetised, known as

single domain (SD), instead subdividing into magnetic domains, with domain walls separating these, multi-domain (MD), regions [10].

The magnetisation of MD grains can be altered by moving the domain walls, which changes the size of neighbouring domains [10]. Some walls require less energy to move than is needed to change the uniform magnetisation of single domain (SD) grains, making SD grains more stable carriers of remanent magnetisation [10]. Magnetised SD grains typically exhibit high coercivities and retain their magnetisations for billions of years [10]. There also exists a third type of grain, known as a pseudo-single domain grain that are smaller than MD grains but larger than SD grains [10]. They have also been shown to be suitable and stable, carriers of remanent magnetisation - but not as stable as SD grains [12].

After the formation of a rock, MD grains acquire new magnetisation more readily than SD grains [10]. Alterations to the original magnetisation of the rock sample are referred to as secondary remanent magnetisation. One example, important in the palaeomagnetic study of rock samples drilled from the ground, is the Drilling-Induced Remanent Magnetisation (DIRM) acquired by the MD grains in drill cores due to the drilling process [13]. When a drill is used to extract a sample, the drill stem acts to concentrate the field lines of the ambient field in such a way that the drill head has a high density of field lines [13]. The high density of field lines means that the drill head can induce a permanent magnetisation, usually, in the MD grains. Collectively, the primary magnetisation and any subsequent secondary magnetisations that resulted from natural sources (such as metamorphism) are referred to as the natural remanent magnetisation (NRM), $\mathbf{M}_{\mathrm{NRM}}$, of the sample [10]. Artificial sources of permanent magnetisation, like DIRM, are collectively called overprints.

2.2 Magnetic Measurements

The magnetic field $\mathbf{B}$ measured near an object is composed of the magnetisation $\mathbf{M}$, generated by bounded currents intrinsic to the object, and the field $\mathbf{H}$, originating from the movement of external charge near the object [10]. Mathematically, the observed magnetic field is expressed as

$$\mathbf{B} = \mu_0(\mathbf{H} + \mathbf{M}) \tag{2.1}$$

where μ_0 is the magnetic permeability of free space.

Ignoring overprints, if the NRM of a sample is to be measured, Eq 2.1 requires that the contribution of free currents, to the total magnetic field must, ideally, be zero ($\mathbf{H} = 0\,\mathrm{A/m}$). If no external charges are moving near the sample, or significantly less than the bounded currents causing the permanent magnetisation, Eq 2.1 reduces to a form where only the NRM contributes to the observed magnetic field, now called the remanent or residual magnetic field $\mathbf{B}_{\mathrm{NRM}}$:

$$\mathbf{B}_{\mathrm{NRM}} = \mu_0\mathbf{M}_{\mathrm{NRM}} \tag{2.2}$$

The intensity of the magnetic field that imparted a permanent magnetisation on a rock sample is not equal to the intensity of the permanent magnetisation. The fraction of the inducing field that is "locked in" as a remanent magnetisation is a complex relationship dependent on material properties [11]. Various time-consuming palaeointensity procedures have been developed to experimentally determine the intensity of the geomagnetic field from the remanent magnetic field, but will not be considered further [11].

It is customary to express the geomagnetic field of the Earth in terms of a geocentric axial magnetic dipole moment to facilitate comparison with measurements taken from rock samples [11]. For a homogeneously magnetised sample, the magnetisation is expressed as the net magnetic dipole moment $\mathbf{m}$ over a volume V:

$$\mathbf{M} = \frac{\mathbf{m}}{V} \tag{2.3}$$

Substituting 2.3 into 2.2, the magnetic dipole moment associated with the permanent magnetic field, B_{NRM}, that originated from the NRM in a sample is expressed as

$$\mathbf{m} = \frac{1}{\mu_0}\mathbf{B}_{\mathrm{NRM}}V \tag{2.4}$$

Standard introductory texts on electromagnetism, by Griffiths (2023), for example, show that the magnetic flux density $\boldsymbol{B}$ measured at an arbitrary point Q of a magnetic dipole moment $\boldsymbol{m}$, positioned parallel to the z-axis of the local coordinate system in Figure 2.1, is expressed in spherical coordinates as [14]

$$\boldsymbol{B}(\boldsymbol{r}) = \frac{\mu_0 m}{4\pi r^3}(2\cos(\theta)\,\hat{\boldsymbol{r}} + \sin(\theta)\,\hat{\boldsymbol{\theta}}) \tag{2.5}$$

where the angles θ and ϕ, and the displacement vector $\boldsymbol{r}$ are defined in Figure 2.1.

Because the dipole is positioned parallel to the z-axis, it is rotationally invariant about this axis, which implies that Eq. 2.5 is not dependent on the angle ϕ - shown in Figure 2.1.

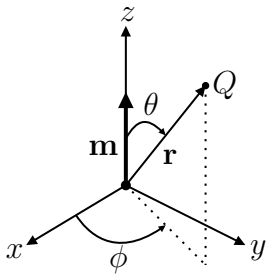


Figure 2.1: A diagram depicting a magnetic dipole moment $\mathbf{m}$ positioned along the z-axis and an arbitrary measurement point Q. The diagram is adapted from Griffiths (2023) and represents the geocentric axial dipole of the average magnetic field of the Earth [14].

In an environment free from any external magnetic fields, knowing the volume and the magnetisation of a rock sample - assumed to be uniformly remanently magnetised - the net magnetic dipole moment is $\boldsymbol{m} = \boldsymbol{M}V$ (Eq. 2.3). When measured at a sufficiently distant point, the magnetic flux density $\boldsymbol{B}$ at an arbitrary point near the sample can be estimated by treating the remanent magnetisation of the sample as a dipole

$$\boldsymbol{B}(\boldsymbol{r}) \approx \frac{\mu_0 \boldsymbol{M} V}{4\pi r^3}(2\cos(\theta)\,\hat{\boldsymbol{r}} + \sin(\theta)\,\hat{\boldsymbol{\theta}}) \tag{2.6}$$

The relationship in Eq 2.6 shows that magnetisation gives rise to a magnetic flux density in the region surrounding the magnetised object.

2.3 Magnetic Shields

Equation 2.1 shows that the ability to measure the remanent magnetisation of a rock sample hinges on the premise that the magnetisation induced in the sample by an ambient magnetic field is negligible. The means to attenuate or diminish the effect of unwanted external magnetic fields is facilitated by electromagnetic shielding.

The reduction of external magnetic fields that originate from artificial sources (such as the operation of electric motors, power lines, or the movement of vehicles) and natural sources (the geomagnetic field) is an important consideration in the development of systems designed to measure the magnetic flux density originating from remanent magnetisation in rock samples. Certain materials, like ferromagnetic alloys, are utilised to passively shunt or concentrate the field lines of the local magnetic field around a region of space in such a way that the region enclosed by the shielding material has a lower density of magnetic field lines than an unshielded region [15].

Passive magnetic shields function through two distinct mechanisms. The first mechanism shunts a static or quasi-static magnetic field around a region of space by providing a low reluctance path for the flux lines. The second mechanism works by the principle of eddy currents. When a time-varying magnetic field encounters a magnetic shield, electrical currents are induced in the material which, by Lenz's law, establish opposing magnetic fields that reduce the *net* intensity of the incident magnetic field [15]. This mechanism does not perfectly negate the incident field as the eddy currents set up in the shielding material experience impedances.

Magnetic shields are made from non-ideal materials, and the shields can become

magnetised by simply being exposed to an ambient magnetic field. The process of degaussing can be applied to the shield to reduce the acquired permanent magnetisation.

The performance of magnetic shields is analysed with analytical and computational methods. Analytical methods are most applicable to regularly shaped shields as these methods often rely on the assumption of infinite length [16]. With the rise of computational electromagnetic techniques, numerical methods have become popular for analysing shields with complex geometries and non-ideal material properties [17]. An example of such a method, the finite element analysis (FEA), is a widely used computational approach that facilitates the analysis of a broad range of physical phenomena by discretizing the domain of the problem space and computing relevant physical quantities across the entire domain.

The selection of the most appropriate computational method depends on the application. For example, the FEA is well suited to the analysis of complex geometries and materials that are anisotropic and have non-linear magnetic permeabilities [18]. A potential complication of the method of FEA requires that the entire problem domain be completely discretised. This increases computation time and prevents the method from being applied to problems with open boundaries [18]. For example, the evaluation of problem spaces that contain thin films (or regions) can become computationally unfeasible as the number of finite elements required to accurately represent the region becomes impractical and the demands on compute resources become astronomic [19].

2.4 Rock Magnetism Measurement Systems

With the fundamental physics of remanent magnetisation and magnetic shielding presented, it is possible to evaluate the existing sensors and measurement systems utilised in the measurement of rock magnetism. This is done through the presentation of selected magnetic field sensors and the measurement systems that employ them.

Magnetic fields are measured by a group of sensors collectively called magneto-

meters. There are a plethora of different types of these instruments, and each has properties that lend them to different applications. There are two general types of magnetometers: vector magnetometers measure the direction and intensity of a magnetic field, and scalar magnetometers only resolve the intensity.

In the context of palaeomagnetic studies, three types of magnetometer are most prominent in existing measurement systems - fluxgate, induction coil, and the Superconducting QUantum Interference Device (SQUID). Figure 2.2 presents instruments that make use of these different technologies.

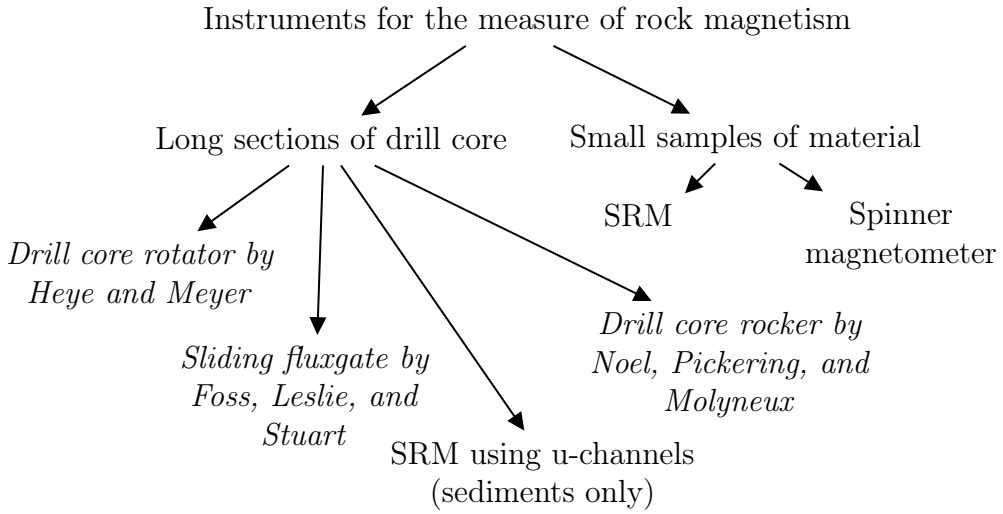


Figure 2.2: Instruments used for the measure of magnetism in rock samples. An *italicised* name indicated a prototype instrument that was not commercially available. Diagram compiled from the works of Heye and Meyer (1972) and Noel, Pickering and Molyneux (1989), Butler (1992), Weeks et al. (1993), Goree (2007), Foss, Leslie and Stuart (2015), and Ripka (2021).

2.4.1 Sensors

The induction coil sensor, used in spinner magnetometers, is one of the simplest types of magnetic field sensors, and the application of this technology was most prevalent in palaeomagnetic study before the maturation of fluxgate and SQUID technologies.

The induction coil magnetometer exploited Faraday's law of induction by noting

that the time rate of change of magnetic flux through an area enclosed by a conductive loop is equal to the induced electromotive force around the loop. By rotating a magnetised rock sample at the centre of an induction coil, a non-zero time rate of change of flux through the coil is established. Induction coil magnetometers only measure AC magnetic fields, and the noise and measurement range depend on the construction of the coil.

The application of this sensor in palaeomagnetic studies has largely been replaced by the fluxgate magnetometer, which will be discussed below.

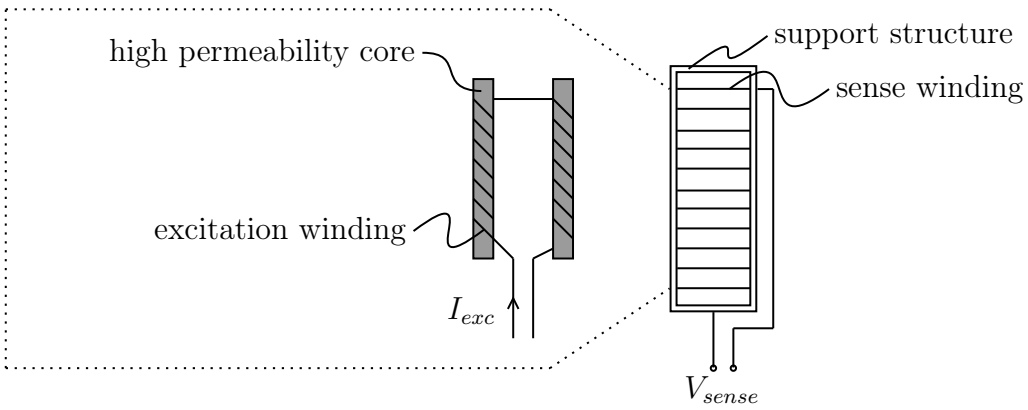


Figure 2.3: A simplified diagram of a single-component Vacquier-type fluxgate magnetometer. The high-permeability cores and excitation winding have been separated from the sense winding for visibility. In a real device, the sense winding is wrapped around both the high-permeability cores and the excitation winding. Source: Adapted from Figure 3.4b in Ripka (2021).

The fluxgate displayed in Figure 2.3 operates by passing an alternating current through the excitation winding, which periodically drives the high-permeability cores into and out of positive and negative saturation along the hysteresis profile of the material [25]. When no magnetic field is present, the net flux passing through the sense winding is zero - the high-permeability cores are driven by currents that establish magnetic fields in opposite directions [25]. In the presence of an ambient magnetic field, one of the two cores has an increased flux density since the ambient field and the field from the driving current interfere constructively [25]. Simultaneously, the net flux density in the other core will experience destructive interference as the ambient magnetic field and the field from the drive current are in

opposite directions [25]. The net effect is a non-zero net flux that induces a current in the sense coil. An arrangement of three fluxgate components in an orthogonal configuration facilitates the measurement of a three-dimensional magnetic field.

Fluxgate magnetometers measure both AC and DC magnetic fields, with a bandwidth of a few kilohertz, and typically have measurement ranges between 10 pT and 10 mT while having noise levels under $10\,\mathrm{pT_{RMS}}/\sqrt{\mathrm{Hz}}$ for export controlled versions [25, 26].

Modern fluxgate magnetometers suffer from two main issues.

First, the crossfield effect causes the sensors to register appreciable components of a magnetic field that are not parallel to the sensitive axis of each sensor [25]. The errors originating from crossfield effects are usually only of concern if measurements are being performed in the magnetic field of the Earth since these errors scale with the strength of the measured magnetic flux density [25].

Second, unlike a theoretical fluxgate sensor, which is a point sensor, real fluxgate sensors have sense elements with finite lengths (the high permeability core and excitation and sense windings in Figure 2.3). The magnetic flux density reported by a sensing element is a representation of the magnetic flux density averaged over the length of the element [20]. As a result, when the flux density changes rapidly, the measurement reported by the sensor may not correspond with the actual value at the position of the measurement [13].

Magnetometers that exploit quantum mechanical principles achieve noise levels significantly lower than fluxgate and induction coil magnetometers - a few $\mathrm{fT_{RMS}}/\sqrt{\mathrm{Hz}}$ [27]. One of these instruments is the DC SQUID.

When a ring of superconducting material transitions to the superconducting state while exposed to an ambient magnetic field parallel to the axis of the ring, a supercurrent is established inside the ring. A net magnetic flux is maintained inside the ring as an integer multiple of a flux quantum (2.067×10^{-15} Wb) [25, 28]. The supercurrent exists as long as the incident field persists. Changes in the intensity of the incident field change the supercurrent so that integer multiples of the flux quantum are maintained [28]. If the incident field increases to a threshold value,

the superconductor briefly becomes resistive, and the incident field penetrates the ring [28]. The supercurrent will now *decrease* and reverse direction to trap the flux inside the ring and restore the superconducting state [28]. The change in magnitude and direction of the supercurrent is a periodic function dependent on the incident field.

The SQUID depends on the response of the supercurrent to an incident magnetic field to function as a magnetic sensor. Practical considerations make using only a superconducting ring impractical for sensing, and many additional considerations, which are out of the scope of the explanation, are required [25].

SQUID magnetometers are known for their extreme sensitivity, which arises from the fundamental principle that magnetic flux in a superconductor is quantised in integer multiples of the minuscule flux quantum [25]. The ultra-low noise associated with SQUID sensors partly originates from the negligible thermal noise due to the operation of the sensor at cryogenic temperatures.

In practice, the minimum detectable field is often limited to background noise rather than the intrinsic ability of the sensor to resolve a field - only a few fT [29]. With the ability to resolve minuscule magnetic fields, steps must be taken to shield and compensate the sensors from unwanted ambient magnetic fields. A complete SQUID magnetometer is typically a large and heavy device due to the shielding and support equipment.

A peculiarity of SQUID-based magnetometers is that they are inherently differential devices. In practice, they record changes in the magnetic field relative to the flux state established when the sensor was first cooled into the superconducting state, a behaviour dictated by the design of the control circuitry [25]. In contrast, devices like the fluxgate and induction coil magnetometers measure the absolute magnetic field.

2.4.2 Systems for Small Samples

With the operation of the sensors relevant to palaeomagnetic studies summarised, the traditional measurement systems used to measure rock magnetism are presented.

Instruments used in palaeomagnetic studies of rock samples require the samples to have volumes less than 16 cm^3 and to be precisely cut into either a cylindrical or cuboidal shape [1]. The most prominent commercial instruments for the measurement of magnetisation in rock samples are the spinner magnetometer and Superconducting Rock Magnetometer (SRM).

The spinner magnetometer is the oldest type of modern magnetometer employed in palaeomagnetic studies. It functioned by rotating a small sample of rock at the centre of a set of detector (induction) coils inside an environment that was magnetically shielded [30]. Through the application of frequency domain analyses, the magnetisation associated with the fundamental frequency, the rate of rotation, was recovered, and information from additional harmonics gave insight into the homogeneity of the magnetisation [31]. The sensitivity of these instruments was proportional to the rotation rate of the sample, and higher sensitivities were only achieved with samples that did not disintegrate [25, 32]. With the replacement of induction coil sensors with fluxgate sensors in commercial spinner magnetometers, the sensitivity of the instrument is no longer dependent on the rotation rate [31].

In contemporary rock magnetism research, the SRM — which utilised the highly sensitive SQUID sensors — emerged as the preferred instrument of palaeomagnetic studies due to the unparalleled performance of the SQUID sensors [24].

An SRM consists of three SQUID sensors, a cryostat, magnetic shields, and a cryogen. SRMs are either positioned horizontally and have a continuous room temperature opening that facilitates the pass-through of discrete samples or are set up vertically and only have a room temperature opening on one side [24]. The insertion and removal of samples are computer-controlled by a motor. Historically, the vertical configurations were more common as there were technological limitations associated with the manufacture of the horizontal configurations [24].

Regardless of the configuration, a set of superconducting inductive pickup coils is used to facilitate the measurement of room-temperature samples by the SQUID sensors inside the cryostat [24]. The act of inserting, removing, or moving a sample near the pickup coils brings about an inductive current in the coils, which is transferred to the SQUID sensors for measurement [28].

One of the benefits of the pickup coils is that the response of the coils to a magnetised sample can be optimised for different applications.

2.4.3 Systems for Long Drill Cores

In contrast to systems designed for small rock samples, some instruments have been developed to measure rock magnetism in long drill cores. These systems fall into two main categories: those that require a near-zero-field environment for measurements and those that utilise the ambient magnetic field to assess both remanent and induced magnetisations. To date, only one commercially available system exists for the continuous measurement of drill cores.

Due to the unrivalled sensitivity of SQUID sensors inside SRMs, a great effort was made toward the development of a commercial product that supported the continuous passage of drill cores, up to 1500 mm in length [24]. The drawback of such a system is that it is only compatible with drill cores that can have a u-shaped channel pressed into them and a corresponding section of core removed [23]. The only drill cores that support this procedure are sediments. The benefit is that high-precision and automated measurements of the magnetisations along the u-shaped sections can be made every 10 mm [24]. Such a feat performed on a full-length drill core, cut into discrete samples, would be too time-consuming.

This method was used extensively aboard a research vessel used in the Ocean Drilling Program (ODP) where 20 km of sediments were analysed between 1985 and 1992 [24]. More recent publications, such as Philippe et al. (2018), have called the ability of this method to detect and accurately resolve magnetic field reversals into question. The convolution of the response of the SQUID sensors and inductive pickup coils with the unknown distribution of magnetisations in the u-shaped sections can produce a distorted representation of the magnetisations [33]. The traditional approach, the measurement of discrete samples, is better for the detection of geomagnetic reversals and excursions instead of continuous u-channel measurements [33].

In the literature, three classes of prototype instruments were developed to accommodate sedimentary and igneous drill cores, but none were commercialised.

The first instrument was designed to operate aboard a ship and predated the SRM system employed by the ODP campaign. In 1972, Heye and Meyer developed a system, Figure 2.4, for the detection of geomagnetic reversals recorded in sedimentary drill cores. The measurement system consisted of a suspended drill core, a magnetic shield, and two single-component fluxgate magnetometers. This setup was designed to immediately measure the component of remanence perpendicular to the main axis of deep-sea sedimentary drill core as they were recovered from a borehole during an ocean drilling project [20].

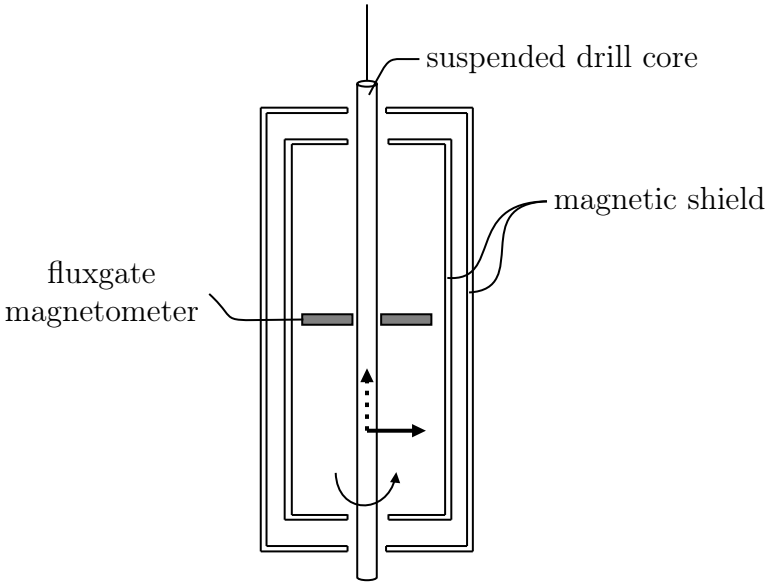


Figure 2.4: A diagram of a measurement system designed for the measurement of the radial component of magnetisation present in a drill core. The directions of the radial and axial components of magnetisation are illustrated by the bold horizontal arrow and vertical dashed arrow, respectively. Source: Adapted from Figure 1 in Heye and Meyer (1972).

The system operated by rotating a suspended drill core through a single revolution between two fluxgate magnetometers. Once completed, the drill core was incrementally moved through the system, and new measurements were taken. The process was repeated until the complete core was analysed. If a radial component of magnetisation existed, a sinusoidal signal, with a period equal to the rate of rotation, would be output by the magnetometer. If a reversal was recorded by the drill core, the peaks and troughs of the sinusoid would exhibit a 180° phase-shift

as the drill core was incrementally moved through the setup [20].

Synthetic drill core samples were fabricated and used in the determination of the minimum thickness of drill core that contained a magnetic reversal, resolvable by the system. Direction changes were detectable in synthetic drill core layers thicker than 30 mm [20].

A similar system, although not explicitly used for the detection of geomagnetic reversals, was developed by Noel, Pickering and Molyneux in 1989. The measurement system, shown in Figure 2.5, was intended for the measurement of the remanence component parallel to the main axis of the drill core [21]. The system was designed to address a key issue: selecting discrete units of continuous drill core for analysis could introduce orientation errors [21].

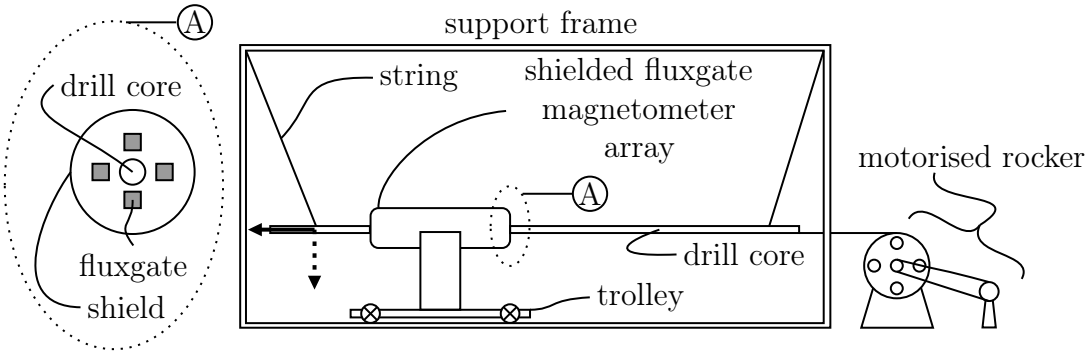


Figure 2.5: A diagram of a measurement system designed for the measurement of axial remanent magnetisation of long sediment cores. The directions of the radial and axial components of magnetisation are illustrated by the vertical dashed arrow and bold horizontal arrow, respectively. Source: Adapted from Figure 1b in Noel, Pickering and Molyneux (1989).

The measurement system consisted of a suspended drill core attached to a motorised rocker, an array of single-component fluxgate magnetometers, and a magnetic shield on a trolley [21]. The four fluxgates were arranged symmetrically, one above and one below the drill core, and one to the left and one to the right of the drill core as displayed by (A) in Figure 2.5.

The setup was operated by rocking the drill core at a constant rate and performing incremental measurements. A discrete Fourier transform facilitated the extraction

of the axial component of magnetisation associated with the fundamental frequency [21]. By analysing subsequent harmonics of the output, information on the uniformity of the magnetisation was recovered in the same way as a spinner magnetometer [21].

Noel, Pickering and Molyneux recognised that deconvolving the response of the magnetometer would aid in improving the accuracy of the measurements as it would be possible to recover the magnetisations, of the unknown distribution of magnetic dipoles, measured near the drill core without the influence of the response of the magnetometer [21].

The two prototype measurement systems rely on magnetic shields to attenuate the ambient magnetic field to reduce the effect of an induced magnetisation on the magnitude and direction of the remanent magnetisations in drill cores. It is possible to exploit the presence of the ambient magnetic field to gain information on the induced and remanent components. For example, a system proposed by Foss, Leslie and Stuart relied on the presence of the ambient magnetic field to discern between the contributions of the remanent and induced magnetisations in moderately to strongly magnetised samples from banded-iron formations [9].

The measurement system, presented in Figure 2.6, consisted of a three-component fluxgate magnetometer, a holder for the fluxgate, and a potentiometer with a string that was used to associate a position along the drill core with a measurement from the magnetometer [9].

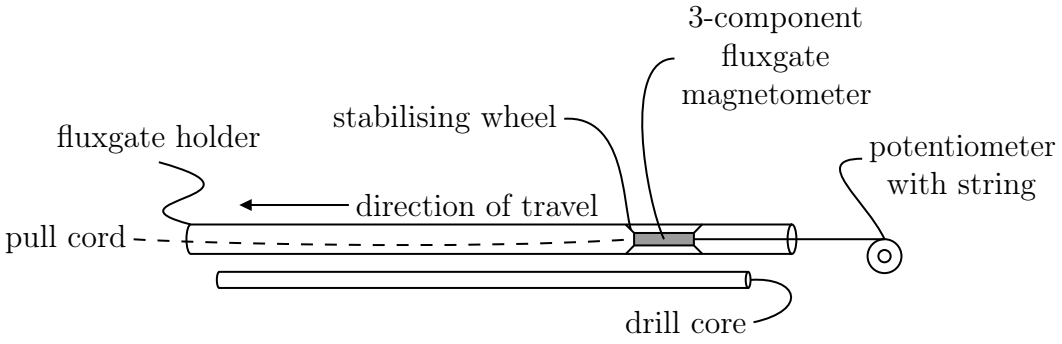


Figure 2.6: A measurement system for the determination of remanent and induced magnetisation along drill cores proposed by Foss, Leslie and Stuart (2015).

The instrument was operated by pulling the fluxgate alongside a drill core. After data was acquired, the drill core was rotated by 90° and new measurements were taken for the full length of the core. This process was repeated, in 90° increments, until the drill core had rotated through 360°. If the magnetisation of the drill core was predominantly induced *or* a component of the remanent magnetisation was parallel to the main axis of the drill core, a rotation about the main axis of the drill core would not change the output of the magnetometer (these components are rotationally invariant) [9]. In contrast, the component of magnetisation perpendicular to the main axis of the drill core would change the output of the magnetometer if the drill core was rotated.

Foss, Leslie and Stuart pointed out that the fluxgate was very sensitive to misalignments in position - for example, a rotation as small as 20 µrad would result in a 1 nT change in the output of a fluxgate [9]. Special attention must be paid to reducing the vibration and rotation of the fluxgate as it is pulled past the drill cores [9].

2.5 Motivation

The preceding discussion highlights that commercial systems for the measurement of remanent magnetisation only accommodate small samples of rock - except the SRM, which can be modified to support the continuous measurement of *sedimentary* cores (u-channel method). Igneous drill cores, from the BIC, for example, would not work with the u-channel method.

The prototype instruments highlighted in the literature only focused on the measure of a single component of the remanent magnetic field in the detection of magnetic field reversals Heye and Meyer (1972), were only concerned with the determination of a single component of the remanent magnetisation Noel, Pickering and Molyneux (1989), or were focused on the determination of the remanent and induced magnetisation, in the presence of an ambient magnetic field Foss, Leslie and Stuart (2015).

A system for the rapid measurement of drill cores would require as minimal user

intervention as possible. Although promising, the prototype instruments reviewed in this chapter require too much user intervention - loading the cores onto the suspended rocker, in the setup by Heye and Meyer, for example.

The instruments presented have highlighted that there was interest in the measurement of remanent magnetisation in complete drill cores in the 19070s and 1980s. Apart from the system developed by Foss, Leslie and Stuart, it seems that interest in this area of research has diminished. Consequently, a modern "off-the-shelf" solution was not found for the *rapid* detection of geomagnetic reversals recorded in *continuous*, igneous, drill cores.

The next chapter focuses on the development of a framework that will guide the investigation.

Chapter 3

Investigative Framework

The problem identified by the investigation is defined, and the framework used to conduct the investigation is described.

With the context of the previous chapter, there is a need for an instrument that can rapidly measure the remanent magnetic field originating from continuous, non-sedimentary, drill cores and provide information that can be used to set aside sections of core for palaeomagnetic study. The need for a more focused point of investigation is required to constrain the scope of the problem.

3.1 Investigative Question

From the intended application of the measurement system, a more focused investigative question is formulated:

> Can changes in the direction and intensity of the permanent magnetic field originating from continuous drill cores be detected and used for the identification of magnetic field reversals recorded by the magnetisation in the cores?

To address the investigative question, the ability of a measurement system to

reject ambient magnetic fields and facilitate the measurement of the direction and intensity of magnetic fields significantly smaller than the ambient magnetic field must be evaluated. In doing so, it is necessary to understand the influence that a magnetic shield has on the ambient field and measurements taken within the shield. This knowledge can be applied to the design of a measurement system that will be used to search for geomagnetic reversals recorded in continuous drill cores. The response of the system can be assessed with synthetic drill cores to address the investigative question. In doing so, limitations of the setup are also identified.

3.2 Research Strategy

The approach used to conduct the investigation involved two significant components. The first component consisted of requirement identification, FEA modelling, and validation with synthetic drill cores, while the second component focused on the measurement of short sections of real drill core:

- The requirements and design of the measurement system are discussed, and the components used in the setup are selected.
- Optimisation of the component placement was done through the use of a magnetostatic FEA of a magnetic shield exposed to an ambient magnetic field. In this model, the non-linear effects of the shielding material were accounted for, and the magnetic field inside the shield was computed.
- The numerical model of the shield was validated by experimental measurement.
- Synthetic drill core samples and short sections of real drill core samples were run through the measurement system.

Once this process was concluded, the investigative question was answered, and shortfalls and recommendations were identified.

The points mentioned above are expanded upon in the subsequent sections below.

3.2.1 Requirement Analysis and Component Selection

A concise discussion and motivation for the application of a portable measurement system that could be used to address the investigative question is presented. With this context, the requirements and performance characteristics of such a system are highlighted in **Chapter 4**.

3.2.2 Magnetic Shield Simulation and Validation

A quantification of the nature of the magnetic flux density in and around a magnetic shield exposed to an ambient magnetic field is an important consideration in the design of the measurement system. The measurement limit in the detection of small magnetic fields is controlled by the residual field in the magnetic shield.

A model that quantifies the magnetic flux density in and around a magnetic shield was developed and solved in Elmer FEM, an open-source multiphysics FEA programme [34]. The method used to create the input geometry and the FEA results were detailed in **Chapter 5**. The complete mechanical and relevant material properties of the magnetic shield, and FEA input geometry and configuration are found in **Appendices A** and **B**, respectively. The specifications of the compute cluster used to run the FEA codes, memory usage, and runtime are detailed in **Appendix C**.

Measurements were used to validate the results from the FEA. The method used to collect the results is detailed in **Chapter 6**.

3.2.3 Measurement of Real and Synthetic Drill Cores

The development and application of synthetic drill cores, used to test the measurement system with known inputs, along with the method for collecting data from short sections of real drill cores from the BIC, are discussed in Chapter 6. The results from these experiments, as well as others, are presented in Chapter 7.

The next chapter presents an analysis of the requirements of a measurement system designed to answer the investigative question.

Chapter 4

Measurement System Design

The use case for a measurement system that does not commercially exist is presented, and the value of such a system is highlighted. The requirements of the system and a high-level proposal for the design of the measurement system are given.

By contextualising the application of a measurement system, the requirements to develop such a system are identified.

Figure 4.1 depicted two researchers, surrounded by 900 m of drill core, conducting susceptibility measurements inside a storage facility as an alternative to down hole measurements. South Africa has an abundance of cores where boreholes have not been geophysically surveyed. If a study aimed to analyse the geomagnetic field recorded in drill cores during a transition in the direction of the field, the depths delineating the transition region needed to be approximately identified, with a measurement system, at the storage facility. The borehole core could then be sampled for detailed palaeomagnetic studies to examine detailed changes in direction during a reversal that can be compared with more recent reversals. The core would have to be carefully put together for relative orientation. If the dip and strike of contacts are known, the absolute orientation of samples may be

possible. The palaeomagnetic analysis would be performed on them in a traditional palaeomagnetic laboratory.



Figure 4.1: Professors Susan Webb and Lewis Ashwal, surrounded by 900 m of Bellevue drill core, performed magnetic susceptibility measurements in the National Core Library hosted at the Council for Geoscience, Donkerhoek, Pretoria. Reproduced with permission from Ashwal, Webb and Knoper (2005).

Upon completion of the BVDP, 2.5 km of drill core will be available for study. Letts et al. found that seven geomagnetic reversals were recorded in the Eastern Lobe of the BIC, but the *exact* location of the polarity transitions remains poorly constrained [5]. No commercial measurement system currently exists to assist in the selection of discrete samples for removal from the storage facility for palaeomagnetic study in a laboratory [5]. A full analysis of all 2.5 km of drill core with existing instruments would require the cores to be subdivided into more than 110 000 samples. The probability of arbitrarily selecting samples that recorded the geomagnetic field *during* a reversal event is exceedingly low. The application of a measurement system that addresses this issue is presented in Figure 4.2.

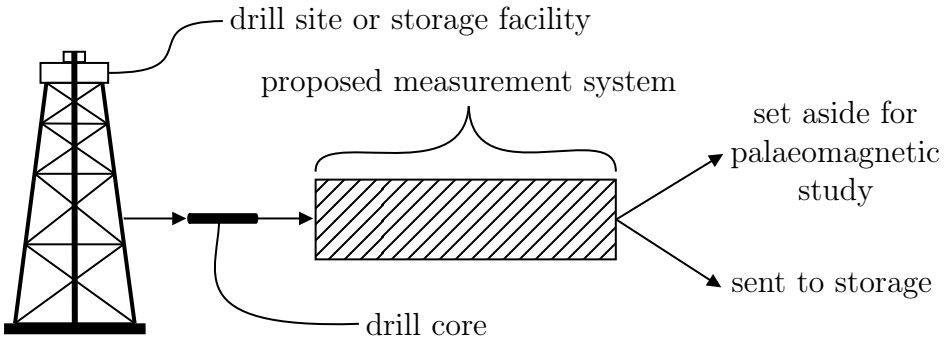


Figure 4.2: A diagram illustrating the intended application for an instrument used to rapidly identify sections of drill core that would be set aside for palaeomagnetic study.

4.1 Requirements

With the greater context of the proposed measurement system established, the two main design requirements for a proof of concept system emerged as

1. The ability to detect changes in the direction of magnetic fields in drill cores;
2. operation in environments with unwanted magnetic fields.

Secondary requirements, while not important for a proof of concept design, were considered for the design of the instrument as primary design requirements that hindered the implementation of the secondary requirements would render the system unusable in a real measurement campaign:

1. Robust and portable;
2. rapid operation.

These four points are expanded in the subsequent sections below.

4.1.1 Detect Changes in the Direction of Magnetic Fields

To identify a change in the direction of the magnetic flux density associated with the recording of a geomagnetic reversal in the magnetisations of drill cores, the smallest magnetic field expected to be encountered by the measurement system

should be established. Changes in the direction of a magnetic field are detected by a vector magnetometer, and the type of magnetometer required by the measurement system was selected based on the minimum flux density and resolution required.

With the use of a spinner magnetometer, Letts et al. measured the NRM of rock samples taken from the Main Zone in the Eastern Lobe of the BIC [5]. The Main Zone is a part of the Rustenburg Layered Suite shown in Figure 1.1. The samples were cylindrical and had a volume of $\sim$40.5 cm^3 [5]. Some of these samples had recorded a reversal in the geomagnetic field of the Earth [5].

One of the samples, measured by Letts et al., had the weakest magnetisation of all the samples in the Eastern Lobe [5]. These samples were also located near the BVDP drill site, which meant that the samples provided data that would be useful to establish a lower bound on the expected measurement range of the proposed measurement system.

If the magnetisation of a rock sample can be approximated by a singular magnetic dipole moment, the magnetic flux density measured near the dipole moment is estimated by Eq 2.6 if the volume of the sample is known. The minimum and maximum magnitudes of the magnetic flux density around a magnetic dipole moment occur at points of measurement located perpendicular and parallel to the axis of the dipole moment, respectively.

With this in mind, the minimum and maximum magnetic flux densities expected to be measured at distances of 20 mm and 40 mm away from the dipole moment were approximated using Eq 2.6 and tabulated in Table 4.1, below.

Table 4.1: A table of results presenting the approximate magnitude of the magnetic flux density measured by a magnetometer positioned at varying distances (r) and angles (θ) from an idealised magnetic dipole moment based on NRM measurements of rock samples taken from the Main Zone in the Eastern Lobe of the BIC, by Letts et al. NRM measurements compiled from Table 2 in Letts et al. (2009).

		$r = 20$ mm		$r = 40$ mm	
Sample	NRM (A/m)	$B_{\theta=0^\circ}$ (nT)	$B_{\theta=90^\circ}$ (nT)	$B_{\theta=0^\circ}$ (nT)	$B_{\theta=90^\circ}$ (nT)
Min	0.02	20.3	10.1	2.53	1.27
Avg	7.59	7690	3850	961	481
Max	28.87	29 300	14 600	3660	1830

Assuming measurements are made, in the worst case, perpendicular to the dipole moment at a distance of 40 mm, the results in Table 4.1 indicate the proposed measurement system would be required to resolve changes in the direction of the magnetic flux density on the order of a few nT.

With the minimum magnetic flux density approximately calculated, a decision on the type of magnetometer employed in the measurement system could be made. Numerous magnetometers exist, but the fluxgate and SQUID magnetometers are the most prominent high-performance vector devices in terms of sensitivity and noise.

SQUID magnetometers are extensively used in palaeomagnetic studies due to their extreme sensitivity and ultra-low noise. However, SQUID magnetometers are exclusively used in laboratories and are not readily portable due to their fragility.

On the other hand, fluxgate magnetometers provide a portable and rugged solution that does not perform as well as SQUIDs magnetometers but still offers attractive noise floors and sensitivities. Fluxgates have a larger measurement range than SQUIDs, which is beneficial for the measurement of strongly magnetised drill cores.

Two fluxgate magnetometers with different measurement ranges and sensitivities were selected for the investigation (Table 4.2).

The selection of two sensors with different measurement ranges ensured that if the measurement range of the more accurate and precise FGM3D/250-3C was exceeded, the FGM3D/1000 would still provide measurements. The use of two three-component sensors allowed for operation as a gradiometer if required. This setup would enable the system to eliminate homogenous residual background fields and respond only to magnetic field gradients between the sensors.

Wider bandwidth sensors were desirable as the signal-to-noise ratio of a signal contaminated by noise from a stochastic process could be improved by averaging the measured signal at the expense of reduced bandwidth [36].

Table 4.2: A table of selected specifications for the two fluxgate sensors manufactured by Sensys GmbH, used in the investigation. Specifications adapted from [37] and noise measurements were compiled from certification reports of the individual sensors.

Sensor	FGM3D/250-3C	FGM3D/1000	Unit
Measurement range	±250 000	±1 000 000	nT
Sensitivity	0.04	0.01	V/µT
Rel. measurement error	±0.1	±0.5	%
Noise (1 Hz)	17.6 ≤...≤ 19.2	18.1 ≤...≤ 21.2	$pT_{RMS}/\sqrt{Hz}$
Resolution	< 150		pT
Temperature drift	≤ ±0.3		nT/K
Bandwidth (3 dB)	2		kHz

The fluxgate sensors output an analogue signal, and a Data Acquisition System (DAS) was specified to facilitate the acquisition of the data - specified in Table 4.3.

Table 4.3: A table of selected specifications for the data acquisition system manufactured by Sensys GmbH, used in the investigation. Specifications adapted from [38].

Parameter	Value	Unit
Resolution	24	bits
Measurement input range	±10	V
Sampling rate	0.2 to 2	kHz
Analogue AA LPF bandwidth (3 dB)	48	kHz
Number of 3-component sensors	5	
Temperature compensation	Yes (0 °C to 40 °C)	
Output	UDP & Serial	

The DAS timestamped and output the digitised data in real-time, over the network via the User Datagram Protocol (UDP). Data from the network was recorded and saved by a computer program. Real-time output of the data was important as the ability to monitor the response of the sensors to drill cores and changes in environmental conditions allowed for quality control and stopping of the measurement campaign due to environmental sources (a car driving past the measurement system, for example).

The TDX analogue-to-digital converters quantised the input signal in 1.192 µV increments from the input range and the resolution given in Table 4.3. The FGM3D/250-3C and FGM3D/1000 had sensitivities of 0.04 V/µT and 0.01 V/µT, respectively - Table 4.2. For two ideal fluxgates with the given sensitivities, the smallest fields resolvable by the TDX were 29.8 pT and 119.2 pT. The resolution for the procured fluxgates was stated to be < 150 pT, so the minimum detectable change in the magnetic flux density was limited to 150 pT.

An inspection of Eq 2.6 shows an inverse cubic relationship between the strength of the magnetic flux density and the distance between the measurement point and the magnetic dipole moment. The fluxgate magnetometer sensors should be placed as close to the drill cores as possible to improve the strength of the magnetic field associated with weakly magnetised drill cores.

The operating environment of the sensors significantly influenced the ability of the measurement system to resolve changes in magnetic field direction. The next section focused on designing the system to tolerate unwanted magnetic fields while maintaining the capability to detect changes in the direction of the weak magnetic fields.

4.1.2 Tolerance Toward Stray Magnetic Fields

If a rock sample is exposed to an ambient magnetic field, the magnetic flux density measured near the sample is the vector addition of the magnetisation induced in the sample, the permanent magnetisation of the sample, and the ambient magnetic field. The direction of the remanent magnetisation will be altered by the presence of the induced magnetisation.

The induced magnetisation in an arbitrary rock sample (under the assumptions that the material responds linearly to the inducing field, has an isotropic susceptibility, and the effects of self-demagnetisation are negligible) is given by

$$M_{\text{indu}} = \kappa_v H = \kappa_v \cdot \frac{B_{\text{ambi}}}{\mu_0(1 + \kappa_v)} \tag{4.1}$$

where H is the strength of the inducing field in A/m, κ_v is the dimensionless volume magnetic susceptibility, μ_0 is the magnetic permeability of free space, and B_{ambi} is the magnetic flux density, in T, of the ambient magnetic field measured near the rock sample.

If the direction of the magnetic flux density associated with the remanent magnetic field is to be measured, the contribution of the induced magnetisation to the change in direction of the net magnetic flux density must be negligible. The extent to which the ambient geomagnetic field can be attenuated is the factor controlling the limiting detectability of the direction of the magnetic flux density associated with weakly magnetic samples.

Equation 4.1 shows that increasing the magnetic susceptibility or ambient magnetic flux density causes the induced magnetisation to increase. The only method to reduce the induced magnetisation is through the attenuation of the ambient magnetic field. Palaeomagnetic laboratories use magnetic shielding, installed around the entire laboratory, to reduce the ambient field to a few hundred nT. Instruments, like SRMs, have additional shielding to further attenuate the ambient field and create ultra-low field regions.

In contrast, drill core storage facilities make no effort to reduce the ambient magnetic field - sheet metal roof panels and metal drill core holder trays are seen in Figure 4.1. In such areas, the ambient magnetic field will impart an induced magnetisation in the samples that may alter the direction of the remanent magnetisation. An important aspect of the proposed measurement system was the creation of an environment that contained a magnetic field significantly weaker than the ambient magnetic field. This is achieved with magnetic shielding.

A two-layer, cylindrical magnetic shield with a length of 900 mm, received from the Geological Survey of Norway, was used in the investigation. Existing literature indicated that a dual-layer shield of this length would attenuate the ambient field below 100 nT [39, 40]. Although significantly lower than the ambient geomagnetic field, the field inside the shield was preferred to be below the minimum flux density expected to be measured near a rock sample, as determined in Table 4.1.

4.1.3 Robust and Portable

The proposed measurement system was intended for use in drill core storage facilities. A final version of the system would be required to cope with the shock and vibration associated with transportation to and from these facilities as vibration and mechanical damage degrades the performance of magnetic shields - see Kamens and Koren (1987) in Further Reading.

4.1.4 Rapid Operation

A Polyvinyl Chloride (PVC) pipe was used to support the drill cores that passed through the measurement system. The pipe should not be in contact with the magnetic shield or fluxgate magnetometers to prevent the transfer of mechanical vibration to these components. For a measurement system intended for field use, improvements to this setup are discussed in **Chapter 7**.

4.2 Proposed Design

The design for a measurement system intended to address the investigative question is presented in Figure 4.3.

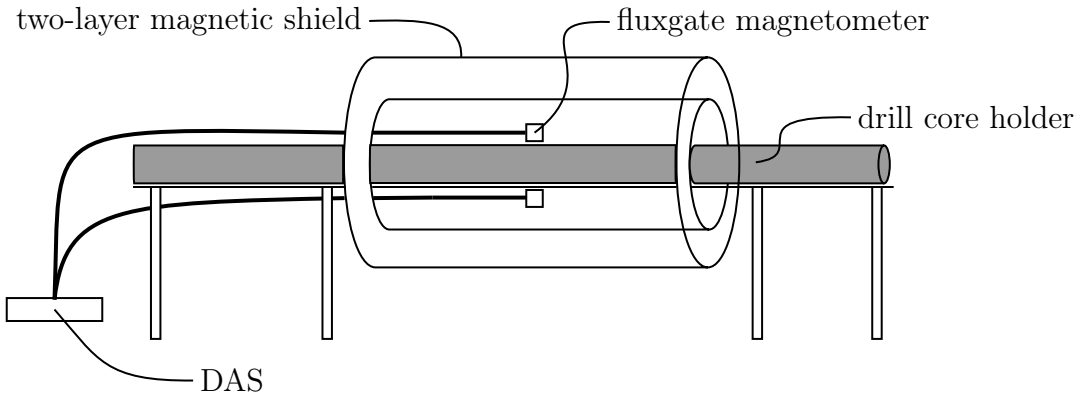


Figure 4.3: A diagram of the proposed measurement system with a second fluxgate magnetometer introduced to facilitate operation as a magnetic gradiometer.

The next chapter analyses the residual magnetic field inside the magnetic shield

used in the proposed measurement system.

Chapter 5

Magnetic Shield Finite Element Analysis

The development of a numerical model designed to evaluate the effectiveness of a two-layer magnetic shield exposed to an ambient magnetic field is presented. In doing so, a complete and open-source workflow is established for the mesh generation, numerical computation, and visualisation of the simulation result. An upper limit on the number of mesh elements used to discretise the magnetic shield in the FEA is identified.

Before the development of the measurement system commenced, the ability of the magnetic shield to attenuate the ambient magnetic field was investigated. This was done because the shield formed a critical component of the proposed system, and if the performance of the shield was unsatisfactory, a different approach in the design of the system would have to be taken.

Schematics supplied in a report from the Norwegian Geologic Survey, Torsvik and Olesen (1988), suggested that a shield with dimensions similar to the one used in the investigation would create a region where the magnetic flux density was below 100 nT [40]. While this represented a significant reduction compared to the

ambient field, typically on the order of tens of thousands of nanotesla, it remained higher than desired. Ideally, a field-free environment was preferable, however, a uniform residual magnetic field below the minimum predicted magnitude of measurement, determined in Table 4.1, was acceptable. Large ambient fields would impart appreciable induced magnetisations in high-susceptibility rock samples that dominate the magnetic field measured by a magnetometer and lead to incorrect representations of the remanent magnetisation. The ambient field inside the shield was required to be as uniform as possible since gradients would reduce the effectiveness of operating two fluxgate magnetometers as a gradiometer.

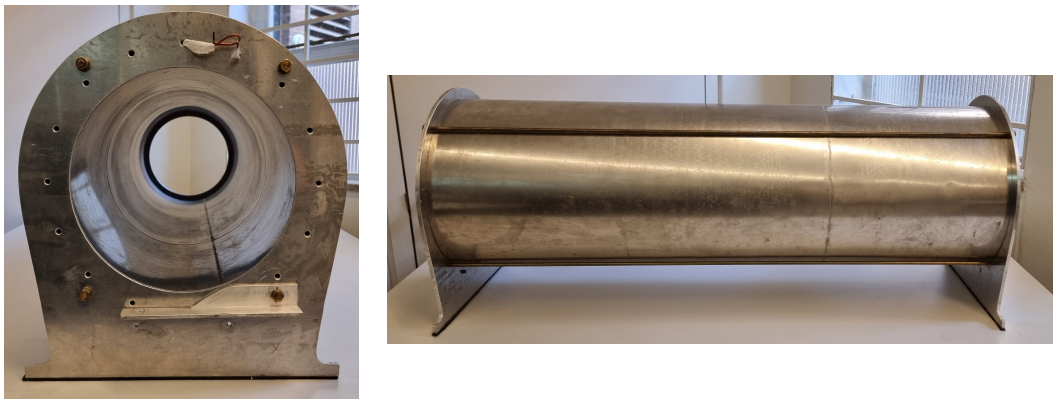
From the information required for an analysis of the residual field in the shield, an FEA of the magnetic shield was performed as it was the most appropriate type of numerical analysis for the application (complex geometry and non-linear material properties).

5.1 Modelling and Meshing

The computational model was developed from the magnetic shield proposed for use in the investigation - Figure 5.1. The shield was made up of two concentric cylinders fabricated from 1 mm thick rolled sheets of a high permeability alloy (HPA) known as ASTM A753 Alloy 4 (MUMETAL®) [42]. The end plates that held the cylinders in place were made from aluminium; one end plate is visible in Figure 5.1a. The end plates were kept in place with brass rods, visible in Figure 5.1b. Mechanical drawings of the magnetic shield are supplied in **Appendix A**.

Table 5.1 compares the relative magnetic permeabilities of the three materials that constituted the magnetic shield. The HPA predominantly determined the effectiveness of the magnetic shield. Consequently, the geometric complexity of the model was simplified by opting to leave the ends of the shield open through the exclusion of the brass rods and aluminium end plates. The welded seams, visible in Figure 5.1, were also excluded from the simulation, and the cylinders were assumed to be perfectly cylindrical and free from deformities.

To create a high-fidelity representation of an arbitrary geometry, a sufficient number



(a) Front view. (b) Side view with brass rods visible.

Figure 5.1: Different views of the magnetic shield proposed for use in the investigation.

of finite elements are required to approximate the geometry of the object. Poor discretisation of a model with finite elements will lead to inaccurate results from FEA codes. In general, the largest element size for the accurate approximation of a region of interest requires that the elements be smaller than the smallest dimension of the smallest detail in the region. Ideally, the largest minimum element size should be used to reduce computation time and resource requirements.

Table 5.1: A table comparing the relative permeability of the different metals found in the magnetic shield used in the investigation.

Material	Relative permeability (μ_r)	Source
ASTM A753 Alloy 4	>250 000	[42]
Brass	1.03–1.06	[43]
Aluminium	1.00002	[44]

For an accurate representation of the two HPA layers, elements inside and immediately surrounding the layers are required to be no larger than 1 mm in all dimensions. The largest minimum element size can be determined by performing several simulations and varying the element sizes - a convergence study. Comparison of these results will identify the least compute-intensive simulation while preserving the desired accuracy.

The entire model cannot be discretised with elements of the same size as the

computation cost will become exorbitant. A means of controlling the size of elements in different parts of the model must be employed - local mesh refinement. For the case of the magnetic shield simulation, finite element size gradients, dependent on position, were created by explicitly setting the number of nodes on the lines bounding the geometries - transfinite curves [45]. By defining the number of equidistant nodes on an arbitrary bounding line, the spacing between nodes is set, which loosely controls the size of the mesh elements around the transfinite curves.

Element size gradients help to gradually shrink or grow the size of the mesh elements. Abrupt changes in element size can lead to distorted and ill-formed elements near the interface where the size changes.

Referring to Figure 5.2, the mesh element size is largest near the edges of the simulation boundary (discretisation domain) and smallest between the HPA layers. The mesh size for the innermost region of the magnetic shield (internal transition region) is smaller than the discretisation domain elements but larger than the elements between the HPA layers.

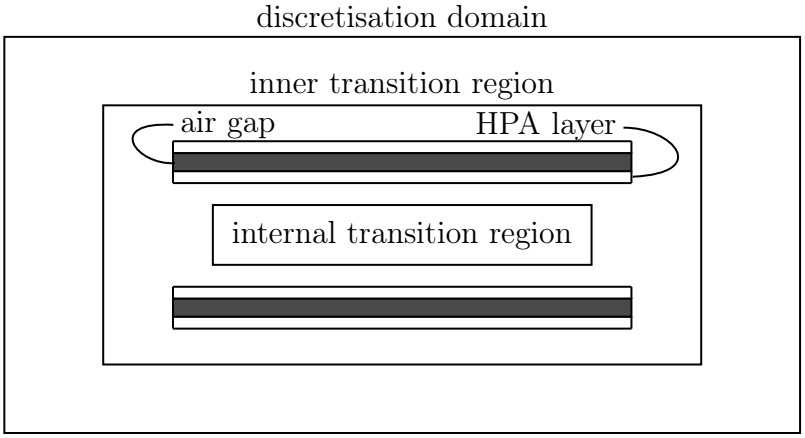


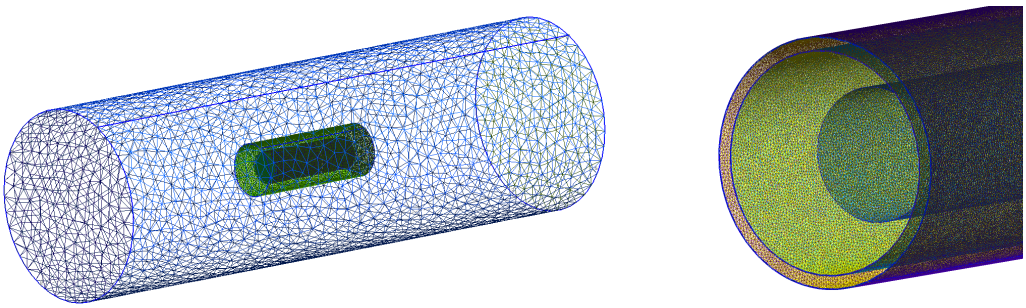
Figure 5.2: A simplified, not to scale, diagram depicting a cross-section of the geometry used to represent a two-layer cylindrical magnetic shield. The annotations indicate areas in the model where the mesh size was controlled with transfinite curves.

The high element density around the HPA layers exists for two reasons. First, it allows for the element size to be lowered around the area immediately surrounding

the shield. This is important so that the interaction between the ambient magnetic field and the shielding material is accurately captured. Second, it makes the element size gradient that exists between the simulation boundary (discretisation domain) and the edges of the HPA less steep, which aids in numerical convergence of the FEA by reducing element distortion [46].

The finite elements were created from an input geometry supplied to the Gmsh code [47]. The mesh generation operated in three states. First, the lines bounding all entities in the model were discretised, then the lines that bounded surfaces were used to generate elements lying on those surfaces [45]. Lastly, the elements that lie on all surfaces are used to generate elements in the regions enclosed by the surfaces [45].

For the 2D element generation, Figure 5.3, an implementation of the Delaunay algorithm was used as this algorithm performed well with many plane surfaces and complex element size gradients [45]. For the 3D element generation, a parallel implementation of the Delaunay algorithm, called `HXT`, was used as it was more efficient in terms of memory usage and execution time compared to other sequential implementations [45].



(a) With bounding region. (b) Without bounding region.

Figure 5.3: Different views of the mesh representing the two-layer magnetic shield used in the FEA. For visibility, only the 2D mesh elements are shown. The innermost cylinder in (b) is the region referred to as the "internal transition region".

Four meshes with different element counts (5 M, 36 M, 81 M, and 95 M) were created by varying the number of points along the transfinite curves - the settings for each mesh are given in Table 5.2 and these region names correspond to the names in

Figure 5.2. These meshes were used to evaluate the effect that the number of elements had on the FEA solution.

Table 5.2: A table listing the number of points on the transfinite curves, used in the generation of the input mesh for the FEA of the magnetic shield, for meshes with various element counts. Lines 50 to 59 in Listing B.2 correspond to the transfinite curves that were modified with the values given in this table.

	5M	36M	81M	95M
Discretisation domain	40	80	100	100
Inner transition region	60	120	160	160
HPAs and air gaps	200	400	600	685
Internal transition region	125	250	250	200

The extent to which elements in a mesh deviated from their respective idealised shape was used to evaluate the effectiveness of increases in the element count on the quality of the elements. The mesh quality was checked with a Python Application Programming Interface (APIs) exposed by Gmsh and the Verdict library (integrated in the Visualization Toolkit software) [47, 48, 49, 50]. In general, the difference between the shape of the mesh elements and the corresponding ideal shapes decreased as the number of elements increased.

Once the complete mesh was generated, it was partitioned into 96 partitions to facilitate the execution of the FEA code in a distributed compute environment. The method of concurrent execution reduced the time taken for the simulation to converge.

5.2 Finite Element Analysis

Elmer FEM is a collection of open-source multiphysics codes that are used to evaluate a range of physical phenomena [34]. To run an analysis using these codes, at least one solver, input mesh, material properties, and boundary conditions are required.

For the application of a magnetic shield simulation, a magnetostatic solver was used for the numerical evaluation of the solution of Maxwell's equations in the

A-V potential form [51].

A magnetodynamic solver is also available. Since the geomagnetic field of the Earth changes slowly over time, it was assumed that the field remained constant over short periods. The complete solver input file is presented in Listing B.3.

The simulation of the magnetic shield made use of two material types, viz., air and ASTM A753 Alloy 4. Every object in the simulation was set to air apart from the two HPA layers.

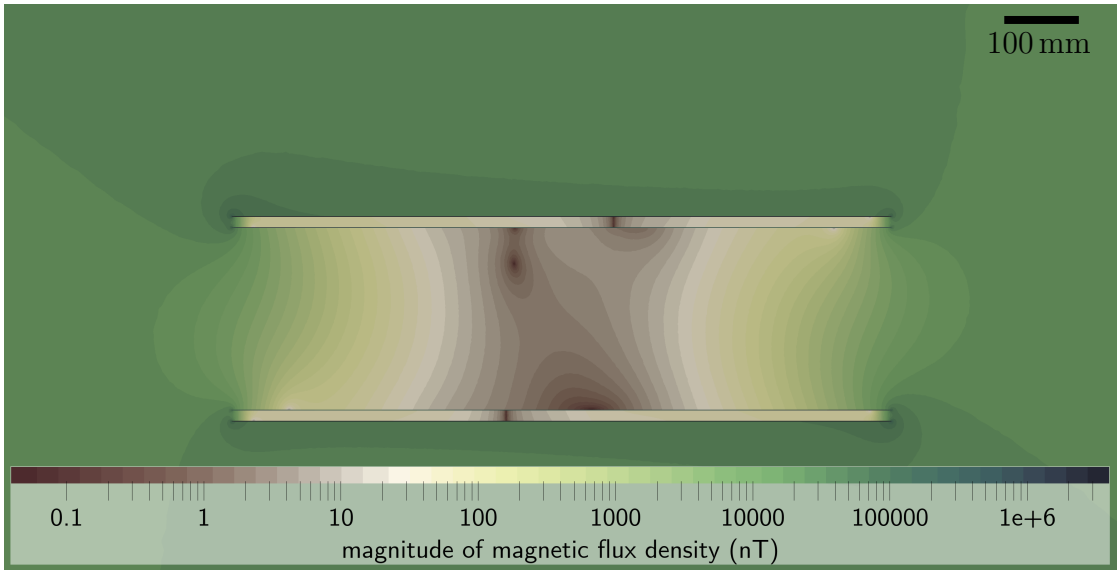
Due to the non-linear relationship exhibited by the induced magnetisation in the HPA in response to an inducing field, it was important to find material data for this relationship where the data was obtained for a DC or low frequency BH relationship and a material thickness of 1 mm. The material data most closely matching these criteria was experimentally measured by Arpaia et al. for a 1.7 mm -thick sample with a constant inducing field [52]. The preprocessing required for Elmer FEM to use this material data is found in **Appendix A**.

One set of boundary conditions was applied to the outermost region of the mesh to facilitate the generation of a constant ambient geomagnetic field in the FEA. The ambient field used in the simulations had the parameters derived from measurements made with a fluxgate magnetometer, used to validate the simulation in **Chapter 6**, at the location (Physical Properties Lab, Geosciences building, University of the Witwatersrand, Johannesburg) of the magnetic shield (inclination of $-64.0°$, declination of $-12.4°$, and an intensity of 22 792.9 nT). Slices of the residual field along the main and minor axes of the magnetic shield, Figure 5.4, were derived from the simulation results with the use of ParaView [53].

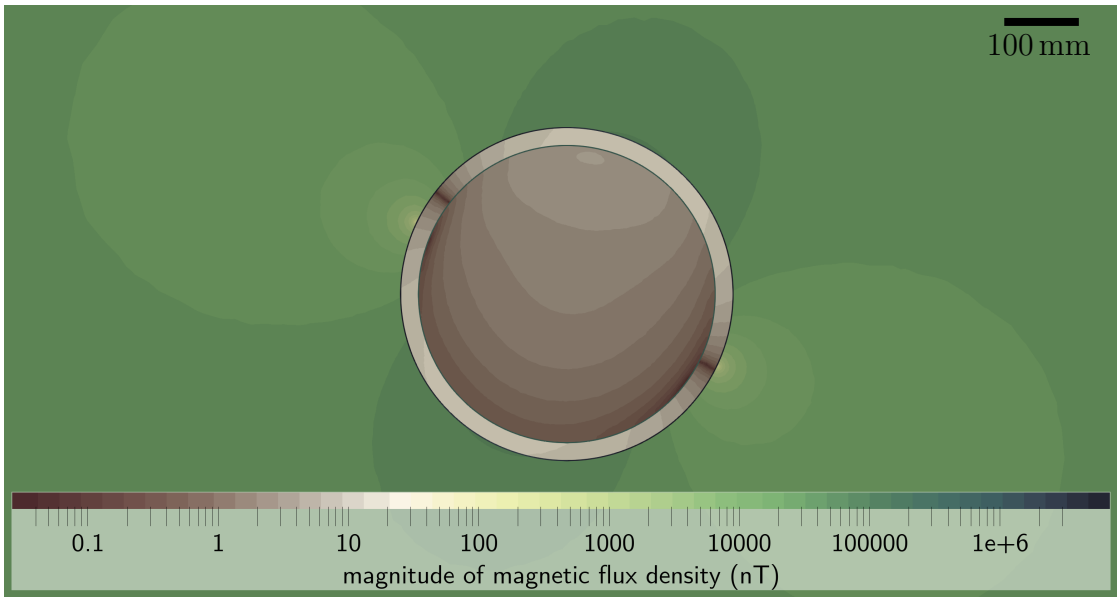
As mentioned, the number of elements used to create the mesh that represented the magnetic shield was varied, and the results from these simulations were compared to facilitate the identification of the least number of finite elements required to discretise the magnetic shield without impacting accuracy. Figures 5.5 and 5.6 present plots of the magnetic flux density as a function of position along the main axis of the magnetic shield while the number of elements used to discretise the shield was varied.

Figure 5.5 shows that all the input meshes produce results that exhibit the same large-scale behaviour while Figure 5.6 shows subtle differences between results associated with the four input meshes. Notably, the global magnetic flux density minima increases from about 2 nT (for the 5 M mesh) to about 6 nT (for the 81 M mesh), then decreasing to about 3 nT (for the 95 M mesh). The position of the minimum for the 95 M mesh also shifts towards the left of the shield. These changes in magnitude and position of the minima are likely associated with changes in element size gradient, in the input meshes, and are non-physical in nature. The results from these simulations are reconciled with experimental measurements in **Section 7.1**.

Through the process of the convergence study, the number of elements that the input mesh could contain before the FEA failed was 100 M elements. Profiles of the memory usage and run time as functions of input mesh element count are presented in **Appendix C**.



(a) Slice along main axis.



(b) Slice along minor, or radial, axis.

Figure 5.4: Main and minor axis slices of the magnitude of the magnetic flux density, coloured in 50 bins, inside a two layer cylindrical magnetic shield exposed to an ambient geomagnetic field (I:−64.0°, D:−12.4°, F:22 792.9 nT). The mesh used by the FEA contained 95 M elements.

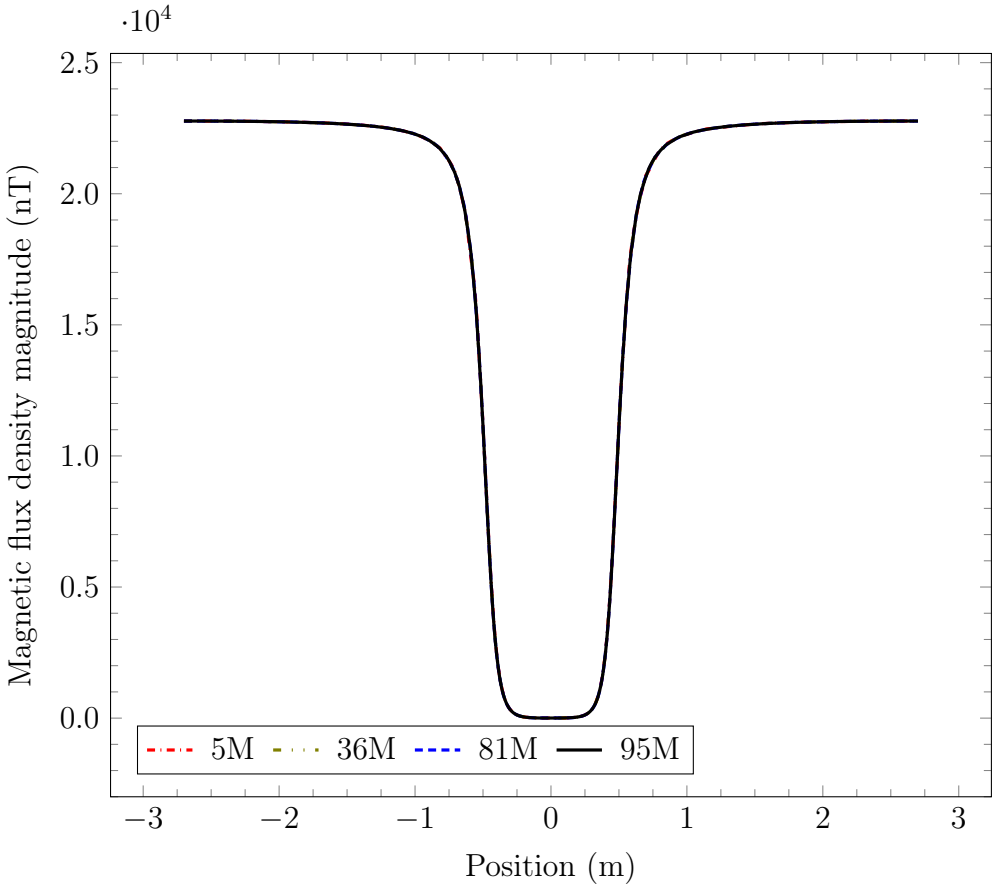


Figure 5.5: A line plot of the magnitude of the magnetic flux density along the main axis of a magnetic shield while varying the element count of the input mesh used in the FEA. The 0 m position corresponded to the midpoint of the main axis of the shield. The shield spanned from −0.447 m to 0.447 m in the plot.

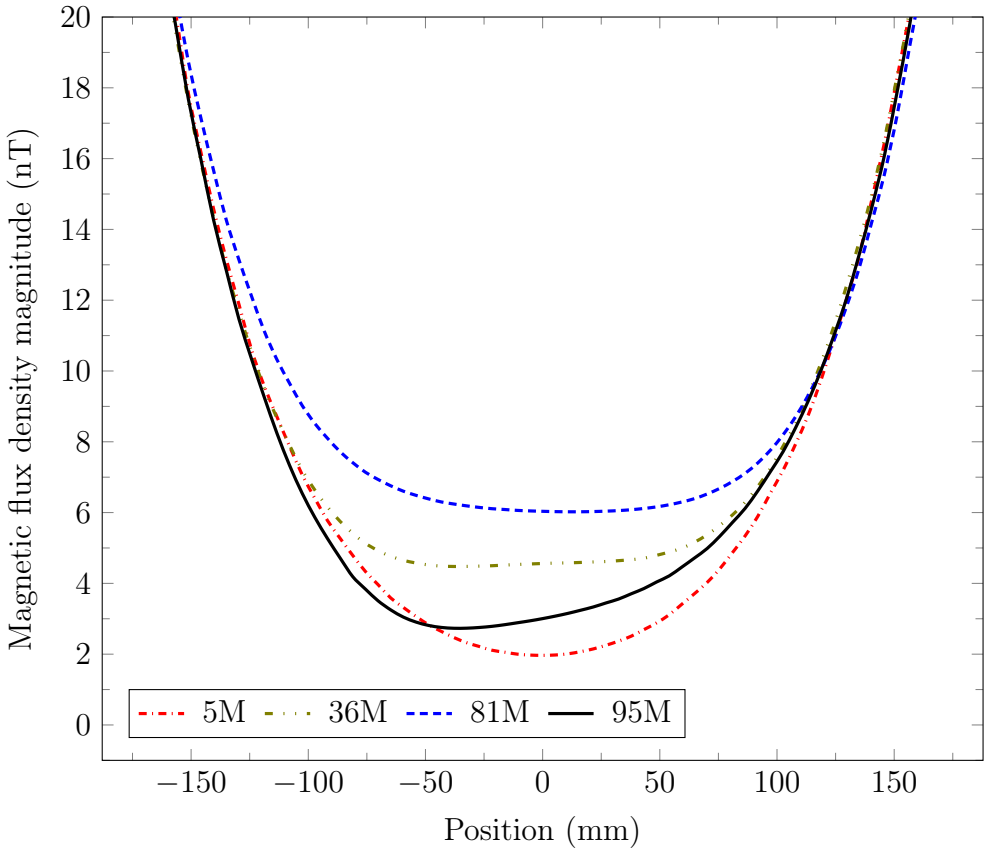


Figure 5.6: A plot of a small section of Figure 5.5, centred around the midpoint of the main axis of the magnetic shield.

The next chapter focuses on various experimental methods and associated results collected. Data from one experiment was used to validate the results from the FEA model given in this chapter.

Chapter 6

Experimental Methods

This chapter presents the standardised setup of the measurement system, the fabrication of the synthetic drill cores, and the results from the experiments used to evaluate the measurement system.

The measurement system setup was standardised for all experiments to ensure the consistency of repeat measurements and facilitate the comparison of results.

6.1 Measurement System Setup

The setup of the measurement system was controlled in three key ways.

First, the magnetic shield was positioned on a wooden table, partly depicted in Figure 6.2, with as few magnetic sources near the setup as possible. To minimise the residual field inside the shield, the shield was oriented to be as parallel to the *local* magnetic West-East direction as possible [54]. The length of the main axis of the shield exceeded the width of the wooden table, which meant it was not always possible to fully orient the shield parallel to the ambient West-East direction. The local magnetic field varied, in part, due to anthropogenic sources near the laboratory and also from the natural variation of the ambient magnetic

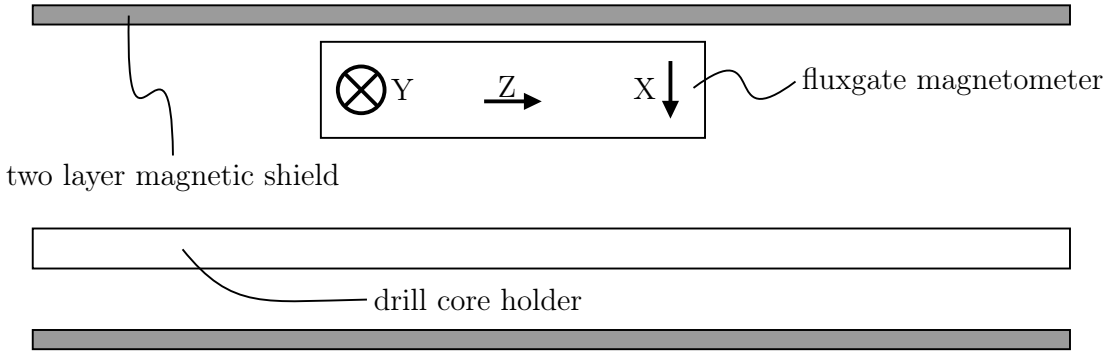
field.

Second, the same fluxgate magnetometer (Sensys FGM3D/250-3C in Table 4.2) and DAS (Sensys TDX in Table 4.3) were used to measure the magnetic flux density in all experiments. The fluxgate was positioned in the same place for each experiment and had the same orientation (depicted in Figure 6.1a). The position of the fluxgate inside the shield was kept the same for all experiments to try to mitigate the addition of different ambient field components between experiments. It was not always possible to measure the same ambient field components in the shield, as the magnetic flux density in the laboratory varied over hours and days.

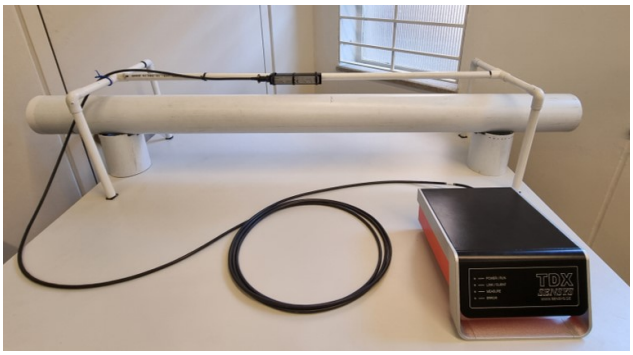
Third, the fluxgate was attached to a white Polyvinyl Chloride (PVC) stand, and the drill cores were inserted and pushed through a large diameter, white, PVC pipe - both depicted in Figure 6.1b. Heye and Meyer noted that the magnetic shield could distort the magnetic field from the drill cores [20]. The radial distance between the samples and the inner wall of the magnetic shield was maximised by aligning the main axes of the drill cores with the main axis of the shield. This was facilitated by the adjustment of the vertical height of the PVC drill core holder. The vertical distance between the fluxgate magnetometer and the drill cores was also fixed so that the magnetometer was as close to the drill cores, without touching the cores, as possible.

Equipment associated with the experiments, such as the PVC pipes, wooden table, or the wooden stick used to push samples through the measurement system, were inspected with the fluxgate magnetometer to determine if any remanent magnetisation was present. Metal brackets were found under the table and were removed before the experiments commenced.

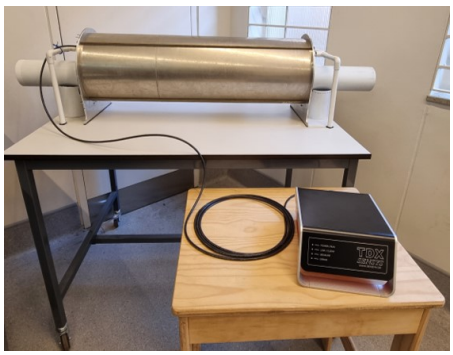
Figure 6.1c presents the complete setup used in the investigation - the metal table was not used during measurements.



(a) Cross-section of the proposed measurement system indicating the orientation of the fluxgate magnetometer.



(b) Without magnetic shield.



(c) With magnetic shield.

Figure 6.1: The components of the measurement system used in the investigation and a simplified diagram of the measurement system.

Measurements from the fluxgate magnetometer were digitised by the DAS and streamed with the UDP over a wired network. A computer program supplied with the TDX was used to set the sampling rate, number of averages, and the preferred unit (nT) associated with each measurement. The TDX only allowed a single sampling rate that was applied to all channels. The sampling rate was set to 2 kHz, while the number of averages, hence the effective sampling rate, was specific to each experiment.

The streamed data were written to permanent storage with the use of a Python script running on a computer on the same network as the TDX [50]. Another Python script plotted the measurements in real time for the operator to observe the response of the system to drill cores and to monitor the contributions of external

sources of interference to the measurements [50]. For example, the laboratory where the measurement system was operated had a magnetic door lock that visibly altered the residual field inside the shield when the electromagnet momentarily de-energised, for the door to open, and re-energised when the door contacted the electromagnet on closure.

Degaussing of the magnetic shield was periodically employed to reduce any unwanted permanent magnetisation acquired by the shield. This process was facilitated by the application of a 50 Hz sinusoidal current supplied by a variable autotransformer to a solenoid wrapped around the inner HPA cylinder of the magnetic shield. The voltage of the transformer was ramped from $0\,V_{RMS}$ to $\sim 80\,V_{RMS}$ before being ramped back down to $0\,V_{RMS}$. Approximately $80\,V_{RMS}$ was the maximum usable voltage without exceeding the power rating of the transformer connected to the setup. The setup used to perform the degaussing is presented in Figure 6.2.

An autotransformer consists of a single winding, meaning there is no galvanic isolation between the primary and secondary of the transformer. Unlike a conventional transformer, a residual current device, connected on the primary side of the transformer, would detect a current that did not return via the path offered by the *secondary* side of the transformer. For the safety of the operator, in the event of a fault, the body of the shield (with all components galvanically connected) was connected to the building earth and the supply to the primary side of the transformer was monitored by a residual current device. It is advisable that the shield not be touched during degaussing and that wearers of pacemakers (or other medical devices sensitive to electromagnetic interference) remain away from the setup during degaussing.

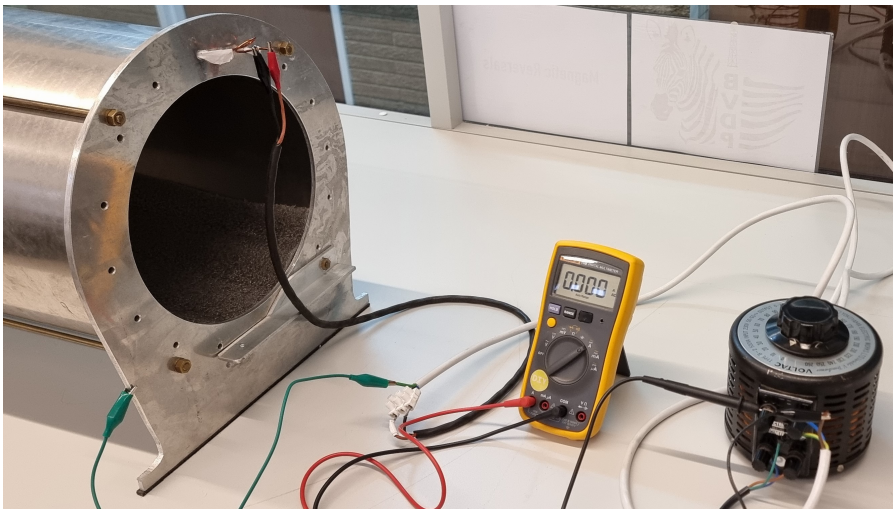


Figure 6.2: The setup used to degauss the magnetic shield. The magnetic shield is on the left side of the image, while the multimeter is in the centre and the variable autotransformer is on the right.

With the measurement system setup, the synthetic drill cores were fabricated.

6.2 Synthetic Drill Cores

The investigative question was concerned with understanding if the measurement system could resolve changes in the direction of a magnetic field to detect geomagnetic reversals recorded in drill cores. Therefore, a means to elicit a response from the measurement system to a magnetic field with a known direction was investigated. The simplest and most reproducible solution required the use of magnetic tape found in cassettes. The development of these synthetic drill cores, with magnetic tape, was inspired by the works of Heye and Meyer, 1972 and Noel, Pickering and Molyneux, 1989.

Before the creation of the cores commenced, a length of tape was removed from the cassette and passed near a fluxgate magnetometer, inside the shield, to determine if there was any remanent magnetisation. Degaussing a cassette tape that was previously magnetised proved ineffective as the coercivity of the material that carried the magnetisation was high (16–23 kA/m) [55]. The high coercivity was desirable

as it meant that the magnetisation of the cores was likely to be stable and tolerant to handling in an environment with magnetic sources - metal tables, for example. If the tape contained little remanent magnetisation, it was cut into predefined lengths (90 mm, 50 mm, 30 mm, and 20 mm) and attached to a cardboard backing with clear adhesive tape. The cores were passed near a fluxgate magnetometer to check that no remanent magnetisation was acquired during handling. If no remanence was measured, the same pole of a neodymium magnet was repeatedly dragged across each tape in the same direction. The steps involved in making the synthetic drill cores are depicted in Figure 6.3.

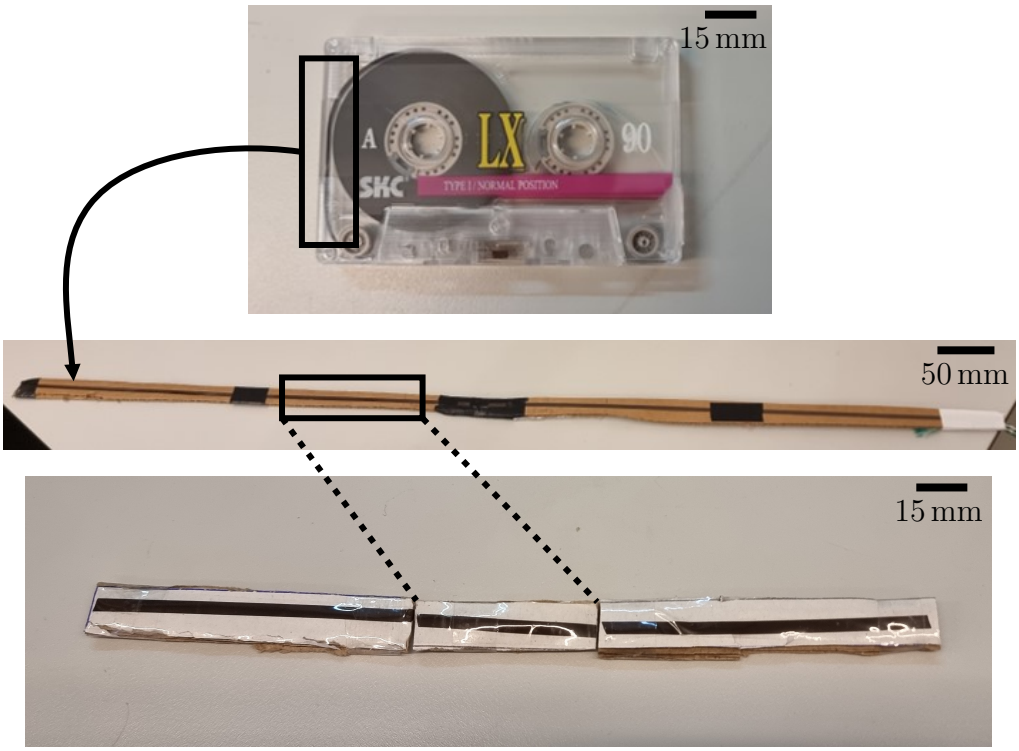


Figure 6.3: A diagram illustrating the process used to create synthetic drill cores from a cassette tape.

With the setup of the measurement system and fabrication of the synthetic drill cores complete, a series of experiments were conducted to evaluate different characteristics of the measurement system. To begin, the residual magnetic field inside the shield of the measurement system was measured with a fluxgate magnetometer.

6.3 Residual Field

Measurements of the residual magnetic field inside the magnetic shield were collected in 20 mm increments along the main axis of the shield to validate the results from the FEA.

As discussed, to facilitate direct comparison of the FEA results, the magnetic shield was positioned on a wooden table with as little magnetic materials around it as possible so that the vacuum environment, assumed by the FEA, was roughly approximated. The ambient magnetic field around the shield was recorded by a second fluxgate magnetometer and used as the boundary conditions in the FEA presented in Chapter 5.

The TDX sampled all channels with the same sampling rate and, if used, the same number of averages. The sampling rate was determined by the identification of the largest expected frequency content of the signal. The fluxgate *outside* of the magnetic shield, Sensys FGM3D/1000, was used to determine the sampling rate as the shield was effective at removing higher frequency content in the ambient magnetic field. The laboratory had electrical power outlets, so the effective sampling rate was set to 100 Hz. Therefore, for both fluxgates, the TDX was set to sample at 2 kHz and to perform 20 averages per measurement to obtain the desired effective sampling rate. The measurement reported at each 20 mm increment consisted of multiple measurements that were averaged, in post-processing, to obtain the reported result.

The specifications of both fluxgate magnetometers indicated that the X, Z, and Y sensing elements inside the housing of the magnetometer were positioned 54.50 mm, 34.50 mm, and 14.50 mm from the edge of the sensor housing, respectively [37]. This means that each sensing element does not record the magnetic field at the same position inside the shield. Corrections were made to the positions of the measurements reported by the three components so that they were correctly aligned with the position of the sensor housing along the shield.

The results, with sense element positions corrected, were plotted in Figure 6.4 and the region along the main axis, on either side of the centre of the shield,

was inspected in more detail in Figure 6.5. From these measurements, the global minimum of the magnitude of the magnetic flux density was recorded as 0.511 nT at a displacement of 11.6 mm from the centre of the chamber.

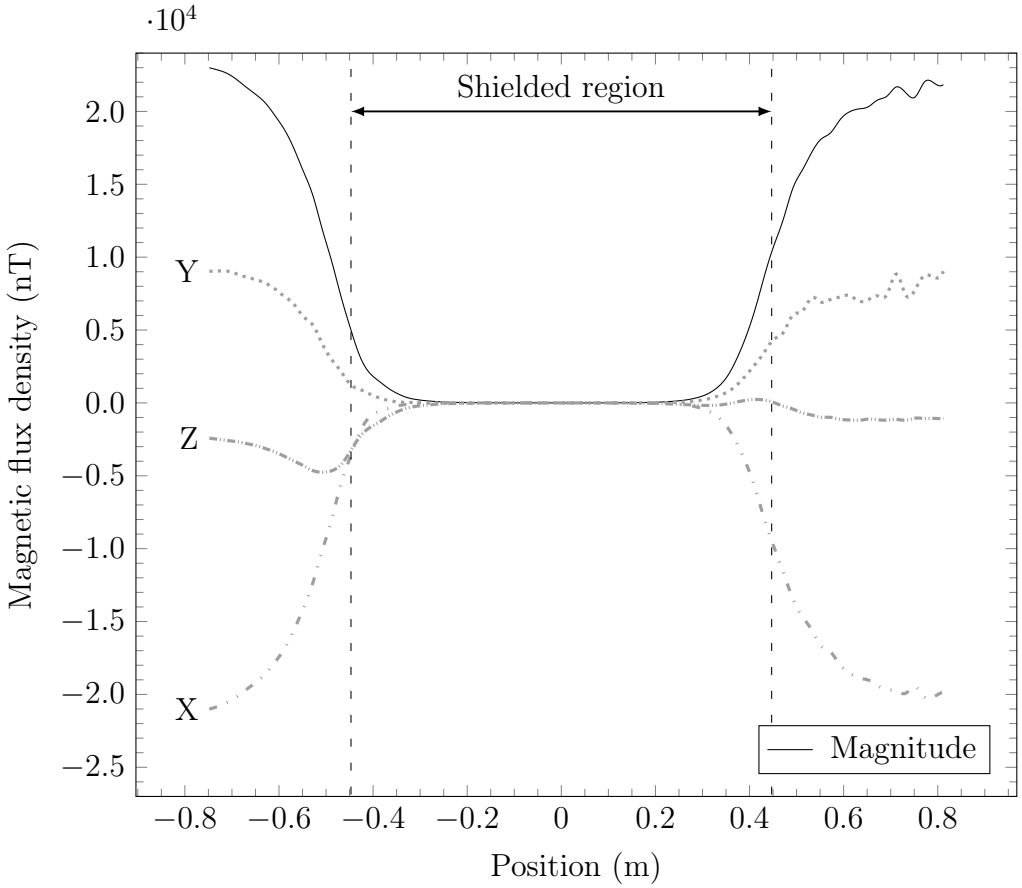


Figure 6.4: Magnetic flux density as a function of position along the main axis of a two-layer magnetic shield. The 0 m position corresponds to the midpoint of the main axis of the shield. The area marked "Shielded region" corresponds to measurements taken inside the magnetic shield.

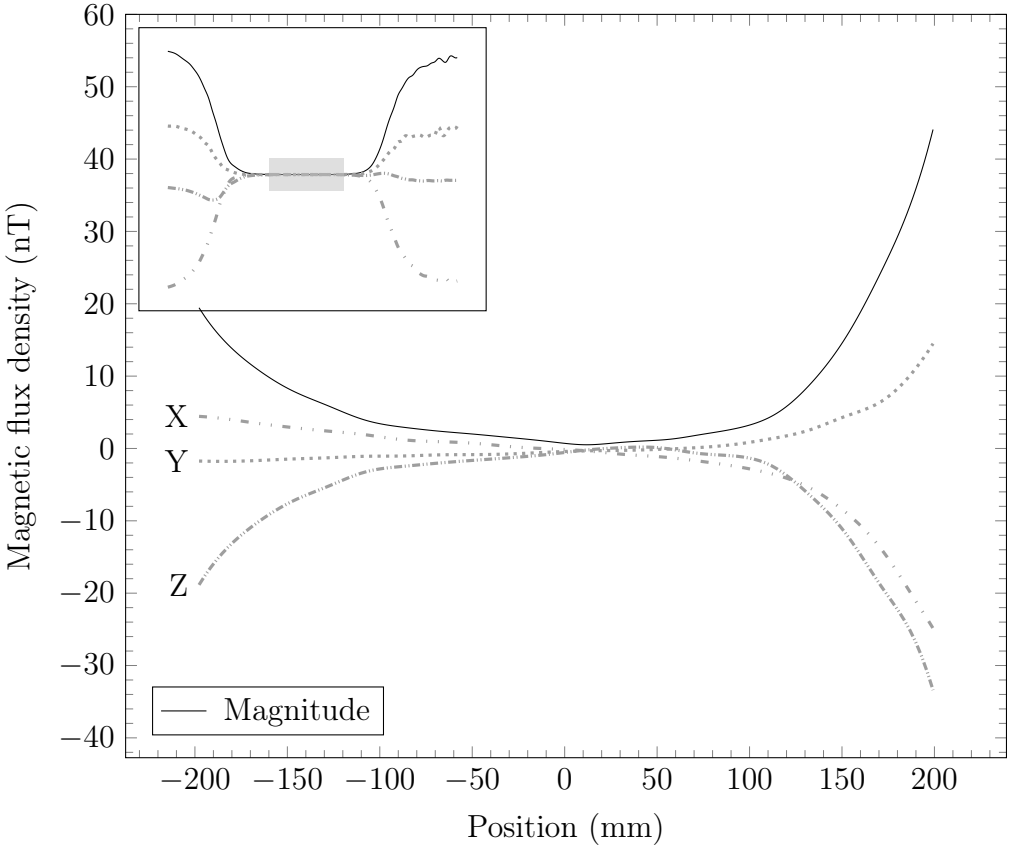


Figure 6.5: A small section of Figure 6.4, centred around the midpoint of the main axis of the magnetic shield used in the investigation. The grey rectangle in the inset graph indicates where the enlarged section was taken from Figure 6.4.

As mentioned, a second three-component fluxgate magnetometer was positioned perpendicular to the left-hand opening of the shield at a distance of ∼300 mm. This sensor served to monitor the ambient magnetic field near the shield, and it was aligned such that the Z-component was parallel to the main axis of the magnetic shield, the Y-component parallel to the minor axis of the magnetic shield, and the X-component perpendicular to the floor. The data were tabulated in Table 6.1.

Table 6.1: A table of the minimum, maximum, and average values of the components of the ambient magnetic field, near the magnetic shield, when the residual field was measured. The X-component measured the vertical component, and the Y and Z components constituted the horizontal components of the geomagnetic field. The measurement duration was 1.48 h, and the effective sampling rate was 100 Hz.

Component	Minimum (nT)	Average (nT)	Maximum (nT)
X	−20 598	−20 485	−20 345
Y	9673.4	9761.7	9863.2
Z	2014.9	2142.9	2168.4

6.4 Response to a Magnetic Dipole

A magnetic dipole on a 27 mm length of cassette tape was moved through the measurement system in 20 mm increments with an 87 mm vertical distance between the fluxgate magnetometer and the cassette tape. An aim of the experiment was to determine the distance at which the fluxgate magnetometer detected the dipole.

The ambient field in the chamber, which was a constant offset, was measured and removed to make it easier to identify the point where the sensor started to respond to the dipole. This was achieved by measuring the residual field in the chamber without the dipole and subtracting this value, in post-processing, from measurements taken with the dipole present. The time between these two sets of measurements was kept short to minimise field variations.

At each measurement point, multiple recordings of the magnetic field with and without the dipole were taken and averaged in post-processing. The sampling rate was 2 kHz, with 250 samples per measurement, resulting in an effective rate of 8 Hz. The resulting points were plotted, and lines of best fit were added to Figures 6.6, 6.7, and 6.8, which corresponded to the X, Y, and Z components of the magnetic flux density, respectively.

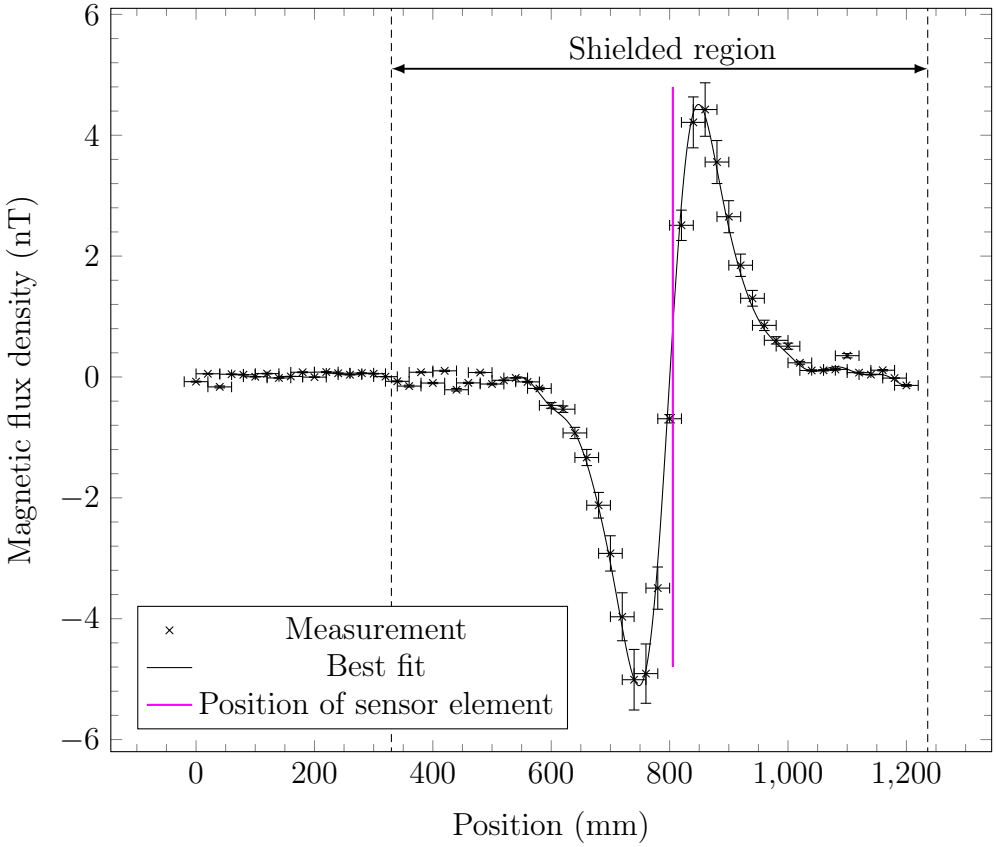


Figure 6.6: X component of the response of a fluxgate magnetometer to a magnetic dipole. The line of best fit, for positions between 540–1200 mm, was an eight-term Fourier model ($R^2 = 0.9984$, RMSE = 0.0886). The effective sampling rate was 8 Hz. The 'shielded region' annotation indicates the extent of the area enclosed by the magnetic shield.

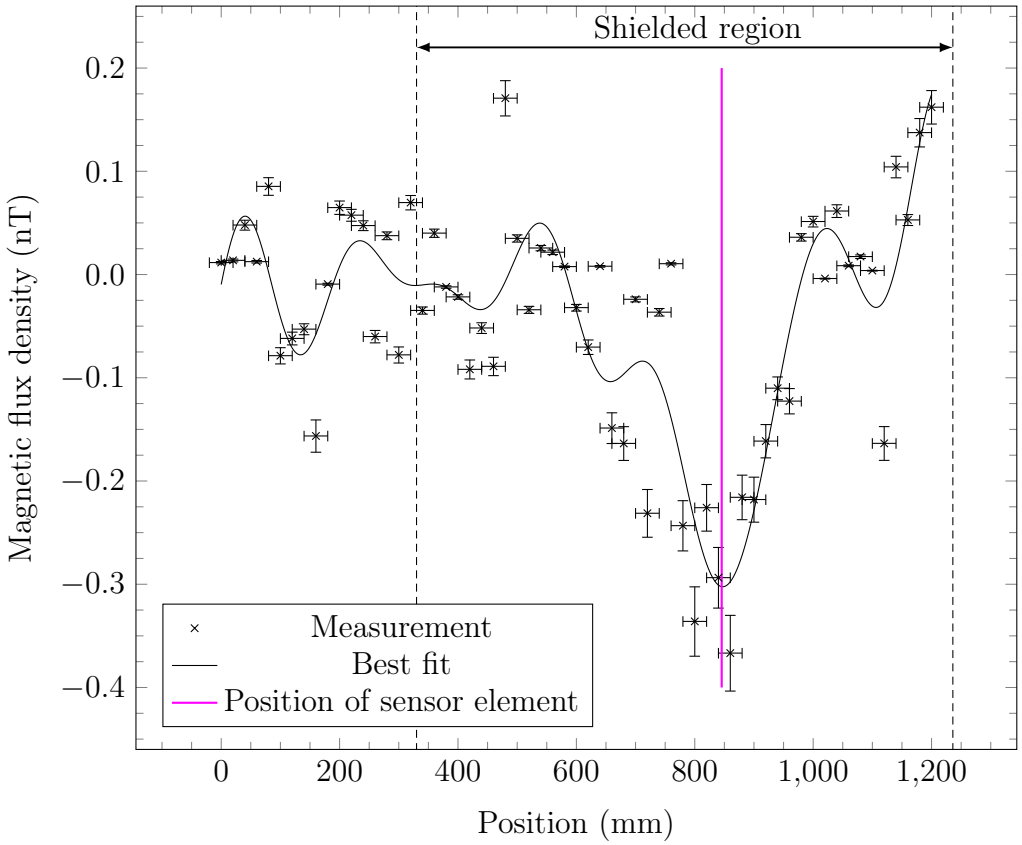


Figure 6.7: Y component of the response of a fluxgate magnetometer to a magnetic dipole. The line of best fit was an eight-term Fourier model ($R^2 = 0.7203$, RMSE = 0.0727). The effective sampling rate was 8 Hz. The 'shielded region' annotation indicates the extent of the area enclosed by the magnetic shield.

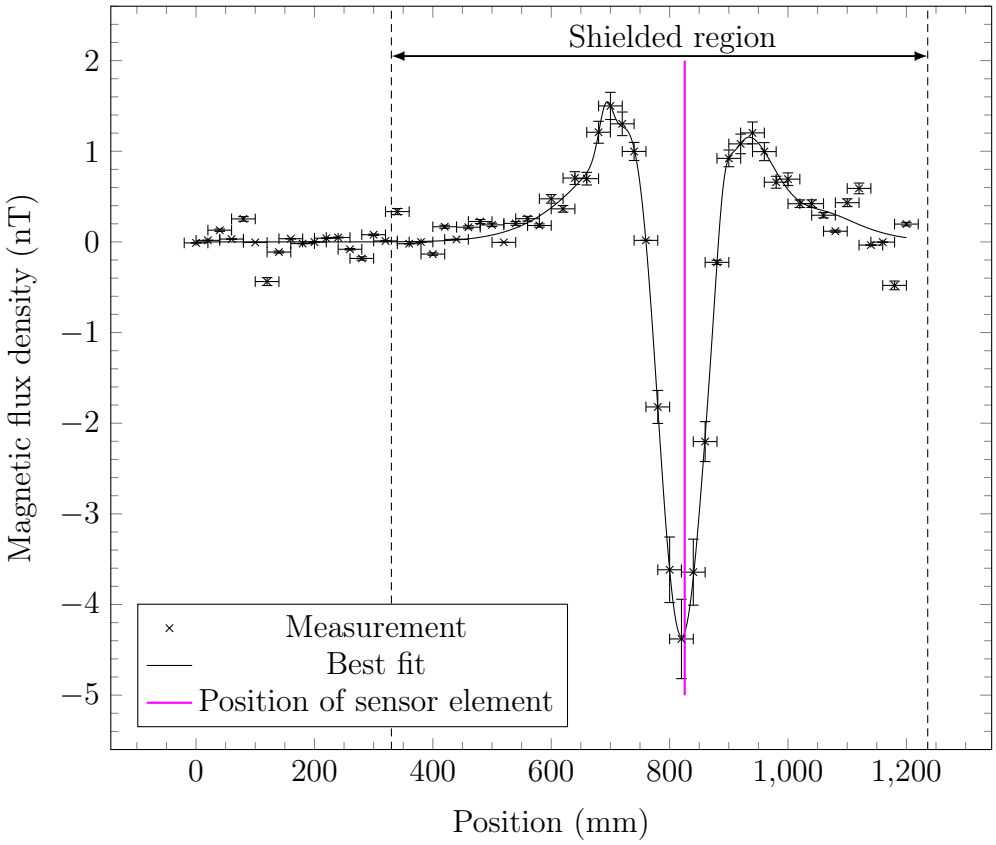


Figure 6.8: Z component of the response of a fluxgate magnetometer to a magnetic dipole. The line of best fit was a six-term Gaussian model ($R^2 = 0.9818$, RMSE = 0.1708). The effective sampling rate was 8 Hz. The 'shielded region' annotation indicates the extent of the area enclosed by the magnetic shield.

Figures 6.6 and 6.8 exhibit the typical response of a fluxgate magnetometer to a magnetic dipole yet the response of the Y-component (Figure 6.7) is not zero, as was expected. Since the cassette tape was magnetised along the length of the tape and not across the thin width of the tape, this component of the magnetisation should be zero. This non-zero response results from a combination of two main factors: the cassette tape was not perfectly aligned with respect to the Z-component of the fluxgate magnetometer (see Figure 6.1a) and the magnetisation of cassette tape was not perfectly parallel to the long axis of the cassette tape. A detailed analysis, including a discussion on the shape of the responses, is provided in Section 7.3.

6.5 Synthetic Reversals

Heye and Meyer explained that a drill core could be thought of as a collection of infinitely thin slices with each slice having a different magnetisation [20]. As fluxgate magnetometers average the magnetic field across the length of the sensing element, an experiment was performed to determine the minimum thickness of three consecutive synthetic drill core slices, where the middle slice is oppositely magnetized, to still detect a directional change in the field [20]. An illustration of the configuration of synthetic standards used in the experiment is displayed in Figure 6.9 below. Samples A and C were kept at a fixed length of 90 mm, and the length of sample B was either 50 mm, 30 mm or 20 mm.

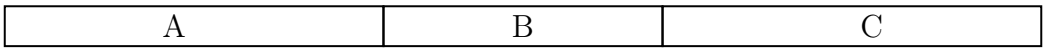


Figure 6.9: A diagram of three synthetic drill cores used to evaluate the ability of the proposed measurement system to resolve changes in the direction of a magnetic field. Samples A and C had magnetisations oriented in the same direction, while sample B had a magnetisation in the opposite direction.

In contrast to previous experiments, the results presented from this section onward plot the magnetic flux density as a function of time rather than as a function of position. A key requirement of the measurement system is the rapid detection of the change in the direction of the remanent magnetisation in drill cores. In the absence of an automated method to measure the position of the drill cores as they are passed through the measurement system, the cores must be incrementally moved through the system, with each position recorded using a wooden ruler. This method is time-consuming and susceptible to errors. To facilitate the rapid acquisition of measurements from many drill cores, it is recommended that the approximate start and end positions, or drill core identifiers, be recorded and associated with the measurements. In post-processing of the results, if signals of interest are identified, they can be associated with subsections of drill cores, which may then be reanalysed with the system as a function of position. A complete discussion on this topic is presented in **Chapter 7**.

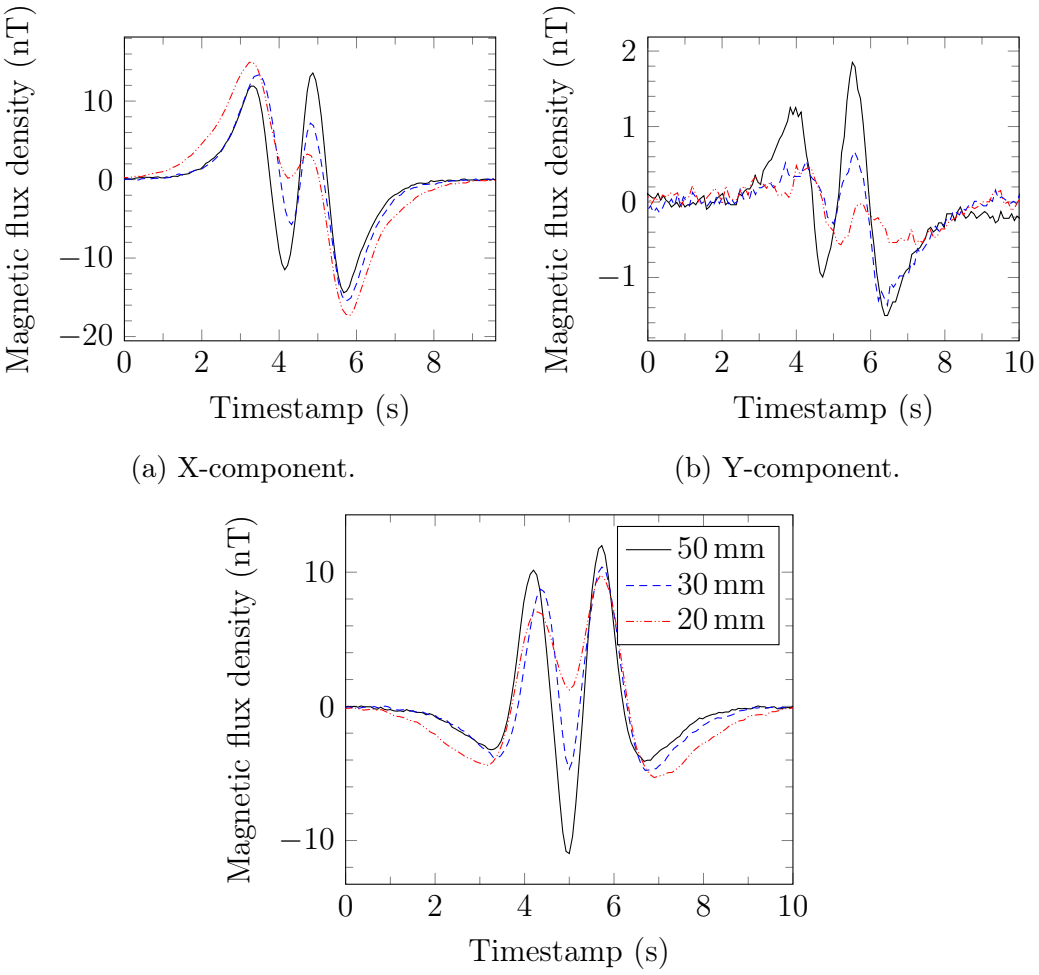
The three sets of responses presented in Figure 6.10 were scaled such that the

points of reversal in the measurements were approximately aligned.

Like the previous experiments, the residual field in the magnetic shield was recorded before the samples were passed through the measurement system. The residual field was subtracted from the measurement results in post-processing, so only the contribution of the magnetic field from the synthetic cores was visible.

The sampling rate was 2 kHz, and 200 averages were taken per recorded measurement. This yielded an effective sampling rate of 10 Hz. The effective sampling rate was chosen to be higher than previous sampling rates to account for the continuous motion of the synthetic cores.

The outputs of each component recorded by the fluxgate magnetometer were plotted in Figure 6.10 below.



(a) X-component.

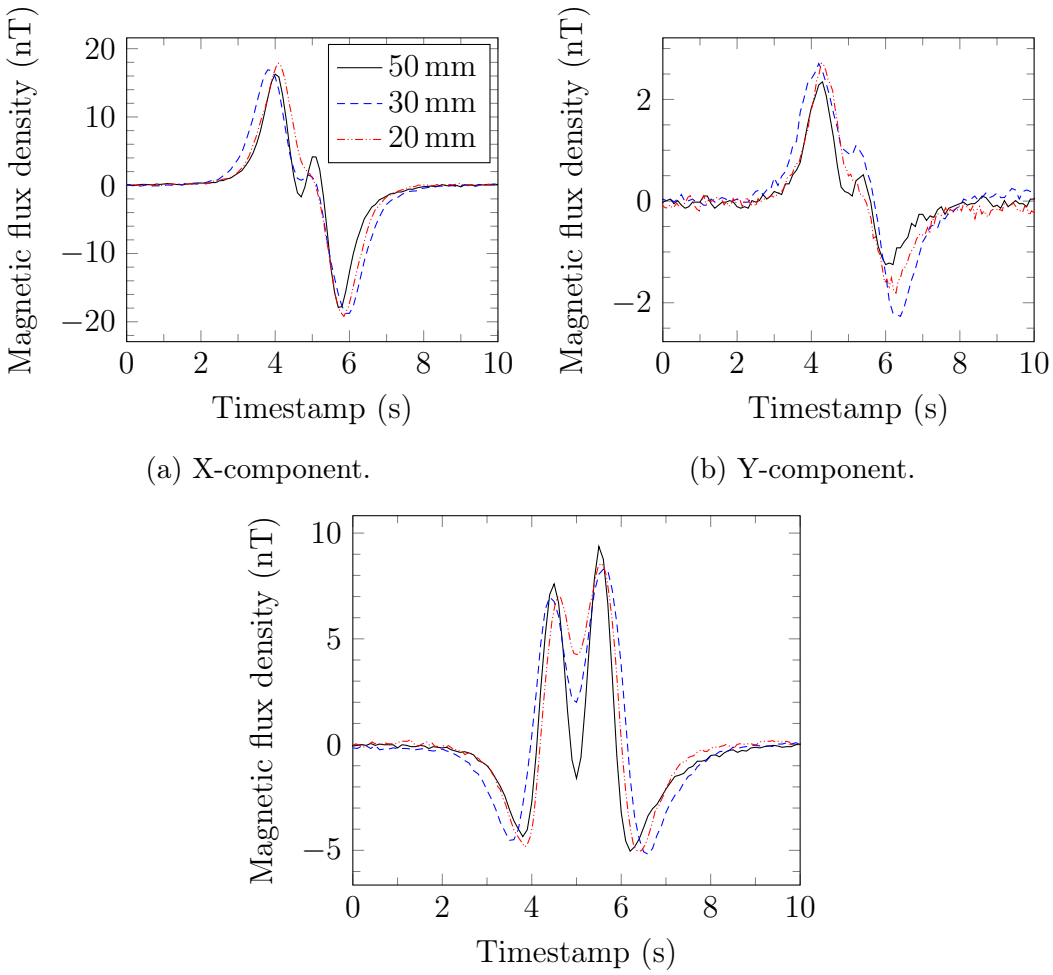
(b) Y-component.

(c) Z-component.

Figure 6.10: Three sets of fluxgate magnetometer outputs were collected using three synthetic drill cores passed under the sensor, with the length of the centre standard varied each run. The effective sampling rate was 10 Hz. The legend in Figure 6.10c applies to Figures 6.10a and 6.10b.

A second experiment was conducted to investigate the response of the fluxgate magnetometer to two sets of synthetic cores with the same polarity, separated by gaps of varying lengths. Heye and Meyer highlighted that in certain cases, it may be possible to erroneously interpret the response of the fluxgate to a gap between consecutive drill cores as a magnetic field reversal [20]. The same measurement and data processing procedure discussed above was used. The results were plotted

in Figure 6.11.



(a) X-component.

(b) Y-component.

(c) Z-component.

Figure 6.11: Three sets of fluxgate magnetometer outputs were collected using two synthetic drill cores, separated by a gap, passed under the sensor, with the length of the gap varied each run. The effective sampling rate was 10 Hz. The legend in Figure 6.11a applies to Figures 6.11b and 6.11c.

Figure 6.10 shows that the ability of a fluxgate magnetometer to resolve a reversal in the direction of the remanent magnetisation of the synthetic drill cores diminishes as the length of the reversed layer decreases. This indicates that the fluxgate magnetometer has a threshold thickness, for the reversed/normal layer, below which it cannot discern a reversal.

Similarly, the results in Figure 6.11 show that a fluxgate magnetometer cannot detect the presence of an air gap between two consecutive drill cores below a threshold distance. This is an important consideration as the presence of an air gap can possibly introduce artefacts that appear to be remanent magnetisation measurements consistent with a geomagnetic field reversal.

The above findings are discussed further in Section 7.4.

6.6 Weakly Magnetised Drill Cores from the BIC

Table 4.1 lists the weakest NRM recorded by a drill core sample in the Main Zone of the Eastern Lobe [5]. Access to drill cores from the Main Zone with similar characteristics would prove a definitive means of testing the lower bound of the requirement for the measurement system to detect magnetic fields on the order of a few nanoteslas. Conveniently, 1.06 m of Main Zone drill cores from an older borehole, location unknown, were obtained. These drill cores had been subjected to study by undergraduate students, and it was not known whether the drill cores were handled correctly to avoid the acquisition of overprints.

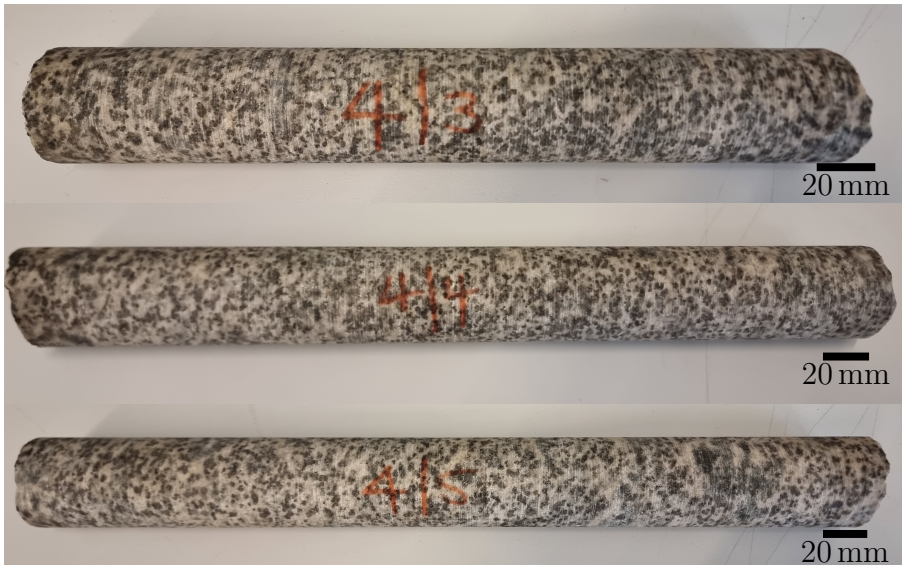


Figure 6.12: Images of the Main Zone drill cores, from the BIC, with weak remanent magnetisation. Drill cores with identifiers 4/3, 4/4, and 4/5 are presented in the top, centre, and bottom of the image, respectively. All cores had a diameter of 40 mm and cores 4/3, 4/4, and 4/5 had lengths of 290 mm, 380 mm, and 390 mm, respectively.

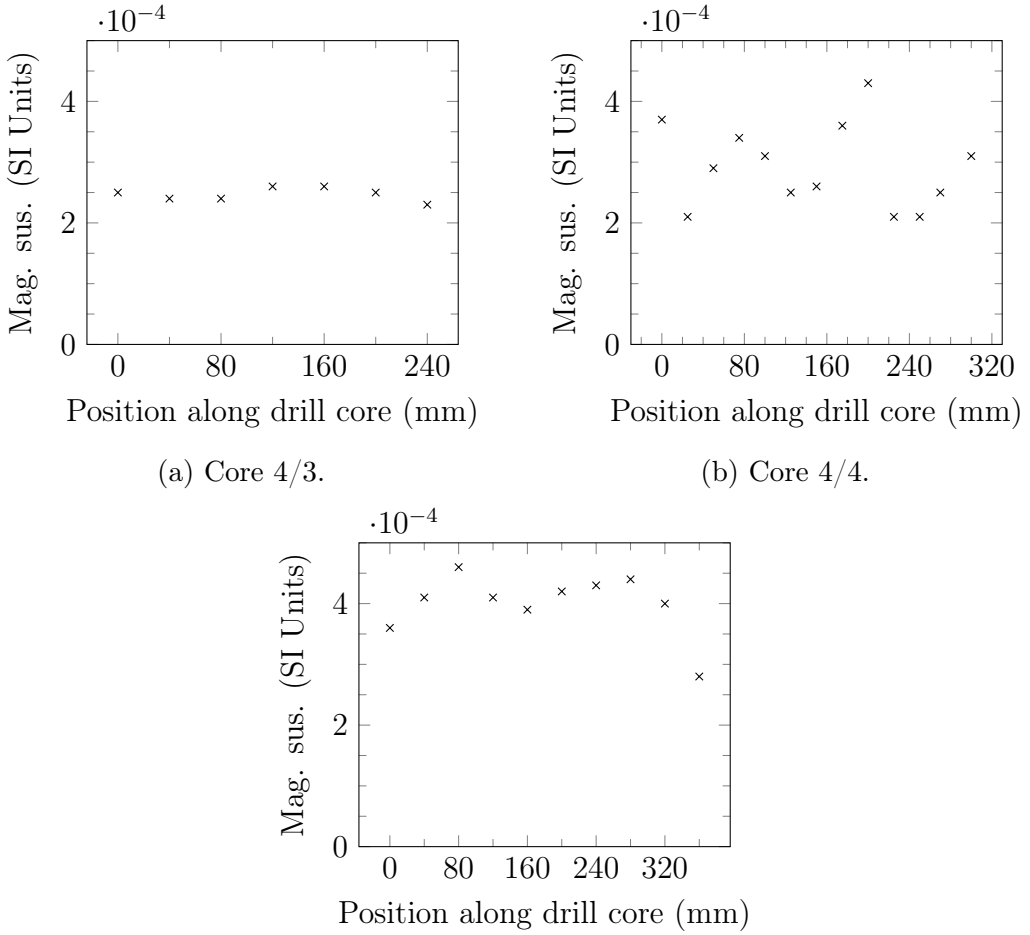
Magnetic susceptibility was used to assess the presence of minerals in the drill cores that could either become magnetised in response to an external magnetic field or serve as carriers of remanent magnetisation. If the magnetic susceptibility was low, it suggested that the rock contained few minerals capable of acquiring either temporary (induced) or permanent (remanent) magnetisation. Magnetite is a well-established carrier of remanence, and in some igneous rocks and sedimentary sequences, magnetic susceptibility has been used as a proxy for magnetite content [10]. This observation is considered in more detail in **Chapter 7**.

Measurements of the magnetic susceptibility of the three drill cores were recorded and plotted in Figure 6.13. The magnetic susceptibility was measured with the GDD MPP instrument. Measurements were taken by first allowing the device to "warmup" for an hour, as per manufacturer recommendations, and then zeroing the device so that when left in open-air, the magnetic susceptibility was recorded as zero. The device was then placed on a drill core and a measurement taken (the

device did not have to be removed from the drill core, and left in the air, for a measurement to be taken). The magnetic susceptibility of all the drill cores was on the order of 10^{-4} SI Units.

Initially, the fluxgate was positioned 87 mm vertically above the drill cores, and the sampling rate was set to 2 kHz with 100 averages per measurement (effective sampling rate of 20 Hz). The results from drill core 4/3, Figure 6.14, indicated that while a response might be contained in the signal, the resolution was poor. The fluxgate magnetometer was repositioned so that it was approximately 10 mm above the drill core to improve the strength of the measured remanent magnetic field. The number of averages was increased to 200 so that the effective sampling rate was reduced to 10 Hz. The results were plotted in Figures 6.15, 6.16, and 6.17 for drill cores labelled 4/3, 4/4, and 4/5, respectively.

The residual field in the chamber was not removed from the measurements because, in the proposed measurement system, measuring the residual field without any drill cores in the chamber would be too time-consuming when analysing many drill cores. This is in keeping with a key requirement of the proposed system: rapid operation. Instead, the ability to resolve the magnetic fields of weakly magnetised cores was evaluated, with the residual field acting as the limiting factor for the minimum detectable field from the drill cores.



(a) Core 4/3.

(b) Core 4/4.

(c) Core 4/5.

Figure 6.13: Magnetic susceptibility measurements, as a function of position along drill core 4/3, 4/4, and 4/5, recorded with the GDD MPP instrument.

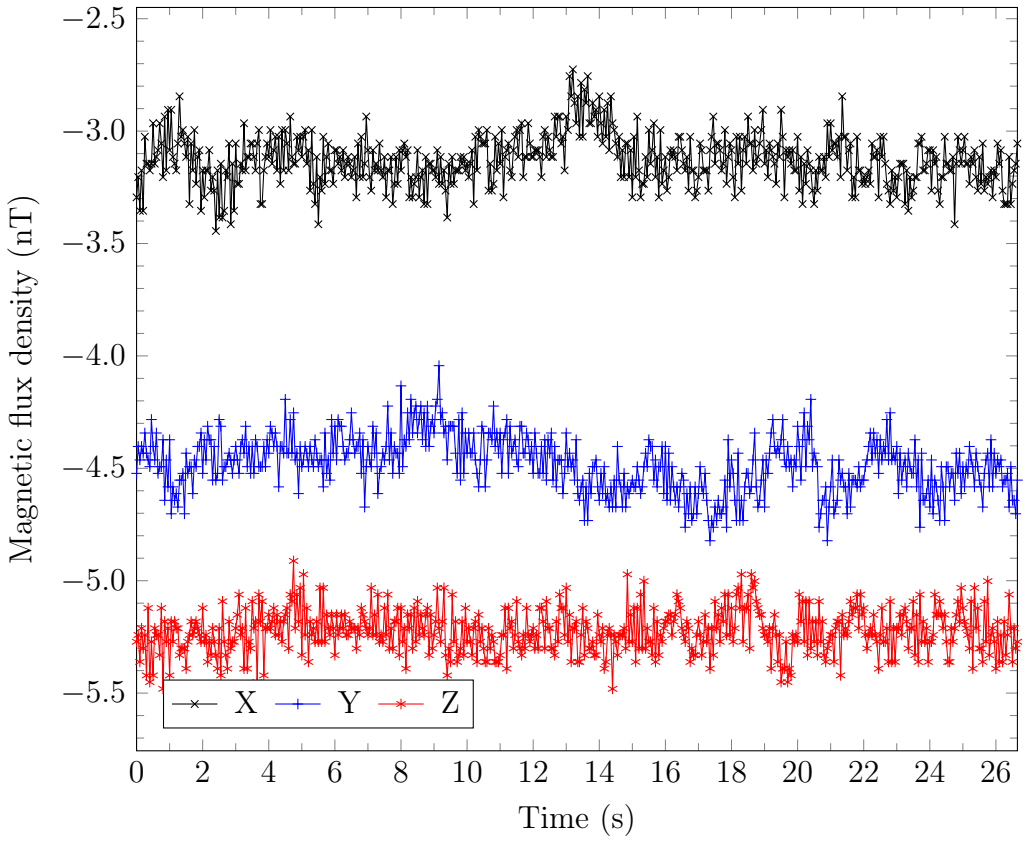


Figure 6.14: A plot of the three components of the magnetic flux density recorded for drill core with ID 4/3, from the Main Zone of the BIC, that contained little magnetic minerals, passed through the measurement system used in the investigation. The effective sampling rate was 20 Hz.

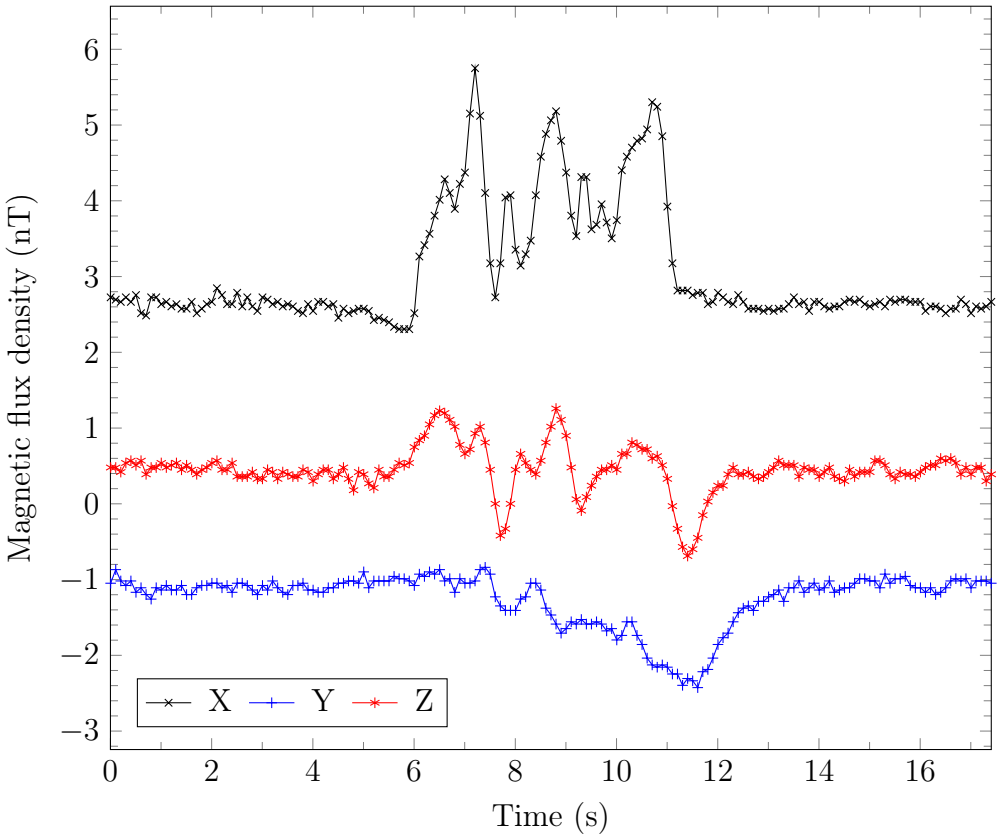


Figure 6.15: A plot of the three components of the magnetic flux density for the drill core with ID 4/3, from the Main Zone of the BIC, that contained little magnetic minerals, passed through the measurement system used in the investigation. The effective sampling rate was 10 Hz.

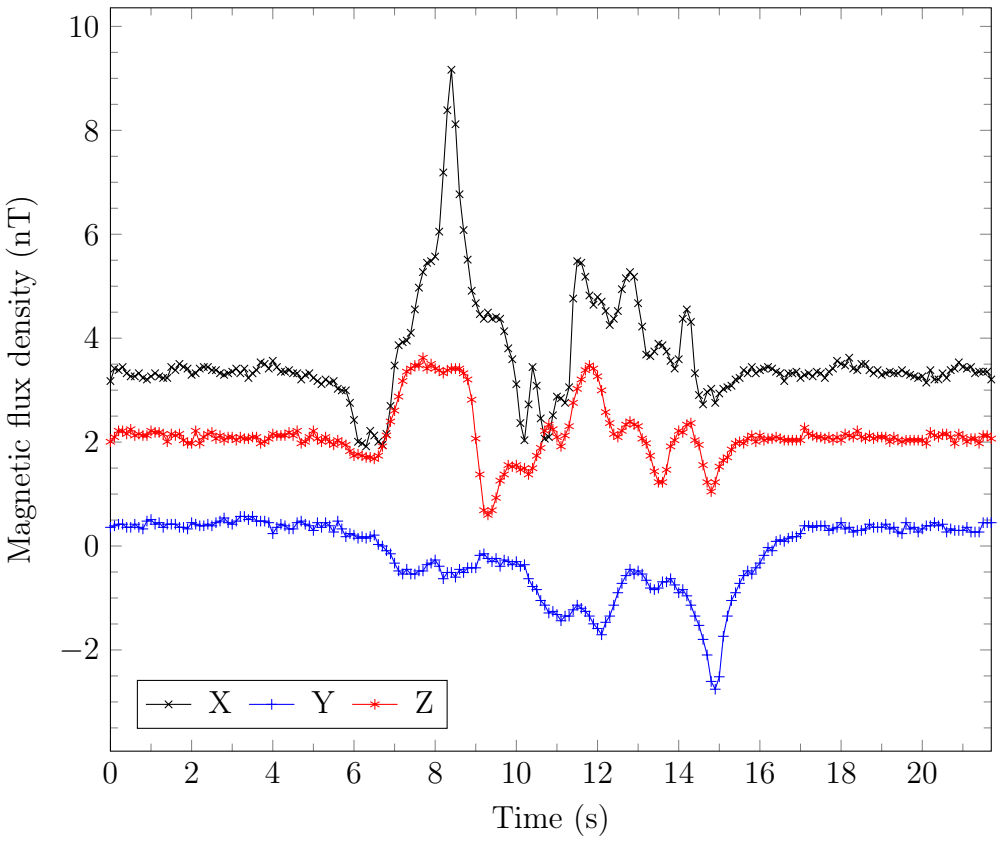


Figure 6.16: A plot of the three components of the magnetic flux density for the drill core with ID 4/4, from the Main Zone of the BIC, that contained little magnetic minerals, passed through the measurement system used in the investigation. The effective sampling rate was 10 Hz.

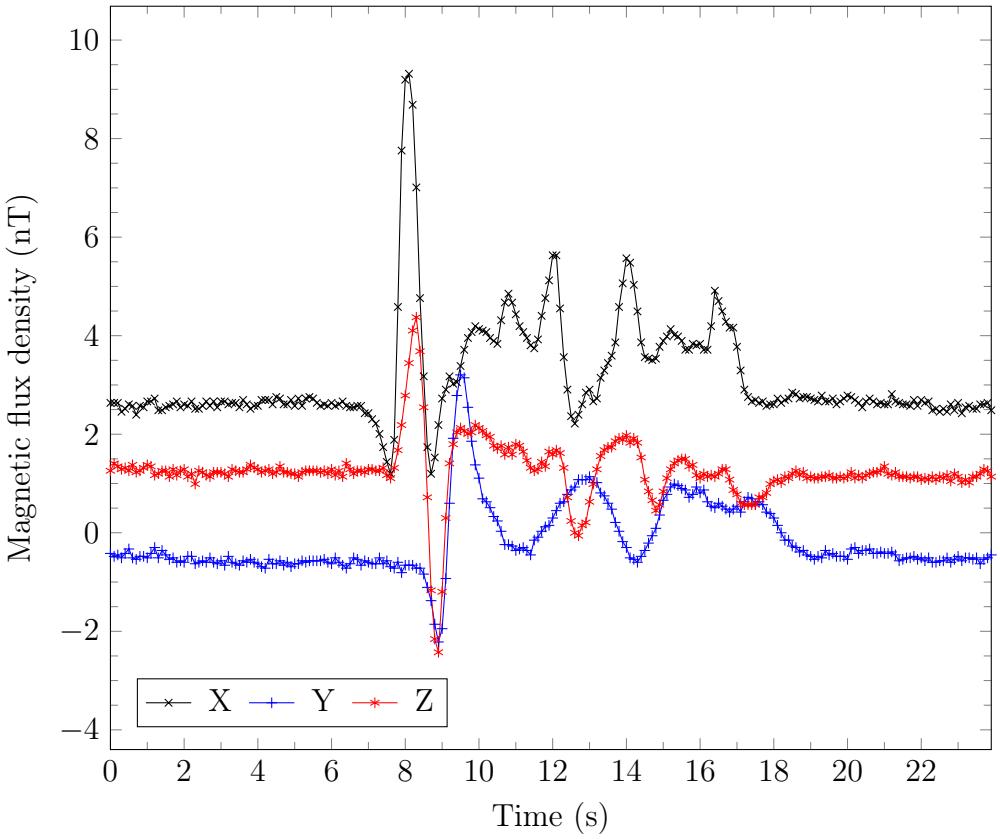


Figure 6.17: A plot of the three components of the magnetic flux density for the drill core with ID 4/5, from the Main Zone of the BIC, that contained little magnetic minerals, passed through the measurement system used in the investigation. The effective sampling rate was 10 Hz.

6.7 Strongly Magnetised Drill Core from the BIC

A previous study obtained a drill core sample (Figure 6.18) near the Atok mine, located in the northern region of the Eastern Lobe of the BIC [56]. The sample was sourced from the Critical Zone within the Rustenburg Layered Suite (Figure 1.1) [56]. This drill core was subjected to neutron tomography at the Pelindaba nuclear research reactor, and it was not known whether this process and subsequent handling of the core altered any primary magnetisation or possibly introduced secondary magnetisation.



Figure 6.18: An image of the strongly magnetised drill core from the Critical Zone in the Eastern Lobe of the BIC. The "A" side of the core is facing the camera. Ledwaba reported the sample had a length of 100 mm and a diameter of 30 mm [56].

A series of measurements in four different orientations were taken along the length of the core as only five measurements could be collected for each profile. Multiple profiles were used to collect more data. For example, side C of the drill core, in Figure 6.18, was a 90° rotation about the main axis from side A of the core. The results were plotted in Figure 6.19 below. The magnetic susceptibility was on the order of 10^{-3} SI Units for the drill core.

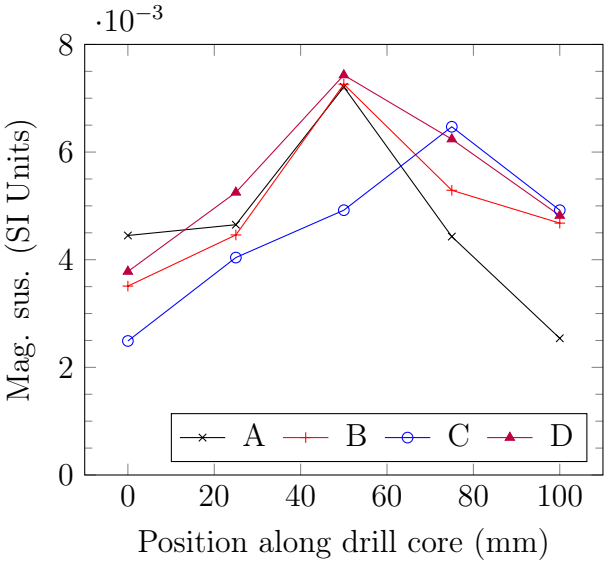


Figure 6.19: Magnetic susceptibility measurements as a function of position along the drill core recovered near the Atok mine, recorded by the GDD MPP instrument. The letters in the legend correspond to four different profiles taken along the length of the drill core. Each profile was a 90° rotation about the main axis from the other.

Using the same setup as described previously, the fluxgate magnetometer was positioned as close to the drill core as possible without making contact. The sampling rate was 600 Hz, and no averaging was used. This was not intentional and was a configuration error on the TDX. The results are still of value as they demonstrate how the noise recorded by the fluxgate magnetometer changes with the number of averages taken per measurement. The results were plotted in Figure 6.20 below.

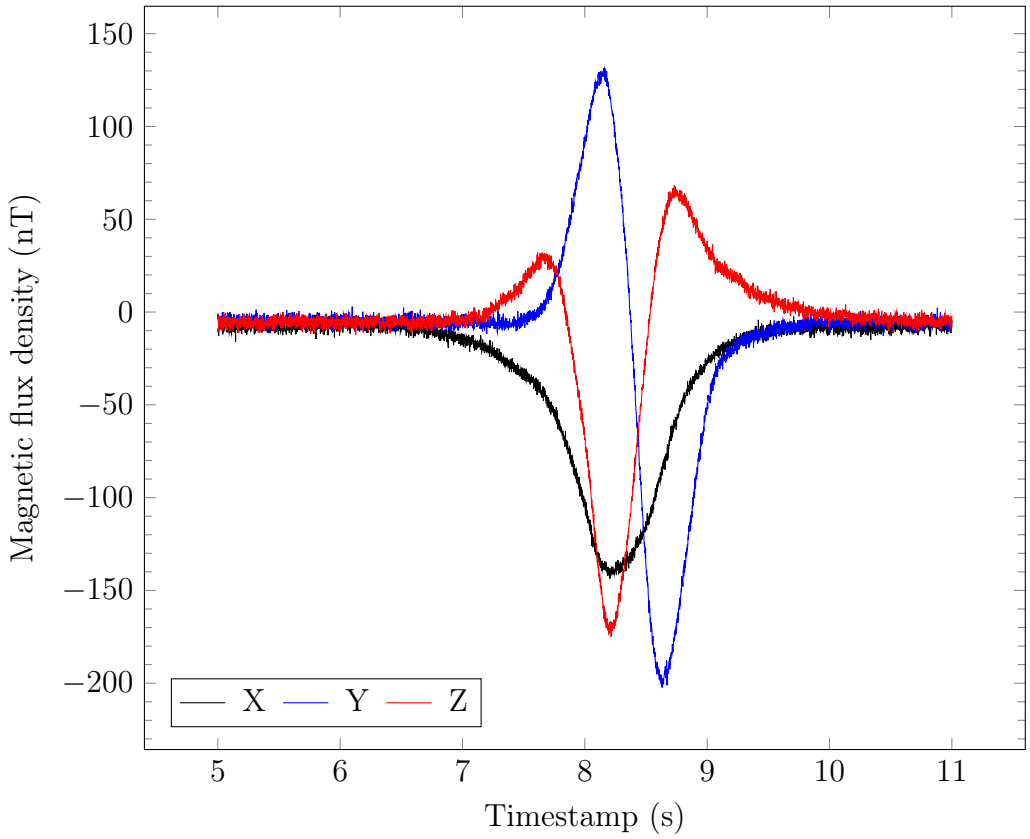


Figure 6.20: A plot of the three components of the magnetic flux density for a drill core, from the Critical Zone in the Eastern Lobe of the BIC. The effective sampling rate was 600 Hz.

As expected, Figures 6.14 and 6.15 depict the inverse relationship between the magnitude of the magnetic flux density and the distance between the source of the magnetisation and point of measurement. Figures 6.15 to 6.17 exhibit complex magnetic fields measured along the drill cores as they were passed through the proposed measurement system. In contrast, Figure 6.20 presents a drill core with a simple magnetic field made up of a single dominant magnetic dipole. A detailed analysis of these findings is presented in Section 7.5.

The next chapter reconciles the FEA results with the experimental measurements and provides a discussion on the data collected from the measurement of the synthetic and real drill cores in the proposed measurement system.

Chapter 7

Tracing the Past: Evaluating a Magnetic Reversal Measurement System

This chapter discusses the application of the FEA to the evaluation of magnetic shield performance and the validation of the FEA results. Data from both synthetic and real drill cores, recovered from the BIC, were analysed to assess the response of the system to real and synthetic inputs. The chapter concludes by identifying the limitations of the system and suggestions for improvements that should be made to facilitate deployment at a drill site or drill core storage facility.

Previous chapters present the context and design requirements for a measurement system intended to investigate the possibility of rapidly detecting reversals in the magnetic field of the Earth, as recorded in drill cores. Results from both simulations and experiments are provided to understand the nature of the residual field in the magnetic shield and any possible interactions with the drill cores and fluxgate magnetometer. This chapter focuses on reconciling the experimental results with the simulations and details how these findings have been employed

to achieve the optimal placement of the fluxgate magnetometer and drill cores within the magnetic shield. With this information, the outcomes from experimental measurements of synthetic drill cores, as well as short sections of real drill cores, are discussed. Through this process, it is apparent that the proposed system is capable of resolving changes in the direction of the permanent magnetic field recorded in synthetic samples. A brief discussion also examines the results obtained from measurements of short sections of drill cores from the BIC, before concluding with limitations and recommendations for improvement of the measurement system.

The FEA of the magnetic shield is the starting point for the evaluation of the measurement system as it provides a way to characterise the nature of the residual field inside the magnetic shield. The residual field is identified as the limiting factor in the ability of the measurement system to resolve changes in the direction of the magnetic flux density associated with weakly magnetised samples.

7.1 Finite Element Analysis Validation

The FEA, in **Chapter 5**, was used to determine the optimal placement of components in the proposed measurement system, which was designed to address the investigative question.

The method of FEA is utilised as manually performing measurements of the flux density inside the three-dimensional cavity of the shield is impractical and error-prone. The use of the FEA presents a way to analyse the nature of the residual field with high-fidelity results while bypassing the time-consuming and error-prone nature of experimental measurements.

Before using the FEA to determine the optimal placement of a fluxgate magnetometer and the drill cores, it is considered best practice to validate the results [57]. Indeed, several disasters have been caused by ill-formed design choices based on incorrect results from FEA codes - see the Sleipner A-1 offshore platform accident in Further Reading [57]. In the context of FEA, validation refers to a comparison of the FEA results with data gathered from experiments [57]. It is not always practical or financially feasible to conduct experiments so closed-form solutions

that, often poorly, approximate the complex behaviour modelled by the FEA are used [57].

Four FEAs were performed where the number of elements used to discretise the magnetic shield were varied between 5–95 M. This was done to observe the effect that the number of elements had on the results. A study of this type, known as a convergence study, is useful to check that the same *relative* characteristics are being observed across a range of different meshes. This is useful to try and spot issues with the mesh generation.

Figure 5.5 shows that the general behaviour of the magnetic shield is the same for all four analyses, and Figure 5.6 shows that all four analyses tended toward the same neighbourhood of values for the magnitude of the minimum flux density. But the analysis performed with the 5 M element input mesh shows that the magnetic field along the main axis of the shield is uniform, while the other three analyses indicate varying degrees of inhomogeneity. Although the analyses all exhibited the same general large-scale behaviour, the correctness of the analyses can only be validated through a comparison with experimental measurements.

The results from the FEA, with the 95 M element input mesh, were compared against experimental measurements in Figure 7.1 to validate the analysis around the region immediately surrounding the main axis of the shield.

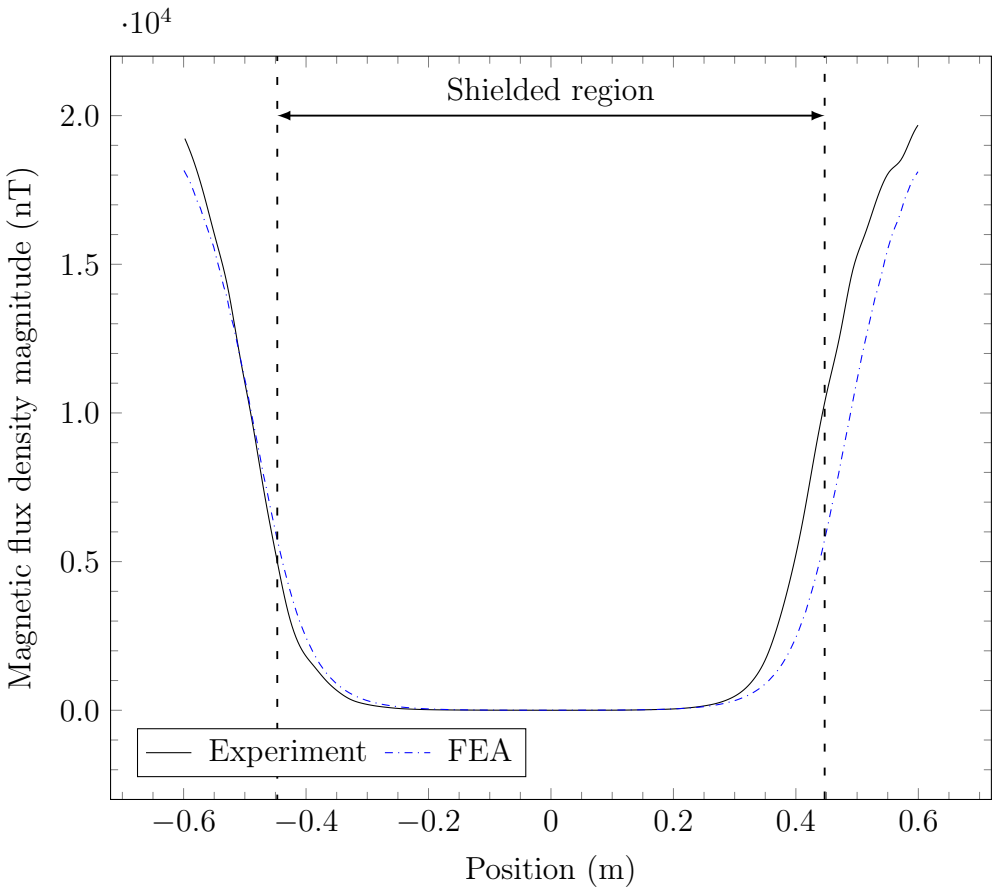


Figure 7.1: A line plot comparing the FEA and experimental results for the magnetic flux density along the main axis of the magnetic shield used in the investigation. The centre of the shield, along the main axis, is found at the 0 m position and the space enclosed by the shield is indicated on the plot as the "shielded region".

The disagreement between the two sets of results, from 0.3 m to 0.6 m, is reconciled by noting that the boundary conditions of the FEA imposed a constant and uniform ambient magnetic flux density while the ambient magnetic field in the laboratory was non-uniform and had gradients. It was observed that the magnitude of the ambient magnetic flux density changed by 2400 nT over the 1.5 m length of the desk where the magnetic shield was positioned during the experiments. The presence of this gradient might have arisen from the sheet metal embedded in the top of the laboratory wall, near the non-magnetic area, where the experiments were conducted.

Figure 7.2 presented the same comparison given in Figure 7.1 but for a smaller section centred around the midpoint of the main axis of the magnetic shield.

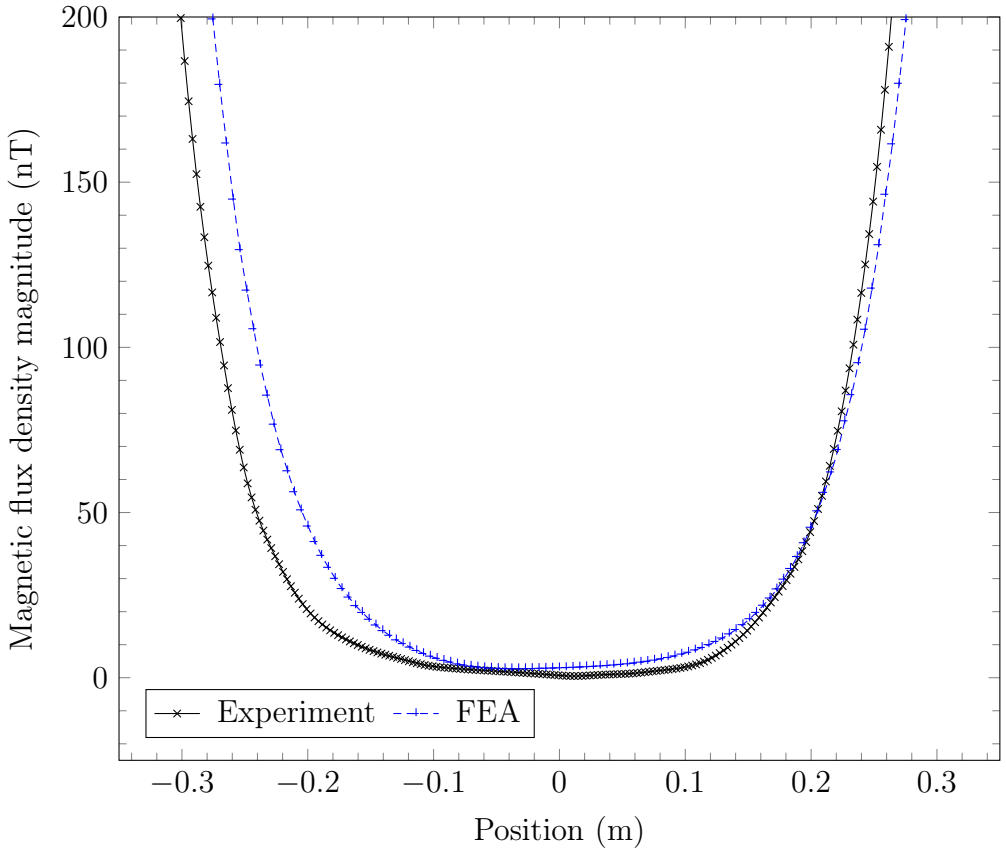


Figure 7.2: A small section of Figure 7.1 focuses on the midpoint of the main axis of the magnetic shield, comparing the FEA and experimental results for the magnetic flux density.

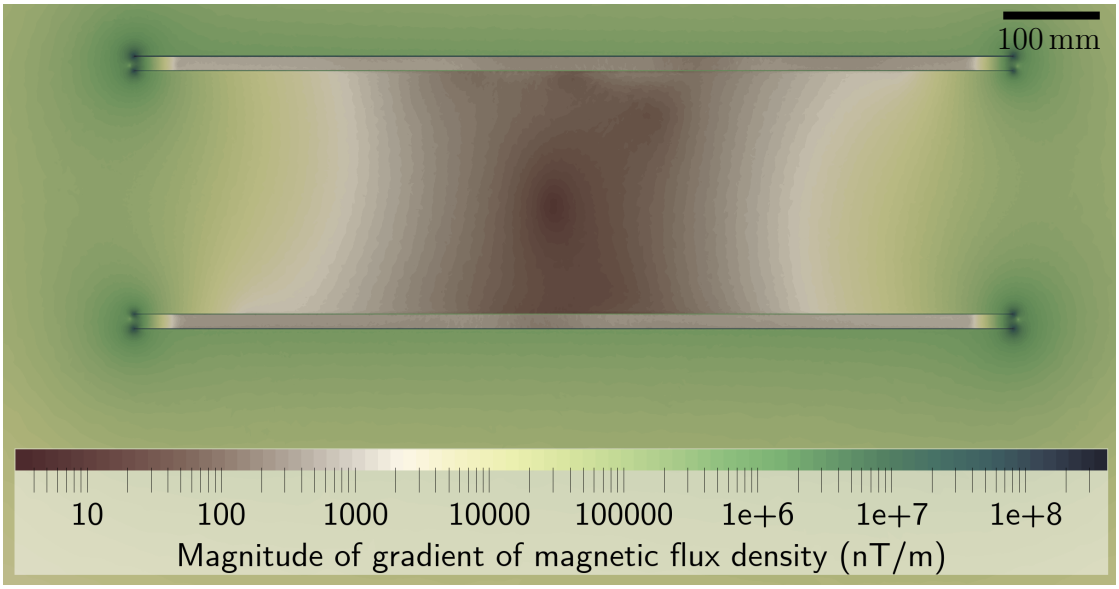
The source of the discrepancy between the results is the same as discussed above. Aside from this discrepancy, the FEA results demonstrate that the simulation accurately captures the overall behaviour of the internal region immediately around the main axis of the magnetic shield. This also confirms that the non-linear BH material used in the FEA to represent the ASTM A754 Alloy 4 approximates the properties of the shield used in the investigation.

An interesting observation has to do with the construction of the magnetic shield. The HPA metal is not one sheet rolled into a cylinder. Rather, the HPA is

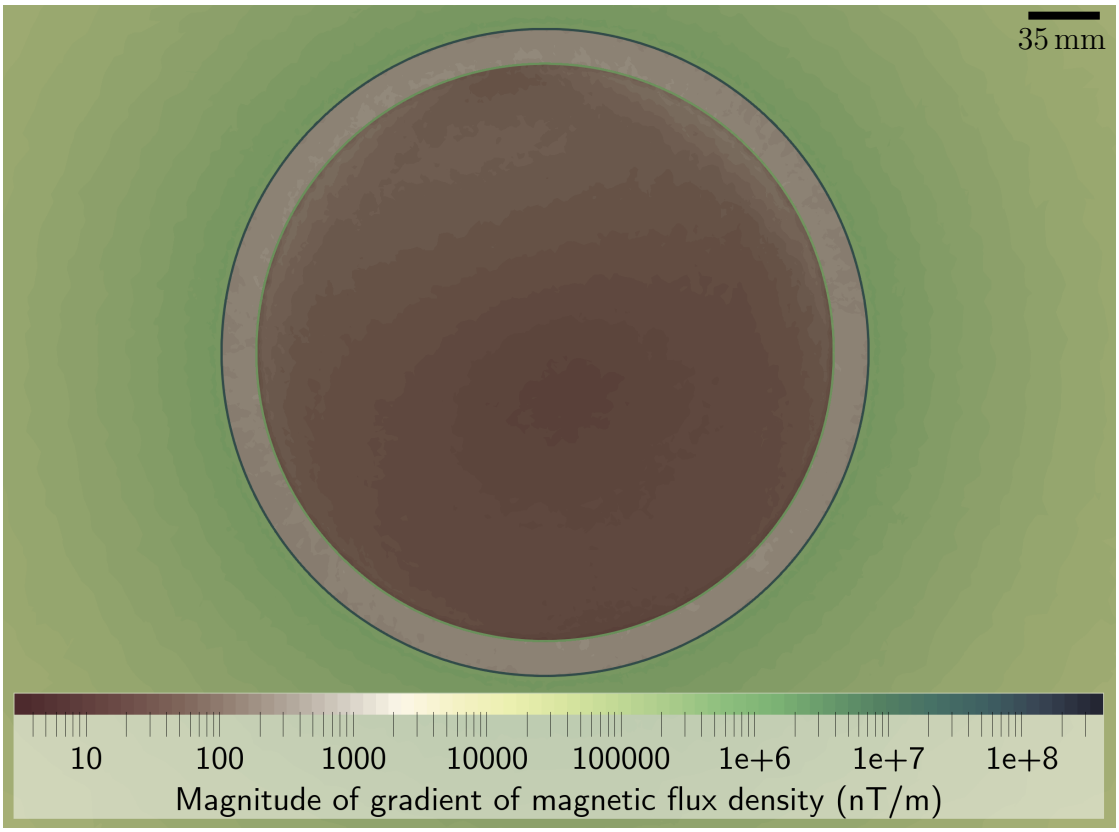
welded together to create the desired length and radius of the cylinder. The FEA assumed the shield material was manufactured into perfect cylinders to simplify the generation of the input mesh. Remarkably, the experimental results show no fringing along the main axis of the shield. This suggests that the welding and treatment processes applied to the HPA were effective or that any fringing at the weld joints is undetectable at the centre of the shield [58].

Figure 5.4 implies the existence of gradients within an hourglass-shaped region centred on the midpoint of the main axis of the shield. Close inspection of this region, in Figure 5.4a and the plot of the FEA with the 95 M element input mesh in Figure 5.6, shows that the hourglass is tilted. This is not an expected result considering that the ambient geomagnetic field, used in the FEA, is uniform. Indeed, the tilted shape of the experimental results in Figure 7.2 is expected seeing as the ambient geomagnetic field is not uniform. However, the origin of the tilt of the hourglass, for the FEA results, is non-physical in nature and has to do with poorly formed mesh elements, as discussed in Section 5.2.

In post-processing, the simulation results were used to numerically compute the Frobenius norm of the second-order gradient tensor of the magnetic flux density ($||\nabla \boldsymbol{B}||_F$) with the results plotted in Figure 7.3 below.



(a) Slice along main axis.



(b) Slice along minor, or radial, axis that intersects the midpoint of the main axis.

Figure 7.3: Main and minor axis slices of the Frobenius norm of the gradient tensor of the magnetic flux density ($||\nabla \boldsymbol{B}||_F$), coloured in 85 bins, inside a two-layer cylindrical magnetic shield exposed to an ambient geomagnetic field.

The variations observed with the movement of a fluxgate magnetometer, inside the magnetic shield, around the midpoint of the main axis suggest that the variation in the field is a few nanotesla. The gradient results, Figure 7.3a, for the hourglass-shaped region suggest that this observation is correct for points located around the centre of the main axis of the shield. Figure 7.3b suggests that the magnetic flux density along the minor axis of the shield is more uniform. A complete and fair comparison of the gradient results from the FEA would require the experimental measurement of enough points inside the shield to facilitate the computation of the nine elements in the gradient tensor.

With the result from the FEA, which used the 95 M element input mesh, in agreement with experimental measurements, these results can be used to analyse the results from the three other FEAs conducted.

In Figure 5.6, the FEA that used an input mesh with 5 M elements did not capture the inhomogeneity in the residual field due to an insufficient number of elements. This assertion is confirmed by noting that the remaining analyses report varying degrees of inhomogeneity. However, if more compute resources are available, an input mesh with more than 125 M elements should be evaluated to see if the disagreement between the results in Figure 7.2 can be partly reduced. Regardless, Figure 5.5 shows that all the input meshes supplied to the FEA capture the effect of the shield significantly attenuating the ambient magnetic field. If an application requires a rough approximation of the behaviour of the shield, and the slight gradient inside can be treated as negligible, then the 5 M and 36 M input meshes are of significant value as they require less compute time than the other analyses: the analysis that used the 36 M element input mesh required a third of the CPU time used by the analysis done on the 95 M element mesh.

7.2 Measurement System Component Placement

When a drill core, containing minerals with non-zero magnetic susceptibilities, is exposed to an ambient magnetic field, an induced magnetisation is generated in the drill core. This induced magnetisation can dominate the resultant, or net, magnetic field measured near a drill core to such an extent that the remanent magnetisation

is rendered negligible. A magnetic shield is designed to attenuate the ambient magnetic field, reducing the induced magnetisation in the drill core to a level that is significantly lower than the remanent magnetisation. This allows for the measurement of the direction of the remanent magnetisation without interference from the induced magnetisation, which could otherwise alter the orientation of the remanence vector.

As discussed in **Chapter 4**, the residual field within the magnetic shield is a limiting factor in resolving the direction of the magnetic flux density associated with the magnetisation found in weakly magnetised drill cores. The experimental results and FEA provide a method for identifying this limit.

The data presented in Figures 7.1 and 7.2 were used to generate Table 7.1, which details the widths of three regions centred along the main axis of the shield, based on various thresholds for the magnitudes of the three components of the magnetic flux density inside the shield.

Table 7.1: A table comparing the length of three different regions inside a magnetic shield where the magnitude of the residual magnetic flux density, for all three components, was less than three different threshold values. The length of the region reported in the table is centred on the midpoint of the main axis of a two-layer cylindrical magnetic shield.

Threshold (nT)	Simulation length (in mm)	Experiment length (in mm)
< 100.0	457.2	500
< 10.0	237.6	280
< 5.0	156.6	220
< 2.2	56.2	140

The findings in Table 7.1 reveal a region, measuring 140 mm, where the magnitudes of all three components of the magnetic flux density are below 2.2 nT along the main axis of the magnetic shield. Results from the FEA indicate that the maximum magnitude of all three components along the minor axis of the shield is less than 2.4 nT for the diameter of the inner layer (250 mm) of the shield. Additionally, the magnitude of all three components along the vertical axis of the shield is less than 2.4 nT for a region measuring 135 mm along the vertical axis.

Heye and Meyer stated that the internal cavity of a shield should ideally be at least four times the diameter of the drill cores passing through it to prevent distortion of the field originating from the drill core [20]. If the drill core is not aligned with the main axis of the shield, the magnetic field from the side of the core closest to the chamber wall may be distorted by the HPA.

Assuming that the drill cores passing through the measurement system have diameters smaller than 60 mm, there exists a three-dimensional region within the magnetic shield where a portion of the drill core will be exposed to a residual magnetic field, with all three components below 2.4 nT. Additionally, there is sufficient space for the fluxgate magnetometer to occupy this region.

Thus, the drill core should be pushed through the chamber along the main axis of the shield, with the fluxgate magnetometer positioned as close as possible to the core, without allowing the core to induce mechanical vibrations in the fluxgate. Both the drill core and the fluxgate magnetometer must be positioned within the region where the residual field has component magnitudes under 2.4 nT.

Having identified the optimal configuration for the elements of the measurement system, the next section presents an analysis of the response of the measurement system to a magnetic dipole.

7.3 Response to a Magnetic Dipole

The sense elements of a fluxgate magnetometer average the magnetic flux density over the spatial extent of the sense elements [20]. Characterising the response of the measurement system to a single magnetic dipole provided a simple means to test how the system responded to a basic input and to characterise the response of the magnetometer. To do this, a brief analysis of the response of the fluxgate magnetometer to a single magnetic dipole is presented to facilitate the interpretation of more complicated results. This scenario is presented in Figure 7.4 below.

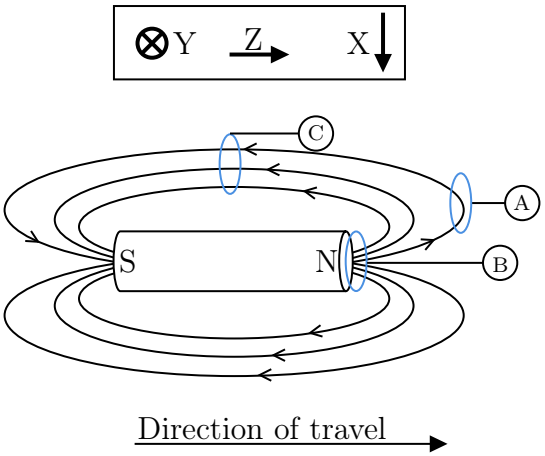


Figure 7.4: A not-to-scale diagram of a synthetic drill core passed under a fluxgate magnetometer, with component orientations depicted. Idealised field lines around the drill core are displayed.

As the drill core approaches the fluxgate magnetometer from the left-hand side, Figure 7.4, the field lines that stretched out, away, from the North pole are first detected by the X and Y components of the magnetometer - region (A) in Figure 7.4 and −300 mm to −57 mm in Figure 7.5. When the North pole is positioned directly beneath the magnetometer - corresponding to region (B) in Figure 7.4 and −57 mm in Figure 7.5 - the only non-zero component will be the Z-component. This is supported by the observation that the field lines at the poles are nearly perpendicular to the edge of the drill core. As the core continues moving under the fluxgate magnetometer, the midpoint between the two poles, region (C) in Figure 7.4, will be encountered when the only non-zero component is the Z-component, −5 mm in Figure 7.5, as the field lines will be perfectly parallel to the magnetic dipole moment. Once the drill core continues to move past the magnetometer, the analysis presented, but in reverse, describes the rest of the behaviour of the magnetic field lines.

The Y-component of the magnetic flux density measured near the synthetic drill core was not considered in the analysis given above. The process of magnetising the magnetic tape used in the synthetic drill cores, ideally, only imparted a permanent magnetisation along the length of the cassette tape and not across the narrow width of the tape: the Y-component would remain zero. Figure 6.7 shows that

when the synthetic core was either close or directly under the Y-component sense element, highlighted by the magenta line, a distinct cluster of measurement points, separate from the rest of the measurements, is found. This unexpected response is due to a non-zero Y-component of the permanent magnetisation of the synthetic core, an alignment error of the synthetic core during the experiment, or a residual magnetisation present on the cassette tape before synthetic core manufacture. It is also possible that the response is a combination of these effects. The presence of orientation or position errors might be corroborated by the asymmetric shape of the lobe of the Z-component, in Figure 7.5, between $-160\,\mathrm{mm}$ and $-70\,\mathrm{mm}$.

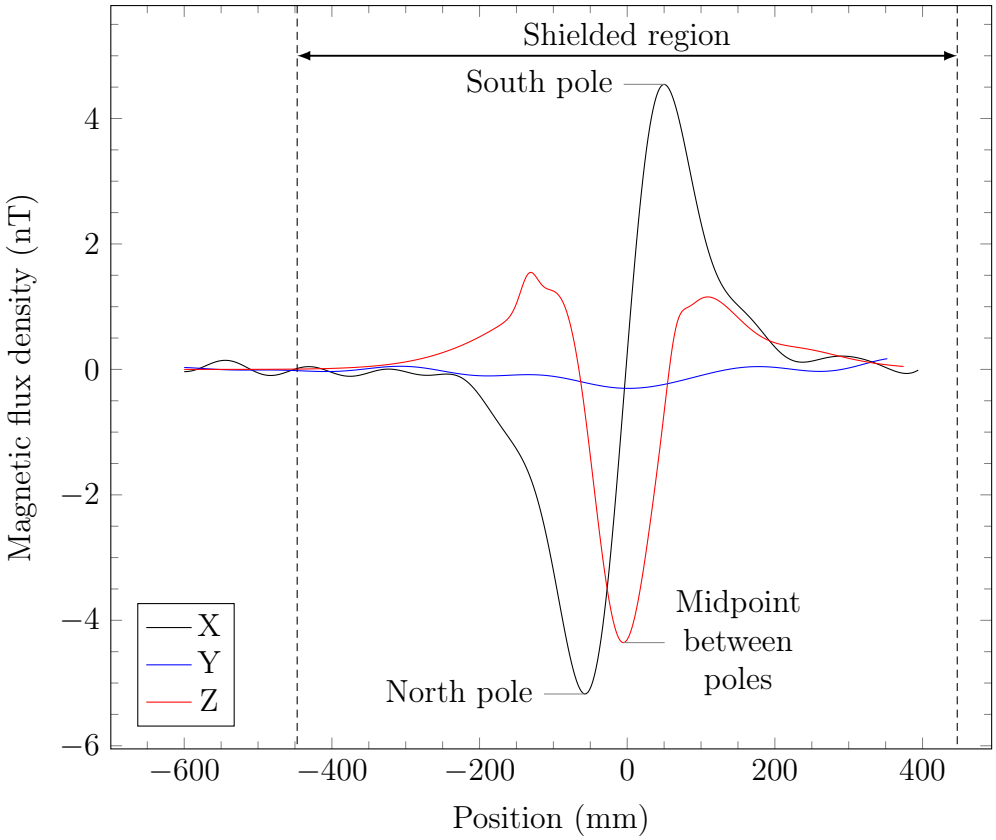


Figure 7.5: The three components of the response of a fluxgate magnetometer to a magnetic dipole as the dipole was moved closer to the fluxgate, directly under the fluxgate, at 0 m, and then away from the fluxgate. The lines of best fit, depicted here, are derived from the measurement points in Figures 6.6, 6.7, and 6.8. The positions of each set of results were adjusted so that at 0 m, all responses corresponded to the dipole being directly under the corresponding sense element inside the magnetometer. The space enclosed by the shield is indicated on the plot as the "shielded region".

The ripple observed in the X-component of the fluxgate magnetometer response, −600 mm to −240 mm in Figure 7.5, was not a measured signal. It originated from the Fourier model fitted to the data.

The −300 mm to −57 mm and 51 mm to 390 mm in Figure 7.5 are referred to as the return field [20]. Noting that the direction of the field lines changes by 180° when tracing out the path of a field line from Ⓑ through Ⓐ and ending at Ⓒ it

can be seen that without careful consideration of this phenomenon, the return field can be interpreted as a magnetic field reversal recorded in a drill core [20]. The straightforward case, shown in Figure 7.5, makes the return field easy to identify. However, more disturbingly, if a comparatively stronger magnetised section of the drill core was adjoined by weakly magnetised sections on either side, it is possible that the return field dominates the weaker fields in the adjoining sections and presents as a magnetic field reversal [20].

The chances of not identifying an artificial magnetic field reversal created by the return field are low. In the inclination and declination (discussed in the next section) of the magnetic flux density recorded by the measurement system, the artificial reversal would appear as a sharp, rapid change followed by a return to the previous values. This behaviour is inconsistent with a genuine magnetic field reversal recorded in the magnetisation of drill cores.

The next section uses synthetic drill cores to create artificial magnetic field reversals used to test the measurement system with known inputs.

7.4 Detecting Geomagnetic Field Reversals

By convention, the geomagnetic field at any point on the Earth is expressed in a spherical coordinate system by two angles - inclination I and declination D - and the magnitude of the magnetic flux density F.

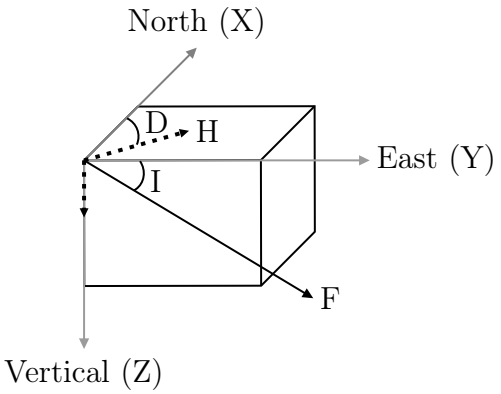


Figure 7.6: A diagram illustrating how the geomagnetic field of the Earth is expressed in spherical coordinates. The diagram is adapted from Lowrie (2007).

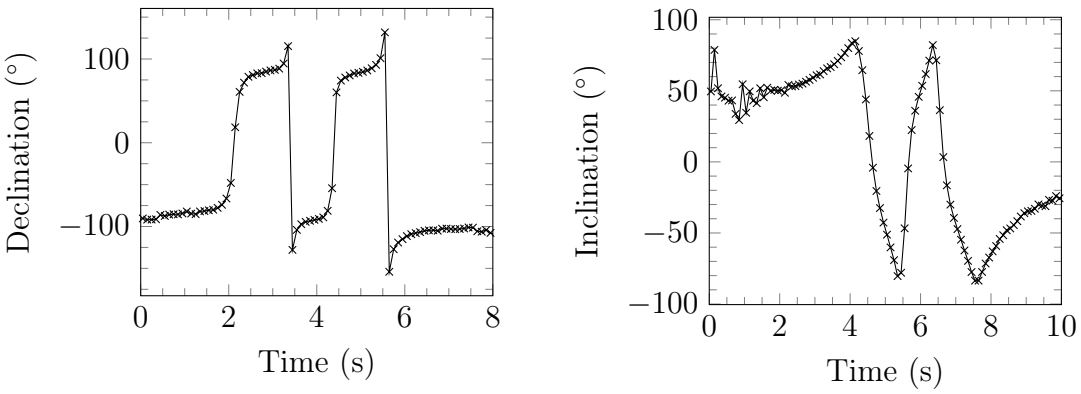
In palaeointensity studies, the inclination and declination of the rock samples are also reported in the coordinate system described by Figure 7.6. The computation of the inclination and declination from the measurements taken by the proposed measurement system facilitates a concise means of comparing the direction of the three-dimensional magnetic flux density vectors in the detection of magnetic field reversals in the drill cores.

Section 7.2 shows that the residual field inside the shield is on the order of a few nanotesla and that the individual components of the residual field are not equal. The computation of the inclination and declination, which is just a conversion from the rectangular coordinate system of the fluxgate magnetometer, from the magnetic flux density of a drill core recorded by the measurement system, is incorrectly determined if the residual field, a DC offset on each component of the measurement, is not removed from the measurements. The individual components of the residual field are not equal, which leads to unequal contributions towards the computation of the inclination and declination. For the inclination and declination of the synthetic and real drill cores presented in the following sections, the residual field was removed from the measurements.

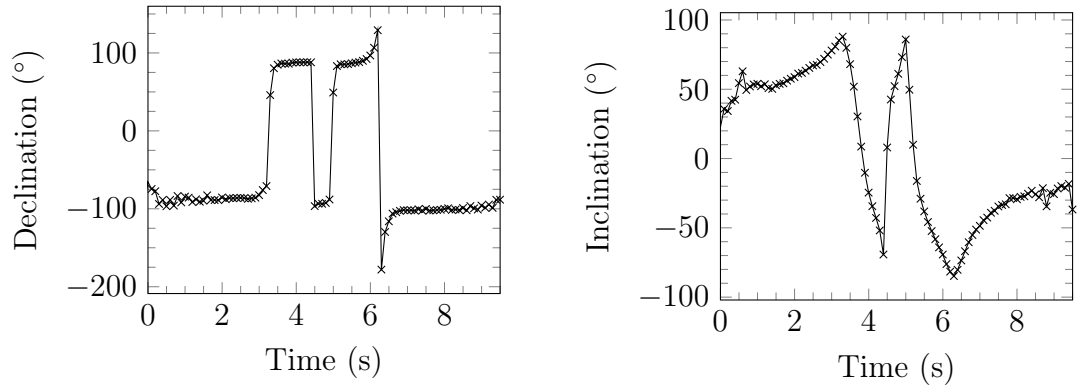
The computation of the inclination and declination arbitrarily assumed the Y and Z components of the fluxgate magnetometer, oriented in Figure 7.4, as the horizontal components and the X component as the vertical component. The exact components that constitute the horizontal plane and the vertical axis are arbitrary in terms of measurements from the measurement system as the results are referenced to the local coordinate system of the fluxgate magnetometer. All that matters is that the same components are consistently used throughout all computations. Expressing these components in terms of the geographic coordinate system requires rotation transformations - discussed in Section 7.6.

The experiment in Section 6.5 laid three synthetic drill cores end-to-end and passed them through the measurement system. The outer synthetic cores had magnetisations in the same direction, while the inner synthetic core had a magnetisation in the opposite direction. The length of the inner synthetic core was decreased until the measurement system was unable to detect a change in the direction of the

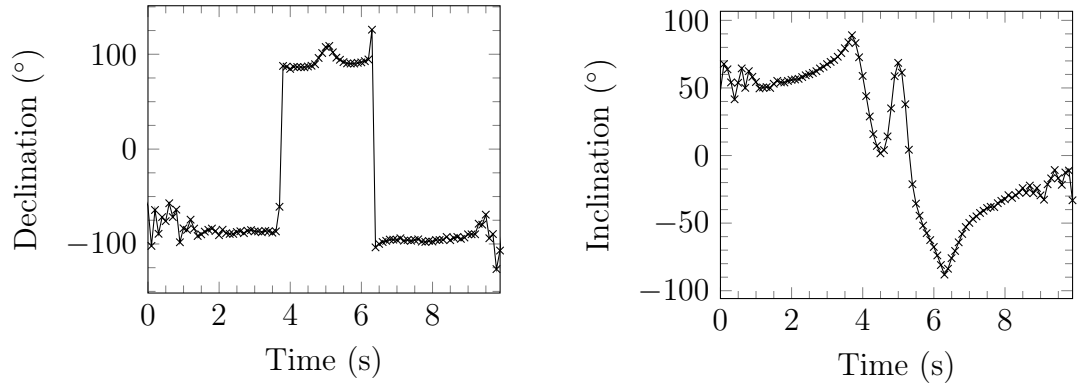
magnetic field. The inclination and declination derived from the results in Figure 6.10 were plotted in Figure 7.7 below.



(a) 50 mm synthetic drill core: Declination (left) and Inclination (right).



(b) 30 mm synthetic drill core: Declination (left) and Inclination (right).



(c) 20 mm synthetic drill core: Declination (left) and Inclination (right).

Figure 7.7: Plots of the computed declination and inclination of the magnetic flux density where the width of the centre synthetic drill core was varied. The polarity of the magnetisation of the outer synthetic drill cores was the same, while the centre synthetic drill core had the opposite polarity.

A perfect change in the direction of a magnetisation such that the vector is anti-parallel to the original vector necessitates a 180° and 90° change in the declination and inclination, respectively. The results show that the fluxgate magnetometer was able to discern complete reversals in the direction of the magnetic flux density associated with the centre synthetic drill core having a length greater than 30 mm. For the synthetic core with a length of 20 mm, the fluxgate was unable to identify the reversal. There are two reasons for this behaviour. First, the averaging of the flux density over the active length of the sensor and the smaller distribution of magnetic dipoles on the reversed synthetic drill core causes the larger contributions from the outer synthetic drill cores to average out the smaller reverse contribution [20]. Secondly, it is possible that the return fields from the outer synthetic drill cores dominated the smaller field originating from the reversed drill core.

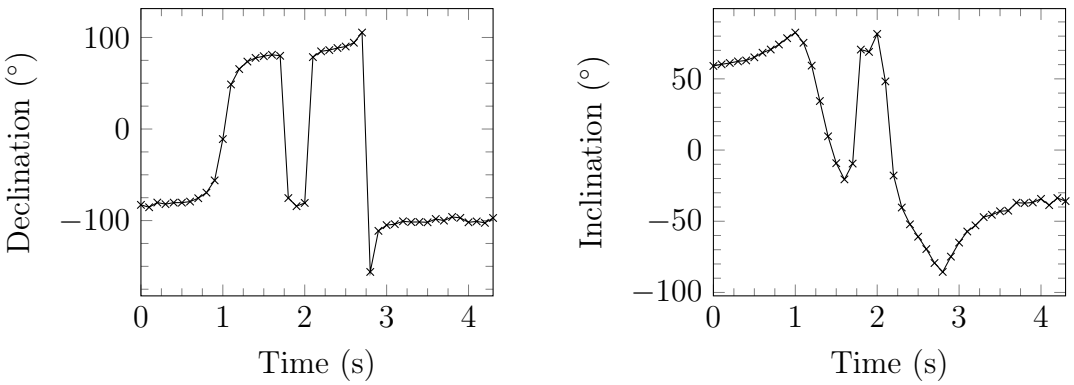
The other notable features are minor peaks before and after a 180° change in declination. These result from edge effects (the return field) - discussed in Section 7.3.

Two additional effects introduced errors and artifacts in the presented data. First, the tilted normal (2.55 s and 5 s) and reverse (4 s) polarity regions of the declination and inclination, in Figure 7.7a, are attributed to orientation errors introduced during the measurements. These errors originated from the misalignment of the synthetic drill core standards. Second, the abrupt shift between normal and reversed polarity does not originate from the drill core measurements. Instead, it is an artefact of the method used to calculate the declinations. The output of the `arctan2` function is restricted to ±90° and ±180° ranges for the inclination and declination, respectively. When the true value exceeds this limit, the output wraps around to the opposite extreme and adds or subtracts the difference, creating the appearance of a sudden change in direction. For a synthetic example such as Figure 7.7, the overflow nature of the `arctan2` function facilitated the identification of the reversals. The behaviour of this function can be misleading in the interpretation of data from real drill cores.

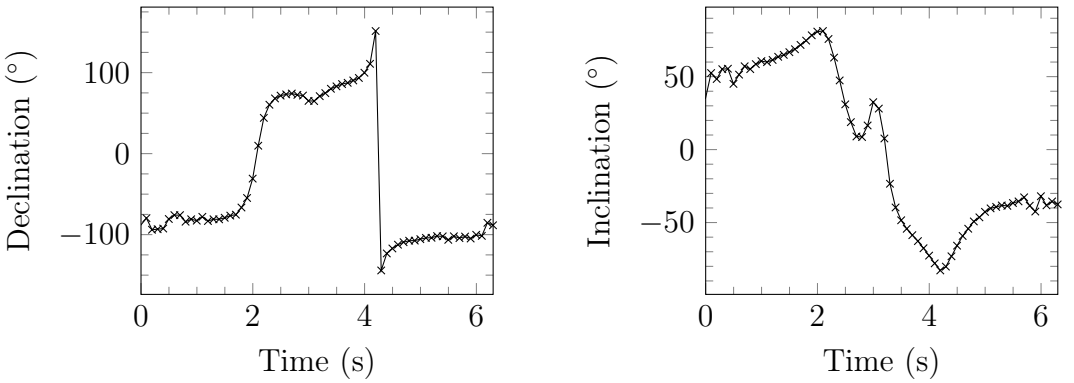
A second experiment replaced the centre synthetic drill core with reverse magnetisation, with a space. This served to evaluate the effect that may occur when the

ends of two consecutive drill cores were connected before being passed through the proposed measurement system.

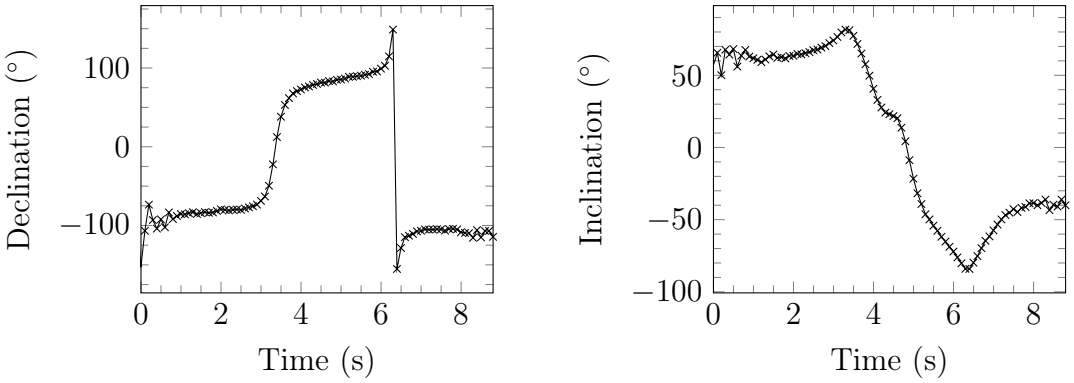
Two synthetic standards with the same polarities were selected for the experiment as it was assumed that there would not be significant declination and inclination variations over a few millimetres. The inclination and declination derived from the results in Figure 6.11 were plotted in Figure 7.8.



(a) 50 mm gap: Declination (left) and Inclination (right).



(b) 30 mm gap: Declination (left) and Inclination (right).



(c) 20 mm gap: Declination (left) and Inclination (right).

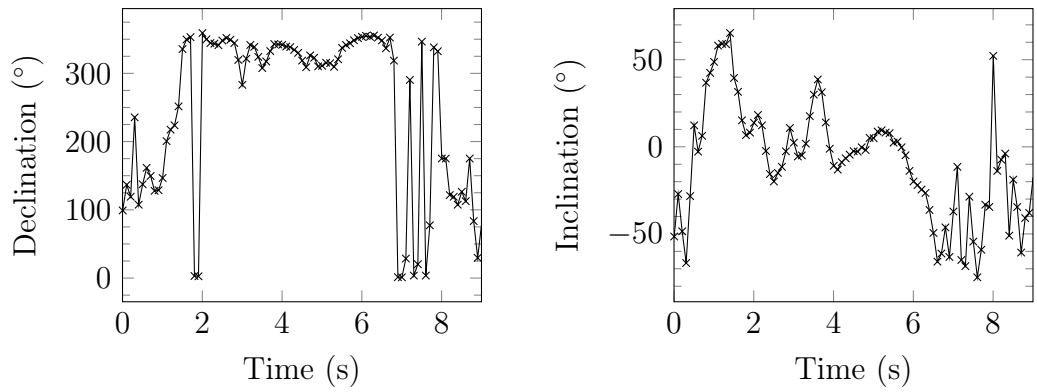
Figure 7.8: Plots of the change in declination and inclination of the magnetic flux density, for three experiments, each with a different length space between two synthetic drill cores having magnetisations with the same polarities.

The results in Figure 7.8 indicate that when the gap between consecutive synthetic cores was 20 mm, the magnetic field behaved as if there were no gap between the cores. To ensure accurate inclination and declination computations, it is recommended that, during a measurement campaign involving multiple sequential drill cores, the cores either be passed through the measurement system individually or placed end-to-end with minimal spacing between consecutive cores to avoid introducing artifacts.

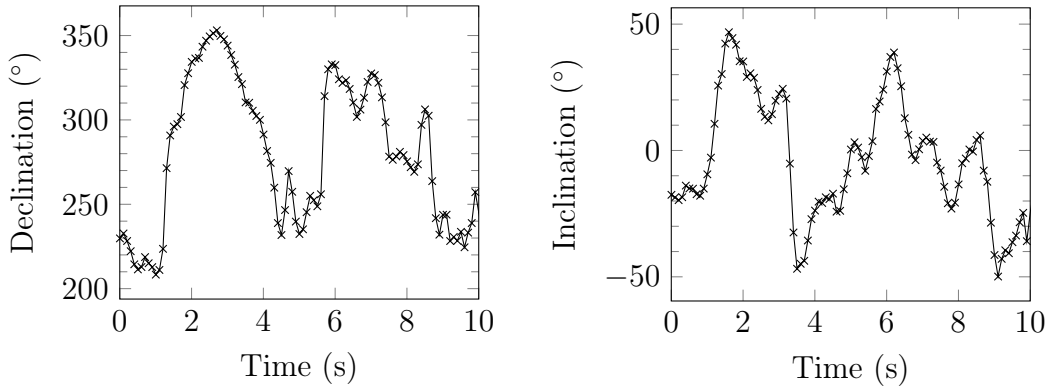
7.5 Bushveld Igneous Complex Drill Cores

With the method used in Section 7.4, measurement of the magnetic flux density, in three sequential sections of short drill cores, Figures 6.15 to 6.17, recovered from the BIC, were expressed as inclinations and declinations in Figure 7.9. The declinations were not constrained to the principle angles ($\pm 180°$). A procedure to unwrap the result was implemented so that the declinations were constrained between 0° and 360° to try to reduce the artefacts, prominent in Figure 7.7.

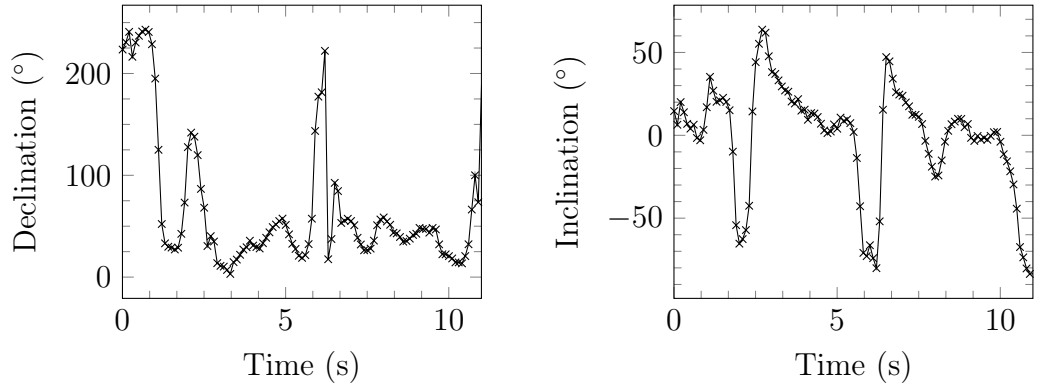
The sharp peaks and troughs visible in Figure 7.9a appear to show large changes in the direction of the declination. When the declination angle is close to 0° or 360°, a small change in the angle is sufficient to cause the `acrtan` function output to wrap around. For example, the trough at 2 s in Figure 7.9a is not a significant variation.



(a) Drill core 4/3: Declination (left) and Inclination (right).



(b) Drill core 4/4: Declination (left) and Inclination (right).



(c) Drill core 4/5: Declination (left) and Inclination (right).

Figure 7.9: Plots of the change in declination and inclination of the magnetic flux density, for three drill cores taken from the Main Zone of the BIC.

In the future, a different method to facilitate a comparison in the direction of the

magnetic fields should be investigated to mitigate the wrap-around issue. The requirement that the inclination and declination be computed with the DC offsets of the residual field removed also makes the output of the `arctan` function unstable, and significant swings in inclination and declination are reported due to the close to zero, but non-zero, values of the corrected DC offsets. Clipped for clarity, an example of the sensitivity to noise (0–2 s and 8–10 s) is seen at the start and end of the inclination and declination plots in Figure 7.7c.

The inclination presented in Figure 7.9c is suspicious as it is periodic. The source of this spurious signal is unknown. It is unlikely that the rocking motion of the drill core, with respect to the position of the fluxgate magnetometer, would create low-frequency periodic signals as experience has shown that this motion manifests as a high-frequency component in the signal.

Apart from the rapid changes in inclination and declination due to the wrap-around issue, the smoothness of the data suggests that DIRM is not present in the drill cores - strong DIRM would manifest as constant inclinations and declinations. The small variation in the declination between 2.1 s and 4 s in Figure 7.9a is likely due to natural variation in the remanent magnetisation and mineralogy of the drill core and not a DIRM. In contrast, the characteristic dipole response, Figure 6.20, of the measurement system to the Critical Zone drill core (image in Figure 6.18) indicates a potential DIRM. Further investigation found that the drill core was recovered from an outcrop with a hand drill. The short length of this drill core and the apparent lack of any natural remanent magnetisation make plotting the inclination and declination of little value.

The primary objective of measuring these cores was to demonstrate that even weak remanent magnetisation—recorded by cores with low magnetic susceptibilities—can be detected by the measurement system. This section outlines a potential approach to decode the magnetic flux density information gathered from the drill cores while also highlighting the challenges that must be considered when developing a field-deployable version of the measurement system.

In **Chapter 2**, Eq 2.6 was derived to estimate the magnetic flux density at various positions from a magnetic dipole moment, based on measurements of the natural

remanent magnetisation in drill cores by Letts et al. Table 4.1 lists the magnetic flux densities associated with these remanent magnetisations and measurement positions. Notably, the sample with the weakest NRM (see Table 4.1) had a magnetic susceptibility of 6.92×10^{-4} SI Units, which is on the same order of magnitude as the magnetic susceptibilities recorded from drill cores 4/3 to 4/5 - Figure 6.13 [5].

Magnetite has a magnetic susceptibility between 1–10 SI Units, which indicates that the Main Zone drill cores should be weakly magnetic [10]. Drill cores 4/3 to 4/5 have average magnetic flux density magnitudes of 1.47 nT, 1.93 nT, and 2.04 nT, respectively, which are consistent with the magnetic flux densities measured 40 mm away from a hypothetical dipole with a magnetisation of 0.02 A/m at both perpendicular and parallel angles relative to the dipole - from Table 4.1.

These consistencies and same localities within the BIC suggest that, on average, the drill cores from the Main Zone are suitable representatives for samples with magnetic flux densities on the lower bound of the minimum field size expected to be measured from drill cores in the Main Zone, by the proposed measurement system.

7.6 Oriented Drill Core

A complication overlooked in previous analyses and experiments was the need to consider the orientation and position of single and sequential drill cores within the measurement system to facilitate the comparison of results. When the magnetisation of a rock unit was acquired at the time of formation, ignoring geologic processes for simplification, the unit of rock was fixed in place and could not translate or rotate. When a drill core is extracted from a rock unit, the drill core can be positioned in any arbitrary direction in three-dimensional space: the direction of the magnetisation can be set in any direction.

In three-dimensional space, the trajectory of a point in a borehole is described by the azimuth and tilt (or inclination) angles - Figure 7.10. The position of a drill core inside a borehole is described by these two angles and an additional angle θ_{roll},

referred to as the orientation in this discussion, that describes the direction that an arbitrary point on the drill core faces with a corresponding point on the borehole wall.

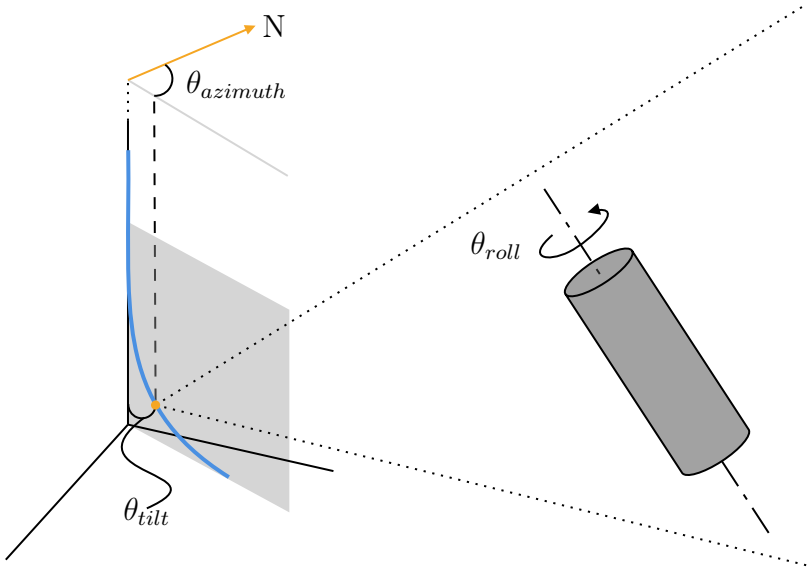


Figure 7.10: A diagram depicting the two angles used to describe the trajectory, blue line, of a borehole in three-dimensional space and a third angle, θ_{roll}, that describes the direction that the drill core faces. The borehole is constrained to the grey plane, which is parallel to the vertical axis and not orthogonal to either horizontal axis. Borehole trajectory diagram adapted from Figure 3 in [59].

For the detection of geomagnetic reversals, with the proposed measurement system, in a series of drill cores recovered from the same borehole, two constraints apply to the orientation and position of the drill cores in the measurement system.

First, θ_{roll} must be the same for all drill cores. In other words, the drill core segments can be reassembled in a continuous line that results in a unique and unambiguous orientation, ensuring that the *relative* orientation of each segment is consistent with the original relative orientations in the rock units before being drilled out. If there are core breakages or loss of core, new oriented segments will have to be made in such a way that they are still consistent with the relative orientation of the other drill cores. This could be done by using the geological dip or downhole imaging from a televiewer tool. The *absolute* angle for θ_{roll}, with

respect to the geographic coordinate system, does not have to be considered.

Second, the distances between points of measurement on the drill core, directly under the fluxgate magnetometer (Figure 6.1a), must be the same for all measurements. Consider Figure 7.11, when directly under the fluxgate magnetometer, the vertical distance, d_A, between region A of the drill core and the fluxgate sensor, indicated by the black dot, is greater than the vertical distance, d_B, between region B of the drill core and the fluxgate magnetometer. An inspection of Eq 2.6 shows that the strength of the magnetic flux density is inversely proportional to the cube of the position between the magnetic dipole moment (or magnetisation) and the point of measurement. A comparison of Figures 6.14 and 6.15 shows the change in magnitude of the magnetic flux density with vertical distances of 87 mm and 10 mm between the same drill core and fluxgate magnetometer, respectively.

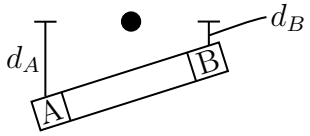


Figure 7.11: A diagram that illustrated how the position of a drill core, white rectangle with two regions of measurement (A and B), would alter the distance, d_A and d_B between the regions of measurement and the fluxgate magnetometer (black dot).

By not using the same position for every drill core in the measurement system, comparisons of the results or computations based on the results will be unfair, as the intensity of the flux density associated with the magnetisations in the drill cores, closer to the fluxgate, will be larger. The implication is that the measured flux density will depend on the measurement distance *and* the magnetisations inherent to the minerals in the core. The separation of these two factors would add unnecessary complexity and allow for the introduction of measurement errors.

The application of the two constraints ensures that the inclinations and declinations, computed from the magnetic flux density reported by the measurement system, can be compared across the full length of the borehole and are expressed in the *local coordinate system* of the fluxgate magnetometer inside the measurement

system. Provided that the azimuth, tilt, and orientation (θ_{roll}) of the drill cores are known, rotation transformations will have to be applied if the measurements, and computations based on them, are expressed in the geographic coordinate system.

Transformation of the results to the geographic coordinate system would facilitate comparison of the measurements with magnetic flux density data recorded by a magnetometer lowered down the borehole, for example. These two sets of measurements could be used to corroborate or support the detection of a reversal in one dataset if the reversal is evident in the other dataset. However, three-component downhole magnetic flux density data is not always available.

7.7 Alternative Applications

The primary application of the proposed measurement system was explored, and findings based on measurements from this system were presented. However, the measurement system can also be utilised as a tool in the targeted drilling of boreholes.

In the Northern Territory of Australia, an aeromagnetic survey was conducted, and a magnetic anomaly was identified near Tennant Creek [60]. Magnetic anomalies occur when local variations in rock properties create differences in the ambient magnetic field. These differences can be due to variations in induced magnetisation (resulting from a magnetic susceptibility that differs in the surrounding rock units) or remanent magnetization (acquired during formation and possibly altered during subsequent chemical or physical processes). However, interpretation of the origin of magnetic anomalies is sometimes done without consideration of the presence of remanent magnetisation [60].

In some geologic settings, the dominant component of the magnetic anomaly is the induced magnetisation, which is sometimes why remanent magnetisation is excluded. Furthermore, induced magnetisation, inferred by the measure of magnetic susceptibility with a handheld tool, is significantly faster and easier to measure in situ than remanent magnetisation.

The Rover 3 magnetic anomaly was identified as having a weaker residual magnetic

flux density (in other words, the remaining flux density after the ambient geomagnetic field was removed) than the surrounding rock units [60]. Subsequently, a borehole was drilled to intersect the anomaly in the hope that the anomaly corresponded to an economic mineral deposit [60]. However, the focus of the exploration team on the induced magnetisation led them to underestimate the role of remanent magnetization. As a result, although the borehole intersected the target at 400 m, drilling continued to 738 m, incurring an additional 338 m of unnecessary expense as the magnetic susceptibility measurements, even once the target was intersected, were not correlated with the expected values which would be responsible for the anomaly if it was due to an induced magnetisation [60].

In 2014, Austin and Foss investigated samples from the borehole and showed that the anomaly was predominantly due to the remanent magnetisation of the rock units intersected by the borehole [60]. If the presence of remanent magnetisation was considered in preliminary forward modelling and subsequent inversion of the data from the borehole, the exploration team may have realised the target was intersected much sooner.

This discussion highlights the possible value of the proposed measurement system, which, when deployed in situ alongside traditional magnetic susceptibility tools, could provide a more complete assessment of the magnetic properties of the drill cores.

7.8 Limitations

Throughout the investigation, two key limitations were identified during the application of the measurement system in the detection of geomagnetic reversals in continuous drill cores.

First, a fundamental requirement in the analysis of the remanent magnetisation in palaeomagnetic study is the ability to determine the origin of the individual components of the resultant magnetisation. In doing so, the primary remanent magnetisation is isolated and used to infer the direction and intensity of the geomagnetic field at the time of formation of the rock sample.

The aim of the proposed measurement system did not seek to distinguish between the components of the total remanent magnetisation. Instead, it relied on the assumption that the primary remanent magnetisation was the dominant component in the resultant magnetisation of the sample. In doing so, the magnetic flux density, measured by the fluxgate magnetometer inside the measurement system, was used as a proxy for the detection of changes in the direction of the primary remanent magnetisation - an indication of a geomagnetic reversal. The use of the magnetic shield helped to improve the validity of this assumption as the induced magnetisation was considered negligible. However, the assumption that the magnetisation acquired from drilling and handling was less than the primary remanent magnetisation may not always be true. The stability and strength of the drilling-induced remanent magnetisation can vary widely as the mineral constituents of a drill core control these properties.

However, there might be means of identifying suspicious segments of data reported by the proposed measurement system. For example, Williams noted that drilling overprints were frequently encountered in the ODP and that the overprint component of the magnetisation tended to be pointed vertically, along the path of the drill string, and perpendicular to the main axis of the drill core [61]. The vertical component of the magnetisation due to the DIRM would manifest as steep inclinations based on computations of the magnetic flux density reported by the proposed measurement system. The application of alternating field demagnetisation, with peak fields of 20 mT, was successful in the removal of the overprint components in drill cores from the ODP [61]. It must be noted that these findings were based on sedimentary sequences and that the conclusions may not hold for the igneous rocks in the BIC. In general, for drill cores recovered from a borehole, the direction of the remanent magnetisation in drill cores with strong primary magnetisations would be less prone to alteration by DIRM due to the magnitude of the primary remanent magnetisation dominating the resultant magnetisation. For the removal of overprints in drill cores from the BIC, Letts et al. showed that alternating fields with peaks of 50 mT were required for the removal of overprints in some of the samples collected from the Main Zone of the Eastern Lobe [5].

In terms of DIRM in drill cores, de Wall and Worm went on to show that for the

superdeep boreholes drilled by the German Continental Deep Drilling Program, the DIRM was strongest on the outside of the drill cores and that specimens, for analysis in a spinner magnetometer, with significantly less DIRM were recovered from samples taken from centre sections of the drill cores [62]. The proposed measurement system was designed for the bulk and rapid measurement of large lengths of drill core; the extraction of samples from the inside of the core is not practical. Therefore, if the DIRM is strong enough to significantly alter the direction of the primary magnetisation, the use of the proposed measurement system may be limited unless the application of rapid alternating field demagnetisation is explored.

The second limitation has to do with a classical consideration in the application of any measurement system: how many measurements must be taken to obtain a result that is representative of the sample? In the context of the proposed measurement system, this question manifested as the identification of the number of fluxgate magnetometers required to acquire an accurate measurement of the magnetic flux density in the drill cores.

For a homogenously magnetised drill core, a single three-component fluxgate magnetometer is sufficient for the complete representation of the dipole magnetic field. In a highly inhomogeneous drill core, the total magnetic field from the magnetisation may require the use of more than one three-component magnetometer to capture a complete representation of the magnetic field. For example, the effects of a region with an appreciably different magnetisation, located on a side of the drill core not in direct contact with the fluxgate magnetometer, may be attenuated or absent from the field measured by the fluxgate magnetometer.

7.9 Recommendations

From the analysis of the limitations of the measurement system, two sets of recommendations can be made to mitigate these issues.

The nature of DIRM in drill cores will vary between cores having differing mineralogies. In general, the DIRM is imparted on MD grains of the cores as these grains require less energy to remagnetise than SD grains (the carriers of primary remanent

magnetisation). An implication is that less energy is required to demagnetise the MD grains. The use of a rapid, inline, alternating field demagnetisation setup would help to attenuate the effects of the permanent magnetisation recorded by the MD grains without affecting the magnetisation of the SD grains. The strength and frequency of the demagnetising field have been studied extensively in the literature in the context of palaeomagnetic study, and further research is required for the development of a rapid demagnetisation setup that can be used with the proposed measurement system. Careful consideration of the placement of the demagnetisation setup must be considered as the demagnetising field may be detected by the magnetometers inside the proposed measurement system.

The question of representative measurement of the flux density in the drill cores is resolved with two solutions. First, multiple three-component fluxgate magnetometers could be installed to record the magnetic flux density associated with the remanent magnetisation of the drill cores in different positions around the drill core. Care must be taken to ensure that the fluxgate magnetometers are not placed too close to each other, as there is the potential for them to interfere with one another. Second, a single three-component fluxgate magnetometer can be used provided that the drill cores are passed through the measurement system multiple times, with the orientation of the drill cores changing each time. The first solution is more favourable as multiple measurements of the same drill core will increase the time required to analyse the full length of drill cores recovered from a borehole.

Several other recommendations are required for the improvement of the proposed measurement system so that it can be used in a measurement campaign with continuous drill cores.

First, with the current requirements of the measurement system, the ability to rapidly measure the remanent magnetisation in the drill cores necessitated the disregard for the association of positions with the measurements taken along the drill cores. If a position is to be associated with the drill cores, the diagram presented in Figure 7.12 facilitates this requirement.

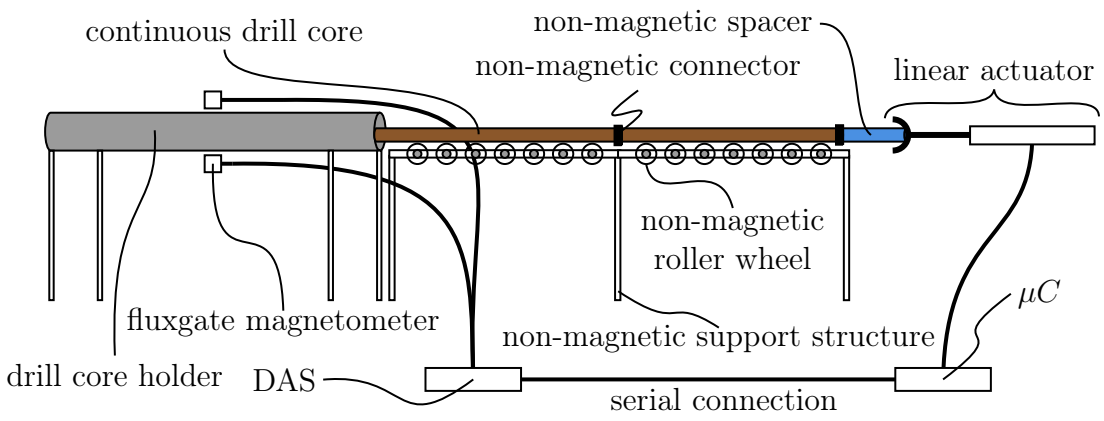


Figure 7.12: A simplified diagram, excluding the magnetic shield for clarity, of an automated version of the proposed measurement system where the only user intervention required is the loading of drill core and initiation of the measurement procedure.

A linear actuator, with non-magnetic spacers between the contact point of the actuator and the drill cores, is used to push the drill cores through the measurement system. The TDX DAS accepts a serial data stream that is timestamped and appended to the UDP output, along with the sensor measurements [38]. The position of the linear actuator, which is controlled and reported by a microcontroller (μC), can be streamed to the TDX. This results in the UDP output containing magnetic flux density measurements and positions of the drill cores. In applying this recommendation, the time taken to analyse drill cores is increased as time must be spent connecting the cores to the linear actuator. The intended use of the measurement system must be considered before implementing this improvement. One approach could be to analyse the full length of the drill core without precise position tracking, recording only rough positions for core sections. Later, selected sections of interest could be analysed with accurate positions.

The inclusion of a device, under control by software, to push the drill cores through the measurement system facilitates a reduction in position errors and affords the ability to implement different modes of operation of the system. For example, one mode could continuously push the drill cores through the system, while another mode could push the cores through in increments to allow for multiple measurements

of the same position. This would facilitate the computation of an average of the magnetic flux density for every position measured along the drill cores for a more detailed analysis.

Second, the PVC drill core holder, Figure 6.1b, should be replaced with a structure that reduces the friction between the drill cores and the support material. Long sections of drill core are supported by a table containing roller wheels to reduce the effort required to push the core through the measurement system. Individual sections of drill core are held together by non-magnetic clamps so that the relative orientation of the cores is enforced.

Third, the magnetic permeability of the shielding material can be lowered by mechanical deformation, stress, and shock. The addition of a protective aluminium box around the outside of the magnetic shield, with foam between the shield and walls of the box, should be considered. It is best to avoid carrying the shield directly; rather, a wooden platform should support the shield and that platform be carried to avoid applying mechanical strain to the shielding material.

In general, the proposed measurement system is modular and additional components can be added around it. For example, a washing station to clean the drill cores of contaminants from the drilling process could be added before the drill cores are passed through the measurement system.

This chapter presented an analysis of the agreement between the FEA results and experimental measurements used to validate the simulation. Once it was discovered that the results agreed reasonably well with the experimental measurements, the FEA was used to quantify the nature of the magnetic flux density gradients inside the shield and how to best position the fluxgate magnetometers and drill cores inside to perform measurements in the weakest possible residual field in the shield. In doing so, the ability of the measurement system to resolve changes in the direction of synthetic drill cores was proven, and it was found that the magnetic flux density associated with short sections of real drill cores was resolvable. However, the short nature of the drill cores made it difficult to extract any meaningful data. The section concluded with an identification of the limitations in the measurement system and possible methods to improve the operation of the setup so that it can

be deployed at a drill site or drill core storage facility.

The next chapter concludes the investigation.

Chapter 8

Conclusion

The absence of commercial measurement systems capable of rapidly assessing the magnetic flux density associated with remanent magnetisation in continuous drill cores motivated the development of a prototype measurement system. This prototype successfully measured the direction of magnetic flux density near weakly magnetised drill cores from the Main Zone. However, analysis of approximately 1 m of drill core did not reveal any clear trends in the inclination or declination of the measured magnetic fields.

Experiments with synthetic drill cores confirmed the ability to resolve directional changes in magnetic flux density down to approximately 10 nT. Additionally, the system successfully detected geomagnetic reversals in synthetic drill cores, provided the reversed polarity region was at least 30 mm thick. These results suggest that, as long as DIRM is not a dominant component of the total magnetisation, the measurement system can identify reversals in the magnetic field recorded by drill cores from the BIC.

Recommendations were provided to improve the measurement system for deployment in a larger measurement campaign. Alternative methods for visualising the direction of the magnetic flux density, beyond computing inclination and declination, should be explored to facilitate interpretation.

A key contribution of the investigation was the simulation and validation of a

magnetic shield using the open-source Elmer FEM software. No prior literature had verified Elmer FEM codes for this specific application. This validation not only demonstrates that Elmer FEM produces reliable results but also highlights the potential as an open-source alternative to proprietary commercial software for the design and analysis of magnetic shields.

References

[1] Roberto Lanza and Antonio Meloni. 'Paleomagnetism'. In: *The Earth's Magnetism: An Introduction for Geologists*. Berlin, Heidelberg: Springer Berlin Heidelberg, 2006, pp. 127–176. DOI: 10.1007/978-3-540-27980-8.

[2] Maylis Landeau et al. 'Sustaining Earth's magnetic dynamo'. In: *Nature Reviews Earth & Environment* 3.4 (Apr. 2022), pp. 255–269. ISSN: 2662-138X. DOI: 10.1038/s43017-022-00264-1.

[3] Anita Di Chiara et al. 'The strength of the Earth's magnetic field from Pre-Pottery to Pottery Neolithic, Jordan'. In: *Proceedings of the National Academy of Sciences* 118.34 (2021). DOI: 10.1073/pnas.2100995118.

[4] R. Cawthorn. 'The Platinum Group Element Deposits of the Bushveld Complex in South Africa'. In: *Platinum Metals Review* 54 (Oct. 2010), pp. 205–215. DOI: 10.1595/147106710X520222.

[5] Shawn Letts et al. 'Palaeomagnetism of the 2054 Ma Bushveld Complex (South Africa): implications for emplacement and cooling'. In: *Geophysical Journal International* 179.2 (Nov. 2009), pp. 850–872. ISSN: 0956-540X. DOI: 10.1111/j.1365-246X.2009.04346.x.

[6] Grant R. Cawthorn and Susan J. Webb. 'Cooling of the Bushveld Complex, South Africa: Implications for paleomagnetic reversals'. In: *Geology* 41.6 (June 2013), pp. 687–690. ISSN: 0091-7613. DOI: 10.1130/G34033.1.

[7] Susan J. Webb et al. 'Gravity modeling of Bushveld Complex connectivity supported by Southern African Seismic Experiment results'. In: *South African Journal of Geology* 107.1-2 (June 2004), pp. 207–218. ISSN: 1012-0750. DOI: 10.2113/107.1-2.207.

[8] R. B. Trumbull et al. ‘Drilling through the largest magma chamber on Earth: Bushveld Igneous Complex Drilling Project (BICDP)’. In: *Scientific Drilling* 19 (2015). DOI: 10.5194/sd-19-33-2015.

[9] Clive Foss, Keith Leslie and Wayne Stuart. ‘A moving 3 component fluxgate magnetometer to measure remanent and induced magnetizations in drill core’. In: *ASEG Extended Abstracts* 2015.1 (2015), pp. 1–3. DOI: 10.1071/ASEG2015ab067.

[10] William Lowrie. ‘Geomagnetism and paleomagnetism’. In: *Fundamentals of Geophysics*. Cambridge University Press, 2007, pp. 281–362. DOI: 10.1017/CBO9780511807107.

[11] Lisa Tauxe et al. *Essentials of Paleomagnetism*. Berkeley, CA: University of California Press, Mar. 2010. DOI: 10.1525/9780520946378.

[12] I. Lascu et al. ‘What does it mean to be pseudo single domain? Demystifying the PSD state’. In: *AGU Fall Meeting Abstracts*. Vol. 2016. AGU Fall Meeting Abstracts. Dec. 2016, GP22A-01, GP22A–01.

[13] Michael J. Pinto and Michael McWilliams. ‘Drilling-induced isothermal remanent magnetization’. In: *GEOPHYSICS* 55.1 (1990), pp. 111–115. DOI: 10.1190/1.1442765.

[14] David J. Griffiths. ‘Magnetostatics’. In: *Introduction to Electrodynamics*. Cambridge University Press, 2023, pp. 209–267. DOI: 10.1017/9781009397735.006.

[15] Salvatore Celozzi et al. ‘Magnetic Shielding’. In: *Electromagnetic Shielding*. John Wiley and Sons, Inc, 2023. Chap. B, pp. 459–481. DOI: 10.1002/9781119736318.app2.

[16] Peter Sergeant et al. ‘Analytical formulation for magnetic shields taking into account hysteresis effects in the Rayleigh region’. In: *COMPEL - The international journal for computation and mathematics in electrical and electronic engineering* 24.4 (Jan. 2005), pp. 1470–1491. ISSN: 0332-1649. DOI: 10.1108/03321640510615733.

[17] Salvatore Celozzi et al. ‘Numerical Methods for Shielding Analyses’. In: *Electromagnetic Shielding*. John Wiley and Sons, Inc, 2023. Chap. 7, pp. 169–255. DOI: 10.1002/9781119736318.ch7.

[18] Arnulf Kost. 'Different Methods for Computational Electromagnetics: Their Characteristics and Typical Pratical Applications'. In: *Computational Methods for the Innovative Design of Electrical Devices*. Ed. by Sławomir Wiak and Ewa Napieralska-Juszczak. Berlin, Heidelberg: Springer Berlin Heidelberg, 2011, pp. 261–275. DOI: 10.1007/978-3-642-16225-1_15.

[19] R. Szewczyk, A. Ostaszewska-Liżewska and P. Råback. 'Modelling the Fluxgate Sensors with Magnetic Field Concentrators'. In: *Acta Physica Polonica A* 137.5 (May 2020), pp. 700–702. DOI: 10.12693/APhysPolA.137.700.

[20] D. Heye and H. Meyer. 'Ein Meßverfahren zur paläomagnetischen Messung an Tiefseesedimentkernen an Bord eines Schiffes'. In: *Zeitschrift für Geophysik* 38 (1972), pp. 937–947. URL: https://resolver.sub.uni-goettingen.de/purl?PPN101433392X_0038 (visited on 05/11/2024).

[21] Mark Noel, Morgan Pickering and Lindsay Molyneux. 'An Instrument For Measuring the Axial Remanent Magnetization of Long Sediment Cores'. In: *Geophysical Journal International* 97.1 (Apr. 1989), pp. 95–101. ISSN: 0956-540X. DOI: 10.1111/j.1365-246X.1989.tb00487.x.

[22] R.F. Butler. *Paleomagnetism: Magnetic Domains to Geologic Terranes*. Blackwell Scientific Publications, 1992. ISBN: 978-0-865-42070-0.

[23] Robin Weeks et al. 'Improvements in long-core measurement techniques: applications in palaeomagnetism and palaeoceanography'. In: *Geophysical Journal International* 114.3 (Sept. 1993), pp. 651–662. ISSN: 0956-540X. DOI: 10.1111/j.1365-246X.1993.tb06994.x.

[24] William S. Goree. 'Rock Magnetometer, Superconducting'. In: *Encyclopedia of Geomagnetism and Paleomagnetism*. Ed. by David Gubbins and Emilio Herrero-Bervera. Dordrecht: Springer Netherlands, 2007, pp. 883–886. DOI: 10.1007/978-1-4020-4423-6_283.

[25] Pavel Ripka, ed. *Magnetic Sensors and Magnetometers*. 2nd ed. Artech, 2021. ISBN: 978-1-630-81743-5.

[26] Bureau of Industry and Security. *Chapter VII - Supplement No. 1 to Part 774 - The Commerce Control List*. Tech. rep. Last updated: 16 January 2025. United States Department of Commerce, 2025. URL: www.bis.gov/ear/title-15/subtitle-b/chapter-vii/subchapter-c/part-774/supplement-no-1-part-774-commerce-control#category6 (visited on 22/01/2025).

[27] D. Drung et al. 'Highly Sensitive and Easy-to-Use SQUID Sensors'. In: *IEEE Transactions on Applied Superconductivity* 17.2 (2007), pp. 699–704. DOI: 10.1109/TASC.2007.897403.

[28] W. S. Goree and M. Fuller. 'Magnetometers using RF-driven squids and their applications in rock magnetism and paleomagnetism'. In: *Reviews of Geophysics* 14.4 (1976), pp. 591–608. DOI: 10.1029/RG014i004p00591.

[29] Antonio Vettoliere and Carmine Granata. 'Highly Sensitive Tunable Magnetometer Based on Superconducting Quantum Interference Device'. In: *Sensors* 23.7 (2023). ISSN: 1424-8220. DOI: 10.3390/s23073558.

[30] D. I. Gough. 'A spinner magnetometer'. In: *Journal of Geophysical Research (1896-1977)* 69.12 (1964), pp. 2455–2463. DOI: 10.1029/JZ069i012p02455.

[31] L. Molyneux. 'A Complete Result Magnetometer for Measuring the Remanent Magnetization of Rocks'. In: *Geophysical Journal International* 24.4 (Dec. 1971), pp. 429–433. DOI: 10.1111/j.1365-246X.1971.tb02188.x.

[32] A de Sa and L Molyneux. 'A spinner magnetometer'. In: *Journal of Scientific Instruments* 40.4 (Apr. 1963), p. 162. DOI: 10.1088/0950-7671/40/4/306.

[33] Édouard G. H. Philippe et al. 'Are Paleomagnetic Records From U-Channels Appropriate for Studies of Reversals and Excursions?' In: *Geochemistry, Geophysics, Geosystems* 19.11 (2018), pp. 4130–4142. DOI: 10.1029/2018GC007803.

[34] CSC - IT Center for Science LTD. *Elmer FEM*. Built from git commit f89cdc5. URL: www.elmerfem.org (visited on 05/11/2024).

[35] Lewis D. Ashwal, Susan J. Webb and Michael W. Knoper. 'Physical and mineralogical properties of Bushveld rocks: magnetic susceptibility, density and mineral chemistry profiles in the 2950 m Bellevue drillcore, Northern Lobe.' In: *South African Journal of Geology - S AFR J GEOL* 108 (Sept. 2005), pp. 199–232. DOI: 10.2113/108.2.199.

[36] John P. Bentley. 'Signals and Noise in Measurement Systems'. In: *Principles of Measurement Systems*. 4th ed. Essex, England: Pearson Education Limited, 2005, pp. 97–124. ISBN: 0-130-43028-5.

[37] *Manual for Triaxial Fluxgate Sensor FGM3D*. Tech. rep. Version 2.01. Sensorik & Systemtechnologie GmbH, 2023.

[38] *Manual for TDX Multi Channel Data Logger*. Tech. rep. Version 1.14 Rev 2.00. Sensorik & Systemtechnologie GmbH, 2024.

[39] S. L. Gokhale. 'Magnetic Shielding (Shielding of Magnetic Instruments From Steady Stray Fields)'. In: *Transactions of the American Institute of Electrical Engineers* 48.4 (1929), pp. 1307–1319. DOI: 10.1109/T-AIEE.1929.5055402.

[40] Trond H. Torsvik and Odleiv Olesen. *Petrophysics and Palaeomagnetism initial report of the Norwegian Geological Survey Laboratory*. Tech. rep. Norges Geologiske Undersøkelse, Oct. 1988. URL: www.ngu.no/publikasjon/petrophysics-and-palaeomagnetism-intial-report-norwegian-geological-survey-laboratory (visited on 12/01/2025).

[42] ASTM International. *Standard Specification for Wrought Nickel-Iron Soft Magnetic Alloys (UNS K94490, K94840, N14076, N14080)*. Tech. rep. 100 Barr Harbor Drive, PO Box C700, West Conshohocken, PA, 19428-2959 USA, 23rd Feb. 2021. DOI: 10.1520/A0753-21.

[43] A E Drake and C I Ager. 'The development and use of low magnetic permeability reference materials.' In: *6th British Electromagnetic Measurements Conference Digest (BEMC 93)*. 1993, pp. 15/1–15/3. URL: www.eprintspublications.npl.co.uk/2840.

[44] Bo Hu, Runqiao Yu and Hengcai Zou. 'Magnetic non-destructive testing method for thin-plate aluminum alloys'. In: *NDT & E International* 47 (2012), pp. 66–69. ISSN: 0963-8695. DOI: 10.1016/j.ndteint.2011.12.007.

[45] Christophe Geuzaine and Jean-François Remacle. *Gmsh Reference Manual for Gmsh 4.14.0*. 3rd Nov. 2024. URL: www.gmsh.info/dev/doc/texinfo/gmsh.pdf (visited on 11/11/2024).

[46] Partick Knupp. 'Measurement and Impact of Mesh Quality'. In: *46th AIAA Aerospace Sciences Meeting and Exhibit*. 2008. DOI: 10.2514/6.2008-933.

[47] Christophe Geuzaine and Jean-François Remacle. *Gmsh*. Version 4.13.1. 24 May 2024. URL: www.gmsh.info (visited on 05/11/2024).

[48] Kitware Inc. *VTK - The Visualization Toolkit*. Version 9.3.1. 29 June 2024. Kitware Inc. URL: www.vtk.org (visited on 18/11/2024).

[49] C. J. Stimpson et al. *Verdict*. Version 1.4.2. 19 July 2023, Sandia National Laboratories. URL: www.github.com/sandialabs/verdict (visited on 18/11/2024).

[50] Python Software Foundation. *Python Language Reference*. Version 3.13.2. URL: www.python.org (visited on 24/03/2025).

[51] Peter Råback et al. *Elmer Models Manual*. Tech. rep. CSC - IT Center for Science, 7th June 2021. URL: www.nic.funet.fi/pub/sci/physics/elmer/doc.

[52] Pasquale Arpaia et al. 'Magnetic characterization of Mumetal® for passive shielding of stray fields down to the nano-Tesla level'. In: *Nuclear Instruments and Methods in Physics Research Section A: Accelerators, Spectrometers, Detectors and Associated Equipment* 988 (2021), p. 164904. ISSN: 0168-9002. DOI: 10.1016/j.nima.2020.164904.

[53] Sandia National Laboratories, Los Alamos National Laboratory and Kitware Inc. *ParaView*. Version 5.13. 22 August 2024. Kitware Inc. URL: www.paraview.org (visited on 05/11/2024).

[54] Nicholas M. Warrener et al. 'Design of a measurement system for the rapid detection of geomagnetic reversals recorded in drill cores'. In: *18th SAGA Biennial Conference & Exhibition 2024*. Unpublished manuscript. Southern African Geophysical Association. Oct. 2024, pp. 1–5.

[55] Geoffrey Bate. 'Magnetic recording materials since 1975'. In: *Journal of Magnetism and Magnetic Materials* 100.1 (1991), pp. 413–424. ISSN: 0304-8853. DOI: 10.1016/0304-8853(91)90831-T.

[56] Lebogang Ledwaba. *Neutron and X-ray Tomographic Investigation of Dendritic Growth Patterns in Bushveld Complex Anorthosite*. School of Geosciences, University of the Witwatersrand, Johannesburg. Hons research project. 2007.

[57] Barna Szabó and Ivo Babuška. *Introduction to Finite Element Analysis: Formulation, Verification and Validation*. 1st ed. John Wiley & Sons, Ltd, 2011. DOI: 10.1002/9781119993834.

[58] Jr C. H. Arendt. *Designers Handbook: The When Why and How of Magnetic Shielding*. Tech. rep. (visited on 01/29/2025). Westinghouse Electric Corporation, 1966. URL: www.efineametals.com/wp-content/uploads/2020/06/Magnetic_Shielding_Handbook_WestinhouseR.pdf.

[59] Chinthaka P. Gooneratne, Bodong Li and Timothy E. Moellendick. 'Downhole Applications of Magnetic Sensors'. In: *Sensors* 17.10 (2017). ISSN: 1424-8220. DOI: 10.3390/s17102384.

[60] James R. Austin and Clive A. Foss. 'The Paradox of Scale: Reconciling magnetic anomalies with rock magnetic properties for cost-effective mineral

exploration'. In: *Journal of Applied Geophysics* 104 (2014), pp. 121–133. ISSN: 0926-9851. DOI: 10.1016/j.jappgeo.2014.02.018.

[61] Trevor Williams. 'Magnetostratigraphy from downhole measurements in ODP holes'. In: *Physics of the Earth and Planetary Interiors* 156.3 (2006). ODP Contributions to Paleomagnetism, pp. 261–273. ISSN: 0031-9201. DOI: 10.1016/j.pepi.2005.09.016.

[62] Helga de Wall and Horst-Ulrich Worm. 'Recognition of drilling-induced remanent magnetization by Q-factor analysis: a case study from the KTB-drillholes'. In: *Journal of Applied Geophysics* 46.1 (2001), pp. 55–64. ISSN: 0926-9851. DOI: 10.1016/S0926-9851(00)00039-2.

[63] Richard J. Blakely. 'Magnetization'. In: *Potential Theory in Gravity and Magnetic Applications*. Cambridge, United Kingdom: Cambridge University Press, 1996, pp. 81–99. DOI: 10.1017/CBO9780511549816.

[64] David J. Griffiths. 'Magnetic fields in matter'. In: *Introduction to Electrodynamics*. 5th ed. Cambridge University Press, 2024, pp. 268–298. DOI: 10.1017/9781009397735.007.

Further Reading

S. M. Kamens and R. M. Koren. *The Drop Test: Deterioration of Magnetic Shielding Due to Mishandling or Abuse*. Tech. rep. EMC Technology, 1987. URL: www.amuneal.com/wp-content/uploads/2016/05/Magnetic_Shielding_Mishandling_Article.pdf (visited on 25/02/2025).

Benedict Feinberg and Harvey Gould. 'Placed in a steady magnetic field, the flux density inside a permalloy-shielded volume decreases over hours and days'. In: *AIP Advances* 8.3 (Mar. 2018). ISSN: 2158-3226. DOI: 10.1063/1.5009926.

Bernt Jakobsen. 'The Sleipner accident and its causes'. In: *Engineering Failure Analysis* 1.3 (1994), pp. 193–199. DOI: 10.1016/1350-6307(94)90018-3.

Appendix A

Magnetic Shield Specifications

A.1 Mechanical Specifications

The magnetic shield used in the investigation is composed of two concentric 1 mm thick cylinders made from ASTM A753 Alloy 4 metal. The cylinders are fixed in place by aluminium end plates which, in turn, are held together with brass rods (not shown in the drawing).

The dimensioned drawing, below, is based on measurements taken of the chamber using a vernier calliper and a wooden ruler.

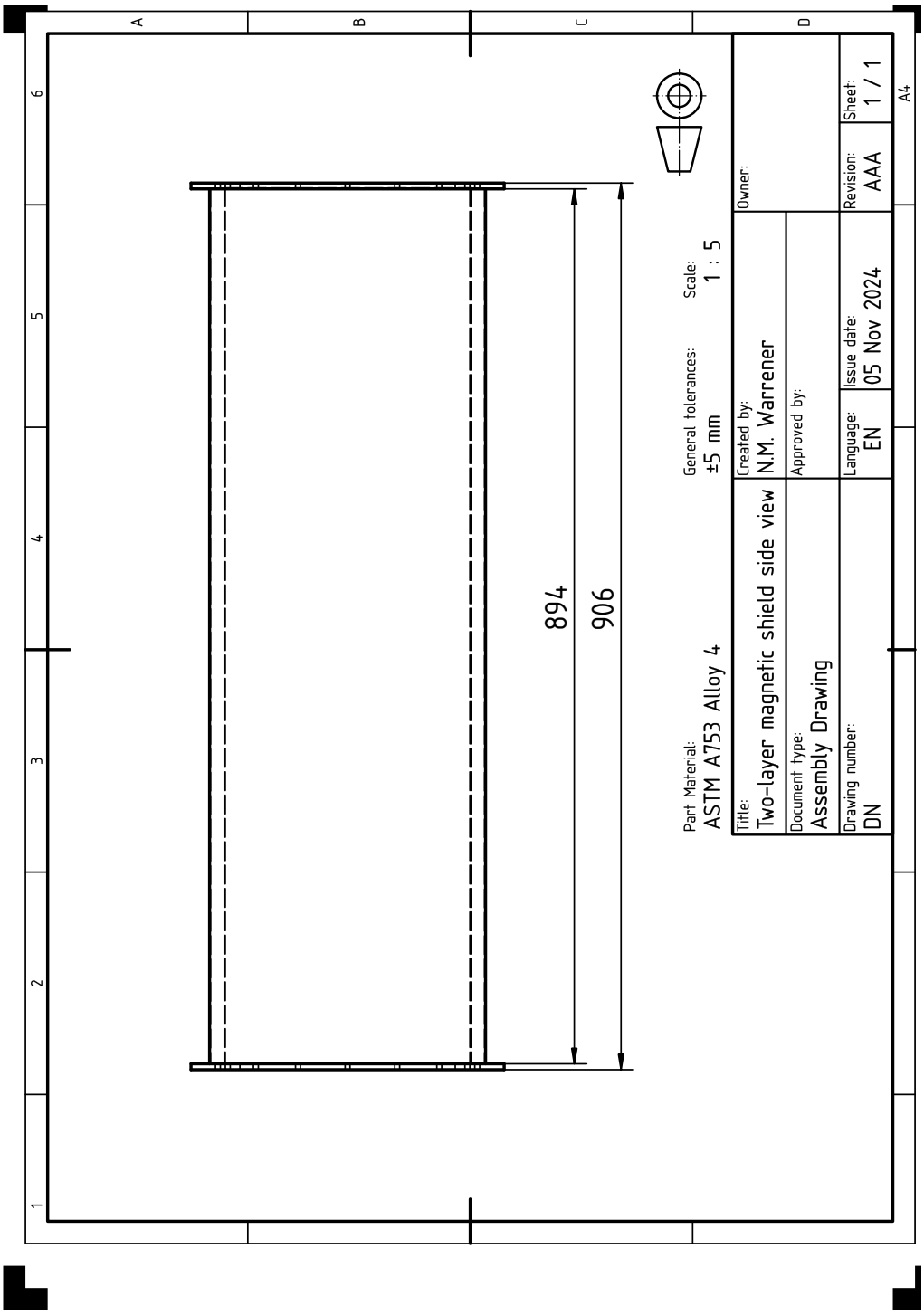


Figure A.1.1: A dimensioned drawing of the side of the magnetic shield used in the investigation.

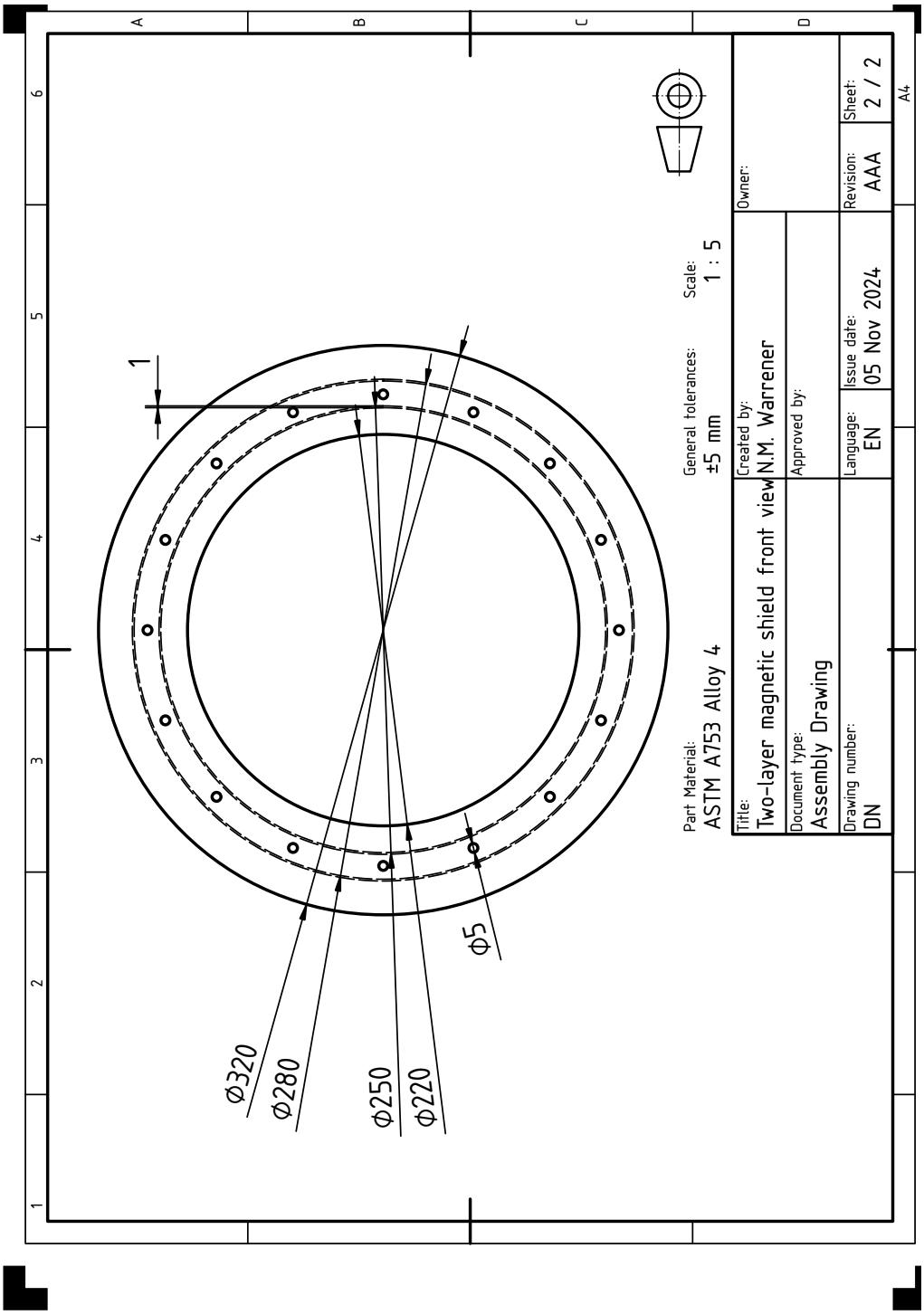


Figure A.1.2: A dimensioned drawing of the front of the magnetic shield used in the investigation.

A.2 ASTM A753 Alloy 4 Properties

The magnetic shield used in the investigation consisted of two concentric 1 mm thick ASTM A753 Alloy 4 layers. This alloy has a non-linear permeability which is dependent on the inducing **H**-field. An experimentally determined B-H relationship for an alloy this thick could not be found. Rather, data for the closest available thickness was obtained from experimental determination of the B-H relationship for a toroid consisting of 17 stacked layers of 0.1 mm thick ASTM A753 Alloy 4 foil which yielded a total thickness of 1.7 mm [52]. The raw material data, presented in Table A.1, was obtained from sample 2 of Figure 3 in Arpaia et al. (2021).

For complete chemical and other properties, the ASTM standard document should be reviewed [42].

Table A.1: A table of B-H data for 1.4 mm thick ASTM A753 Alloy 4 derived from Sample 2 in Figure 3 from the paper by Arpaia et al., used to fit a cubic spline and interpolate points for magnetic shield simulations in the investigation.

H (A/m)	B (T)
0.000	0.000
0.261	0.003
0.300	0.004
0.339	0.004
0.379	0.004
0.757	0.008
1.129	0.012
1.511	0.016
1.880	0.020
2.255	0.024
2.469	0.026
2.635	0.030
3.019	0.034
4.052	0.052
8.118	0.146
12.302	0.225
16.267	0.281
20.464	0.321
24.652	0.353
28.810	0.377
32.594	0.399
36.874	0.415
38.674	0.428
75.996	0.544
113.685	0.620
152.268	0.661
188.644	0.682
265.508	0.705
304.934	0.715
339.033	0.722
377.759	0.729

Appendix B

Magnetic Shield Finite Element Analysis Setup

B.1 Processing B-H Data for FEA Use

For the FEA, the non-linear permeability is supplied in the form of B-H data for ASTM A754 Alloy 4 material. Before using this data, a cubic spline was fitted so that the values can be interpolated. The script to perform the interpolation is found in Listing B.1. The result of the interpolation is presented in Figure B.1.1.

Elmer requires the cubic spline start at the origin. The original data from Arpaia et al. does not have a zero-field measurement. For the purposes of the FEA, the material was assumed to exhibit negligible hysteresis.

Listing B.1: A MATLAB® script to fit a cubic spline to B-H data and use the spline to interpolate the data.

```
% 16 August 2023
% This script takes the original B-H values and fits a cubic
% spline to them. The cubic spline is then used to interpolate
% the B-H data so that we have more data for Elmer. This is
% also necessary because Elmer requires the data to be created
% from a cubic spline.

% The first and second columns in raw.txt are the B-values and
% H-values, respectively. The delimiter is whitespace.
% H is in first column, B is in second column.
M = readmatrix('original_bh.csv');
b_inter = spline(M(:,1), M(:,2), min(M(:,1)):0.001:max(M(:,1)));

% Plot of the interpolated values
semilogx(min(M(:,1)):0.001:max(M(:,1)), b_inter');
hold on;
% Plot of the original values
semilogx(M(:,1), M(:,2));
hold off;
legend({'Interpolated', 'Original'}, 'Location','southeast')
xlabel('Magnetic field strength (A/m) ') % Also called H-field
ylabel('Magnetic flux density (T) ') % Also called B-field

% Save the interpolated values to a text file
res = [min(M(:,1)):0.001:max(M(:,1)); b_inter]';
writematrix(res,'interpolated_bh.dat','Delimiter','space')
```

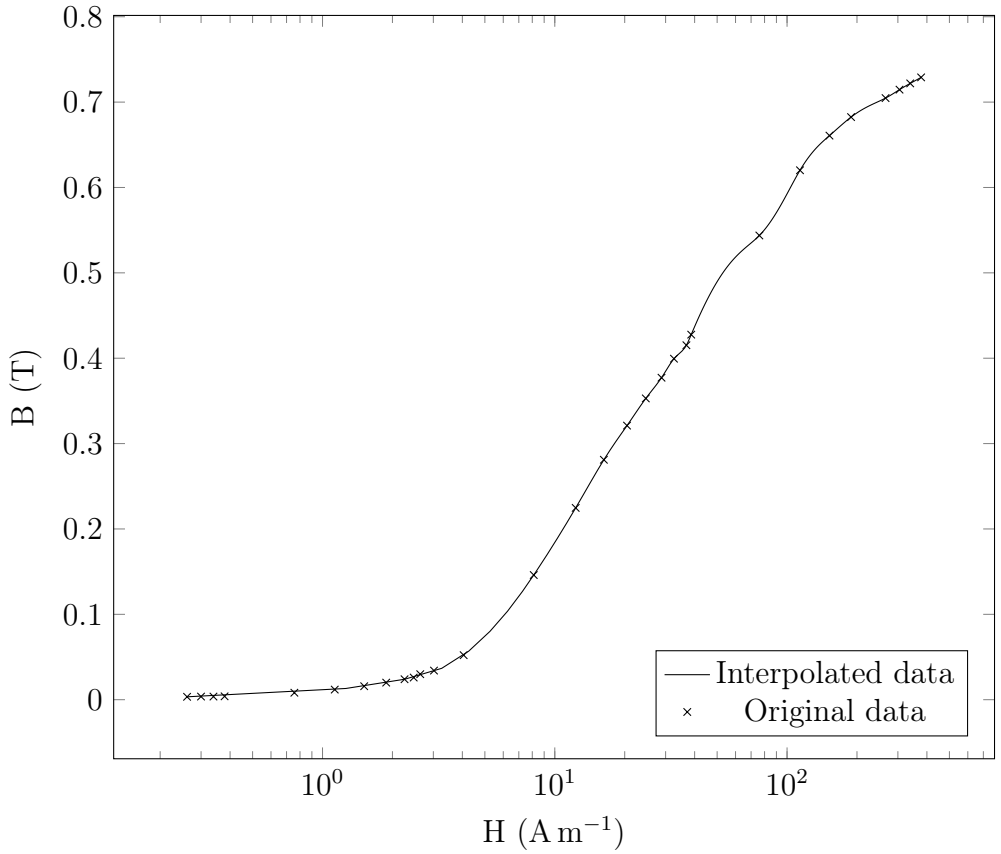


Figure B.1.1: A semi-log plot of the original B-H points measured by Arpaia et al. for 1.4 mm thick ASTM A753 Alloy 4 and a line plot derived from fitting a cubic spline to the original data.

B.2 Geometry and Mesh

The geometry file used by the mesh generation program, Gmsh, is as follows:

Listing B.2: Gmsh script, saved as "model.geo", for the geometry used to represent a two-layer cylindrical magnetic shield.

```
// Mesh generated with Gmsh version 4.13.1.
// NOTE: ELMER WILL ASSUME ALL UNITS ARE IN METRES.

// Geometry kernel.
SetFactory("OpenCASCADE");

// Environment surrounding the shield/simulation domain.
```

```
Cylinder(1) = {-2.7, 0, 0, 5.4, 0, 0, 0.84, 2*Pi};

// Transition to the outer mu-layer
Cylinder(2) = {-0.6, 0, 0, 1.2, 0, 0, 0.23, 2*Pi};

// 2 layer mu-metal chamber
Cylinder(3) = {-0.45, 0, 0, 0.9, 0, 0, 0.140, 2*Pi};
Cylinder(4) = {-0.45, 0, 0, 0.9, 0, 0, 0.139, 2*Pi};
Cylinder(5) = {-0.45, 0, 0, 0.9, 0, 0, 0.125, 2*Pi};
Cylinder(6) = {-0.45, 0, 0, 0.9, 0, 0, 0.124, 2*Pi};

// Region inside the working space of the shield.
Cylinder(7) = {-0.35, 0, 0, 0.7, 0, 0, 0.075, 2*Pi};

BooleanDifference{ Volume{1}; Delete; }{ Volume{2}; }
BooleanDifference{ Volume{2}; Delete; }{ Volume{3}; Volume{4};
   Volume{5}; Volume{6}; }
BooleanDifference{ Volume{3}; Delete; }{ Volume{4}; }
BooleanDifference{ Volume{4}; Delete; }{ Volume{5}; }
BooleanDifference{ Volume{5}; Delete; }{ Volume{6}; }
BooleanDifference{ Volume{6}; Delete; }{ Volume{7}; }
Coherence;

// Rotate everything by \qty{90}{\degree} so as to align with
   coordinate system of fluxgate.
// Not strictly necessary but just done for convenience.
Rotate {{0, 0, 1}, {0, 0, 0}, 1.57079632679} { Volume{1}; Volume{2};
    Volume{3}; Volume{4}; Volume{5}; Volume{6}; Volume {7}; }

// Assign names to the different volumes so that they can be given
// material properties in the Elmer FEM solver input file.
Physical Volume("chamber_interior_vol", 96) = {7};
Physical Volume("chamber_vol", 97) = {6};
Physical Volume("inner_mu_vol", 98) = {5};
Physical Volume("air_between_mus_vol", 99) = {4};
Physical Volume("outer_mu_vol", 100) = {3};
Physical Volume("fine_mesh_transition_vol", 101) = {2};
Physical Volume("domain_vol", 102) = {1};

// Give the surfaces constituting the outermost object a name so
// that boundary conditions can be applied to them in the
// Elmer FEM solver input file.
Physical Surface("domain_boundaries", 103) = {31, 33, 32};

// Environment region
Transfinite Curve {24, 23, 22} = 100 Using Progression 1;

// Inner transition region (the region between the environment
   region and the outer mu layer).
Transfinite Curve {27, 26, 25} = 160 Using Progression 1;

// The thin gap making up each mu layer and the air gap between the
   mu layers.
```

```
Transfinite Curve {34, 34, 36, 30, 32, 38, 39, 37, 29, 35, 33, 31,
    28} = 685 Using Progression 1;

// Region inside the working space of the mu chamber. Need coarser
    mesh here to reduce mesh size.
Transfinite Curve {42, 41, 40} = 200 Using Progression 1;

Mesh.Algorithm   = 5;  // Delaunay
Mesh.Algorithm3D = 10; // HXT

Mesh.MaxNumThreads1D = 16;
Mesh.MaxNumThreads2D = 16;
Mesh.MaxNumThreads3D = 16;
```

B.3 Simulation Input File

The input file, called `case.sif`, supplied to the FEA program, called `ElmerSolver`, is given in Listing B.3, below.

Listing B.3: Elmer FEM configuration, saved as "case.sif", for a simulation of a two-layer cylindrical magnetic shield exposed to an ambient magnetic field.

```
! Ran with Elmer Version 9.0 (Rev: f89cdc5ed, Compiled: 2024-10-26)
! Constants used to define the three-components of the ambient
! magnetic field (UNITS IN TESLAS!)

! Horizontal components
! X-component is parallel to radial axis of cylinder.
! Y-component is parallel to main axis of cylinder.
$ Bx = (9.7617e3)*1e-9
$ By = (2.1429e3)*1e-9

! Vertical component.
$ Bz = (2.0485e4)*1e-9

Header
    CHECK KEYWORDS Warn
    Mesh DB "mesh"
    Include "mesh/mesh.names"
    Include Path ""
    Results Directory "results"
End

Simulation
    Max Output Level = 5
    Coordinate System = Cartesian
    Coordinate Mapping(3) = 1 2 3
    Simulation Type = Steady state
    Steady State Max Iterations = 1
    Output Intervals(1) = 1
    Coordinate Scaling = 1
    Solver Input File = case.sif
    Post File = case.vtu
End

Constants
    Permittivity of Vacuum = 8.85418781e-12
    Permeability of Vacuum = 1.25663706e-6
End

Body 1
  Target Bodies(5) = 1 2 4 6 7
  Name = air_bodies
  Equation = 1
  Material = 1
End

Body 2
  Target Bodies(2) = 3 5
  Name = mumetal_bodies
  Equation = 1
  Material = 2
```

```
End

Solver 1
    Equation = MgDyn
    ! Use the WhitneyAVSolver in the MagnetoDynamics file.
    Procedure = "MagnetoDynamics" "WhitneyAVSolver"
    Exec Solver = Always

    ! From I-DEAS Student Guide (ISBN: 0-9638178-4-1)
    ! Bandwidth is the maximum width of the non-zero rows
    ! surrounding the diagonal of the stiffness matrix.
    ! Larger bandwidth increase solution time dramatically.
    Optimize Bandwidth = True

    Steady State Convergence Tolerance = 1e-8

    Nonlinear System Convergence Tolerance = 1e-8
    Nonlinear System Max Iterations = 500
    Nonlinear System Newton After Iterations = 5
    Nonlinear System Newton After Tolerance = 1e-4
    Nonlinear System Relaxation Factor = 1

    ! BiCGStabl is usually most performant for AV-solver.
    Linear System Solver = Iterative
    Linear System Iterative Method = BiCGStabl
    BiCGstabl polynomial degree = 4
    Linear System Max Iterations = 500
    Linear System Convergence Tolerance = 1e-8

    ! Cannot use ILU preconditioning as the stiffness matrix is not
    ! invertible due to the solution of the vector potential being
    ! non-unique.
    ! Preconditioners are nice because they can usually speed up
    ! convergence of the BiCGStabl method by incompletely
    ! factorising the  stiffness matrix. See Section 4.3 of the
    ! ElmerSolver Manual (April 6, 2023 version).
    Linear System Preconditioning = none
    Linear System ILUT Tolerance = 1e-3
    Linear System Abort Not Converged = False
    Linear System Residual Output = 10
    Linear System Precondition Recompute = 1
End

Solver 2
    Equation = MgDynPost
    ! This solver calculates the derived fields of interest.
    Procedure = "MagnetoDynamics" "MagnetoDynamicsCalcFields"
    Exec Solver = Always
    Calculate Magnetic Field Strength = True
    Optimize Bandwidth = True
    Steady State Convergence Tolerance = 1e-9
    Linear System Solver = Iterative
    Linear System Iterative Method = BiCGStab
```

```
    Linear System Max Iterations = 500
    Linear System Convergence Tolerance = 1e-10
    Linear System Preconditioning = ILU0
    Linear System Abort Not Converged = False
    Linear System Residual Output = 10
    Linear System Precondition Recompute = 1

    Calculate Nodal Fields = False
    Calculate Elemental Fields = True

    ! Perform the averaging within this solver
    Average Within Materials = Logical True
End

Solver 3
    Equation = "ResultOutput"
    ! This solver deals with how the results are saved.
    Procedure = "ResultOutputSolve" "ResultOutputSolver"
    Exec Solver = after timestep
    Output File Name = f
    Vtu format = True
    Discontinuous Bodies = True
    Save Geometry Ids = True
    Save Linear Elements = True
    Save Bulk Only = True

    ! Save different parts of results to different files
    Vtu Part Collection = False
End

! Equations are a way of grouping a bunch of seperate solvers and
! setting their execution order.
Equation 1
    Name = "Equation 1"
    Active Solvers(3) = 1 2 3
End

Material 1
    Name = "Air"
    Relative Permeability = 1.0
    Relative Permittivity = 1.0
End

Material 2
    Name = "ASTM A753 Alloy 4"
    Relative Permittivity = Real 1.0
    Electric Conductivity = Real 1.67e4

    H-B Curve = Variable "dummy"
    Real Cubic Monotone
        include "H-B_Spline_A753_Alloy_4_Interpolated.dat"
    End
End
```

```
Boundary Condition 1
    Name = "Ambient Field"
    Target Boundaries(1) = $ domain_boundaries

    ! The magnetic flux density B is the circulation of the
    ! magnetic vector potential A: B = curlA
    ! Inverting this relationship allows to express A in terms
    ! of B. A side effect of this is that A is *not* uniquely
    ! defined. We can therefore use many different expressions
    ! to give A a valid definition. In this application, A is
    ! assumed to be of the form:
    ! A = Bx (0, -z/2, y/2) + By (z/2, 0, -x/2) + Bz (-y/2, x/2, 0)
    AV {e} 1 = Variable Coordinate 1, Coordinate 2, Coordinate 3
    Real MATC "By * tx(2)/2 - Bz * tx(1)/2"
    AV {e} 2 = Variable Coordinate 1, Coordinate 2, Coordinate 3
    Real MATC "-1*Bx * tx(2)/2 + Bz * tx(0)/2"
    AV {e} 3 = Variable Coordinate 1, Coordinate 2, Coordinate 3
    Real MATC "Bx * tx(1)/2 - By * tx(0)/2"
End
```

The file "mesh.names" referenced on line 16 in Listing B.3 is an auxiliary file generated by the `ElmerGrid` codes and is presented in Listing B.4, below.

Listing B.4: Elmer Grid mesh.names file used to associate alias names with the geometry IDs.

```
! ------ names for bodies ------
$ chamber_interior_vol = 1
$ chamber_vol = 2
$ inner_mu_vol = 3
$ air_between_mus_vol = 4
$ outer_mu_vol = 5
$ fine_mesh_transition_vol = 6
$ domain_vol = 7
! ------ names for boundaries ------
$ domain_boundaries = 1

! Unnamed boundaries are assigned generated names.
$ surf_bc398 = 398
$ surf_bc741 = 741
$ surf_bc751 = 751
$ surf_bc1568 = 1568
$ surf_bc3182 = 3182
$ surf_bc3198 = 3198
```

Appendix C

Compute Resources

The specifications of the compute resources used to run the finite element analysis (FEA) codes presented in the investigation are provided. Details on the profiling performed on the hardware to determine the limitations that the FEA codes must operate under for the simulation of a two-layer cylindrical magnetic shield to complete successfully are investigated.

The Elmer FEM codes implemented the Message Passing Interface (MPI) which facilitated communication of multiple processes on a single computer and even multiple computers on the same network. Operating Elmer FEM in an environment where multiple computers were used to execute the codes proved advantageous due to the ability to pool multiple compute resources together. In this way, a simulation whose requirements exceed the resources of a single computer can be evaluated by distributing the workload across multiple computers.

C.1 System Specifications

The FEA codes were run in a distributed compute environment. The environment consisted of six compute nodes with the following specifications:

- Intel® Xeon® D-1587 - 16 physical cores with Intel® Hyper-Threading Technology disabled
- 10 Gbit/s connectivity
- 64 GB of memory
- Ubuntu 24.04.1 LTS

The generation of the input mesh was performed on a single compute node, with the same specifications as given above.

C.2 Resource Usage

The resource usage of the FEA codes was profiled so as to determine the maximum number of mesh elements that can be incorporated in an input mesh before an analysis failed due to insufficient memory.

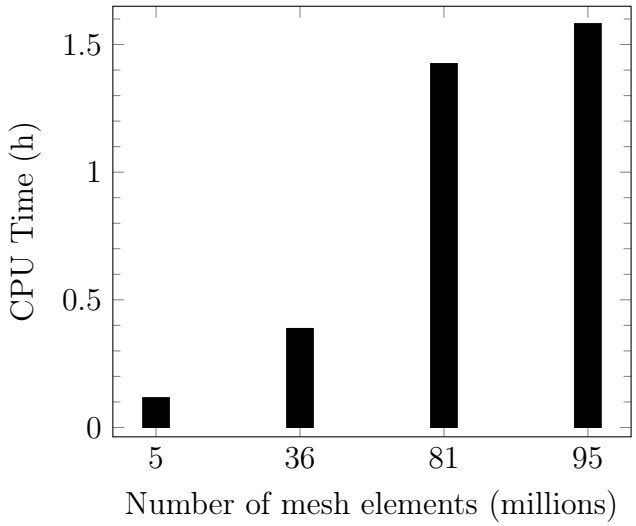


Figure C.2.1: A bar graph of the number of elements in an input mesh, to an FEA, and the amount of CPU time taken for the FEA code to reach the convergence criterion.

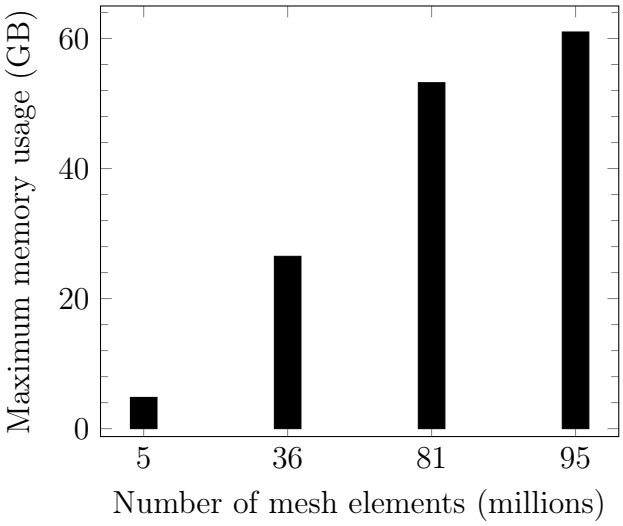


Figure C.2.2: A bar graph of the number of elements in an input mesh, to an FEA, and the maximum memory usage, per compute node, during execution of the FEA code.

Appendix D

Fundamentals and Terminology

The following section provides a brief clarification on the terminology and fundamental physics used in the dissertation. The aim is to give clarification to some of the ambiguities that arise in the discussion of magnetism.

D.1 Magnetic Fields

The vector fields, **B**, **H**, and **M** associated with magnetic materials and fields are confusing. A brief discussion on their origin and application is warranted. The closely related physical properties, bulk or volumetric magnetic susceptibility κ_v and permeability μ are also explored.

D.1.1 Flux Density, Field Intensity, and Magnetisation

Magnetic fields are described by vector fields. The magnetic flux density **B** is considered *the* fundamental vector field, representing the total magnetic field that arises from both macroscopic and microscopic currents in matter [63].

To simplify computations involving magnetic materials, the magnetic flux density **B** can be separated into two components [63]. The first component, the magnetic field intensity **H**, accounts for the contribution from external (free) currents such as those produced by the movement of charge [63, 64]. The second component,

the magnetisation **M**, represents the contribution from bound currents within the material, which originate from atomic-scale phenomena like electron spin and orbital motion [63, 64]. Thus, the magnetic field in and around materials is described by the following relation:

$$\mathbf{B} = \mu_0(\mathbf{H} + \mathbf{M}) \tag{D.1}$$

From this equation, it can be seen that **H** is simply a parameter of convenience that is proportional to **B** *in non-magnetisable* materials ($\mathbf{M} = 0\,\mathrm{A/m}$) [10]. Inside a magnetisable material, **H** describes how **B** is altered by the permanent magnetisation **M** [10].

D.2 Physical Properties

D.2.1 Magnetic Permeability and Susceptibility

Bulk or volumetric magnetic susceptibility κ_v is a dimensionless physical quantity. It is dependent on the material properties and is also a function of **H** but usually constant for small **H**-fields [64, 10]. Equation D.2 shows how susceptibility relates **H** and **M**.

$$\mathbf{M} = \kappa_v \mathbf{H} \tag{D.2}$$

In words, magnetic susceptibility describes how easily a material becomes magnetised [10]. It does not indicate the size of the permanent magnetisation once the inducing field is removed. Substituting the relation in Eq D.2 into Eq D.1 yields Eq D.3 [10].

$$\mathbf{B} = \mu_0 \mathbf{H}(1 + \kappa_v) \tag{D.3}$$

Magnetic susceptibility can be used as a diagnostic tool to discern between three main classes of magnetic behaviour viz. diamagnetism, paramagnetism and ferro-

magnetism [10].

Magnetic permeability μ is also a physical quantity that has the same dependency on material properties and the **H**-field as magnetic susceptibility. Following the form of the **M**-**H** relationship, Eq D.4 shows how magnetic permeability relates **H** and **B**.

$$\mathbf{B} = \mu\mathbf{H} \tag{D.4}$$

The above relation shows that permeability expresses the ability of a material to concentrate magnetic flux lines [10]. Permeability of a material can also be expressed in terms of magnetic susceptibility and vacuum permeability:

$$\mu = \mu_0\mu_r = \mu_0(1 + \kappa_v) \tag{D.5}$$

It is important to note that practical materials have susceptibilities, permeabilities, and magnetisations that are fully expressed as rank-two tensors [63]. As an example, a material's magnetisation has a preferred direction, known as the "easy direction" [10].

D.3 Terminology

The **B**-field is *the* fundamental magnetic field and the term "magnetic field", is reserved for discussions about the **B**-field, only [64]. Misuse of this term, in the literature, when discussing **H** boils down to the fact that **H** is a quantity dependent on the free current through a material [64]. It is this current that can be controlled in an experiment or application. Therefore, from this perspective, **H** is more useful in a discussion as the **B**-field depends on a material's properties and hysteresis effects which are not easily controlled [64].